

**TURBULENT COLLAPSE OF GRAVITATIONALLY BOUND
CLOUDS**

by

Daniel W. Murray

A DISSERTATION SUBMITTED IN
PARTIAL FULFILLMENT OF THE
REQUIREMENTS FOR THE DEGREE OF

DOCTOR OF PHILOSOPHY
IN PHYSICS

at

The University of Wisconsin–Milwaukee

May 2018

ABSTRACT

TURBULENT COLLAPSE OF GRAVITATIONALLY BOUND CLOUDS

by

Daniel W. Murray

The University of Wisconsin–Milwaukee, May 2018

Under the Supervision of Professor Philip Chang

In this dissertation, I explore the time-variable rate of star formation, using both numerical and analytic techniques. I discuss the dynamics of collapsing regions, the effect of protostellar jets, and development of software for use in the hydrodynamic code RAMSES. I perform high-resolution adaptive mesh refinement simulations of star formation in self-gravitating turbulently driven gas. I have run simulations including hydrodynamics (HD), and HD with protostellar jet feedback. Accretion begins when the turbulent fluctuations on largescales, near the driving scale, produce a converging flow. I find that the character of the collapse changes at two radii, the disk radius \vec{r}_d , and the radius \vec{r}_* where the enclosed gas mass exceeds the stellar mass. This is the first numerical work to show that the density evolves to a fixed attractor, $\rho(\vec{r}, t) \rightarrow \rho(\vec{r})$, for $\vec{r}_d < \vec{r} < \vec{r}_*$; mass flows through this structure onto a sporadically gravitationally unstable disk, and from thence onto the star. The total stellar mass $M_*(t) \sim (t - t_*)^2$, where $(t - t_*)^2$ is the time elapsed since the formation of the first star. This is in agreement with previous numerical and analytic work that suggests a linear rate of star formation. I show that protostellar jets change the normalization of the stellar mass accretion rate, but do not strongly affect the dynamics of star formation in hydrodynamics runs. In particular, $M_*(t) \propto (1 - f_{\text{jet}})^2 (t - t_*)^2$ is the fraction of mass accreted onto the protostar, where f_{jet} is the fraction ejected by the jet. For typical values of $f_{\text{jet}} \sim 0.1 - 0.3$ the accretion rate onto the star can be reduced by a factor of two or three. However, I find that jets have only a small effect (of order 25%) on the accretion rate onto the protostellar disk (the “raw” accretion rate). In other words, jets do not affect the dynamics of the infall, but rather simply eject mass before it reaches the star. Finally, I show that the small scale

structure — the radial density, velocity, and mass accretion profiles — are very similar in the jet and no-jet cases.

TABLE OF CONTENTS

1	Introduction	1
1.1	The Phenomenology of the Interstellar Medium (ISM)	3
1.1.1	Warm Ionized Gas	3
1.1.2	Neutral Gas	4
1.1.3	Molecular Gas	5
1.1.4	Deviations from Larson’s laws in massive star forming regions . .	7
1.2	Where Are Stars Born?	8
1.2.1	Star formation tracers	8
1.2.2	Correlation between Free-Free & CO and between FIR & CO . .	10
1.3	Star formation	10
1.3.1	Star Formation Efficiency (SFE)	11
1.4	Star Formation on the Galactic Scale, The Kennicutt-Schmidt Law . . .	12
1.5	Star Formation on the GMC scale	13
1.6	Review of Analytic Theories of Star Formation	13
1.6.1	Larson (1969) and Penston (1969)	14
1.6.2	Shu (1977)	15
1.6.3	Myers & Fuller (1992)	15
1.7	Current Numerical simulations and Observations	16
1.7.1	Krumholz & McKee - The Berkeley Group	17
1.7.2	Klessen & Mac Low Group	17
1.7.3	Lee et al. (2015)	18
1.7.4	Murray & Chang (2015)	19
1.7.5	Galaxy Scale Simulations	21
1.8	What this Dissertation Does Not Cover	22
1.8.1	Missing Physics	22

2	Hydrodynamic Simulations	25
2.1	Detailed Simulations of Turbulent Collapse	26
2.2	Results	30
2.2.1	The Run of Infall ($ \vec{u}_r $), Circular (\vec{v}_ϕ), and Random Motion (\vec{v}_T) Velocities	32
2.2.2	The Stellar Sphere of Influence	34
2.2.3	A Fixed Point Attractor for $\rho(\vec{r}, t)$ Inside \vec{r}_*	37
2.2.4	Mass Accretion Rate	38
2.2.5	Rotationally Supported Disks	39
2.2.6	Gravitationally Unstable Disks	41
2.2.7	Average Profiles	41
2.2.8	Mass Accretion Rates	50
2.3	Discussion	53
2.3.1	Basic Results of this Work	53
2.3.2	Comparisons to Observations	58
2.4	Conclusions	60
2.5	Appendix	62
2.5.1	Notes on Calculating the Random Motion and Rotational Velocity	62
2.5.2	Filamentary or Spherical Accretion?	63
2.5.3	Star Formation Criteria	66
2.5.4	Radial and Lateral Components of the Random Motion Velocity .	67
2.5.5	The Initial Mass Function	69
2.5.6	Convergence with N_J	70
3	Jet Feedback in Star Formation	73
3.1	Current State of the Field	73
3.2	Numerical Implementation	75
3.2.1	Jet Feedback Prescription	75
3.2.2	Protostar Evolution Prescription	78

3.3	Jet Feedback in Turbulent Star Formation	80
3.3.1	Parsec Scale Effects of the Jets	82
3.3.2	Star Formation Rate	83
3.3.3	A Fixed Point Attractor for $\rho(\vec{r}, t)$ Inside \vec{r}_*	88
3.3.4	The Infall ($ \vec{u}_r $), Circular (\vec{v}_ϕ) and Random Motion (\vec{v}_T) Velocities with Protostellar Jets	89
3.3.5	Average Mass Accretion Rate $\langle \dot{M}(\vec{r}, t) \rangle_{\text{stars}}$ for Jet and No Jet Sink Particles	91
3.3.6	Jet Momentum Deposition	91
3.3.7	Jets Mainly Drive Small Scale Turbulence	93
3.4	Discussion	96
3.5	Conclusions	100
3.6	Appendix	101
3.6.1	Effects of Excising Bi-cones Aligned with Protostellar Jets on the Infall, Random, and Rotational Velocity	101
3.6.2	Protostellar Model	102
4	Conclusions	104
4.1	Isolating the Effect of Random Thermal Motions	105
4.2	The Effect of Protostellar Jets	107
4.3	Future Work	107
4.4	Curriculum Vitae	118

LIST OF FIGURES

1	HD – Projected Density of the Simulation Box	31
2	HD – Stellar Sphere of Influence I	33
3	HD – Stellar Sphere of Influence II	34
4	HD – Stellar Sphere of Influence III	36
5	HD – Sphere of Influence IV	37
6	HD – Run of Density	38
7	HD – Run of Mass Accretion Rate	40
8	HD – Toomre Q	42
9	HD – Run of Mass/Number Density	43
10	HD – Velocity vs. Density	46
11	HD – Sink Averaged Run of Velocity	47
12	HD – Run of Mass	48
13	HD – Ratio of Pressure and Gravity	49
14	HD – Toomre Q Average	50
15	HD – Mass Accretion Rate over Time	54
16	HD – Normalized \dot{M} and Normalized Solid Angle	64
17	HD – Non-filamentary Accretion	65
18	HD – Comparison of Particle Formation Checks	66
19	HD – Radial vs Lateral Turbulence	67
20	HD – Initial Mass Function	70
21	HD – Average Stellar Mass as a function of $t - t_*$	71

22	HD – Convergence in Jeans Length	72
23	HD – Average Run of Density for Sink Particles $0.5 - 3.0 M_{\odot}$	72
24	Jet – Test Problem Panel	78
25	Jet – Jet vs. No Jet Comparison	84
26	Jet – Postage Stamp of Jet Blown Gas	85
27	Jet – SFR	86
28	Jet – SFR Varying f_{jet}	87
29	Jet – Density Profile for Jet Feedback	88
30	Jet – Velocity Profile Comparison	90
31	Jet – \dot{M} Profile	92
32	Jet – Jet Momentum over Time	93
33	Jet – Phase Plot of Density vs. Velocity	94
34	Jet – $\vec{v}_{\text{rms}}(t - t_{\text{grav}})$	95
35	Jet – Velocity Power Spectrum	96
36	Jet – Star Formation Efficiency over Time	98
37	Jet – Effect of Subtracting the Jet Cone	102

LIST OF CONVENTIONS

- In astronomy Hydrogen that has been ionized is referred to as HII, where “H” is hydrogen and “II” is the roman numeral for 2.
- Bold font indicates a vector or a matrix, such as **I**, **S** and **x**.
- Vector notation is also used, where an arrow indicates a vector, such as \vec{x} , \vec{v} , \vec{a} . Both styles are used throughout.
- ‘over-dot’ notation (Newtons notation) is used, such as $\dot{M} = \frac{dM}{dt}$

ACKNOWLEDGMENTS

*“Sometimes the gift of an
inquisitive nature to the young can
be greater than that of the wisdom
which comes of age.”*

— Abbot Mordalfus, *Mattimeo* by
Brian Jacques

The inquisitiveness of many good friends and the wisdom of family and colleagues have planted me here. I would not be where I am today without the constant love and support of my family. I would like to thank my nephew Aiden, and Phil’s sons Liam and Gregory, for teaching me to approach everything with an open mind, and to question constantly. I have a new appreciation of sprinklers and “Mighty Machines”, due to their curiosity.

I thank my father for our many stimulating conversations about the physical world, whether it was calculations of our mpg over Tioga Pass or talk of the constellations in the heavens. A special thank you to my sisters for fun times, growing up. My mother encouraged me to use my wits and approach the world with courage.

I would like to thank Matthew Brinson, Adil Amin, and Joe Simon for the countless walks, the coffee breaks, and the occasional late night at Vintage.

I would like to thank all the members of the Leonard E Parker Center for Gravitation, Cosmology & Astrophysics (CGCA) and the UWM Physics Department for being wonderful mentors over the years. I want to especially thank David Kaplan and Dawn Erb for the many rousing CGCA teas, whether science was involved or one of the many festivals around the city.

Finally, I want to acknowledge the guidance, support and encouragement from my advisor Philip Chang. Phil was extremely patient and persistent in shepherding me along towards independent research. He was instrumental in my development both professionally and personally.

I am grateful for the opportunity to complete my dissertation as a member of the CGCA.

Chapter 1

Introduction

“Everything starts somewhere, though many physicists disagree. But people have always been dimly aware of the problem with the start of things. They wonder how the snowplough driver gets to work, or how the makers of dictionaries look up the spelling of words”

— *Hogfather* by Terry Pratchett

Stars are arguably the fundamental building blocks of the Universe, and play a crucial role in the existence of life on Earth. Newborn stars consist of $\sim 71\%$ Hydrogen, $\sim 27\%$ Helium, and a smattering of heavier elements. Almost all of the heavier elements, including those that make up the planets of our solar system, for example oxygen, silicon, and iron, as well as elements found in living organisms, like carbon and nitrogen, were created by stars.

The energy that fuels life and our modern society comes exclusively from stars, with all but one form coming from our Sun. The oil that we burn, the wind energy we capture via turbines, and the radiation we capture via solar panels, all have an origin in the nuclear fusion reactions in the center of our Sun. The one exception is the fuel used in nuclear reactors. Those elements, including Uranium, were created in stars that died before our Sun was born.

Stars have been studied since antiquity, partly because the position of the sun relative

to the stars allowed people to predict the timing of the seasons. Anaxagoras and Democritus argued that the Milky Way consisted of many stars blurred together, and that the sun was a star. While this argument proved to be correct, astronomers long applied it too broadly, asserting that there was no true nebulosity, i.e., no gas or other absorbing material between the stars (Trimble 1997). The idea that there is no gas outside of stars naturally goes hand in hand with the idea that stars are not forming at the present time, an idea consistent with the notion that the stars are eternal, e.g., Thomas Carlyle’s quote that “The eternal stars shine out again, as soon as it is dark enough”. Trimble argues that the idea that most, if not all, stars formed long ago was held by most astronomers until the 20th century.

This paradigm changed dramatically in 1930, when Trumpler (Trumpler 1930) showed convincingly that stellar radiation was absorbed by some medium between the stars. He did so using two methods, one based on the apparent diameters of open clusters, and a second based on the anomalously red colors of stars of a given spectroscopic type known to lie at large distances. In the same paper Trumpler noted that the obscuring material was confined to the plane of the Milky Way. The amount of gas associated with this obscuring material was not known, but was assumed to be small compared to the stellar mass of the Galaxy.

It took another 20 years, and the discovery of 21 cm emission from neutral hydrogen, to establish the presence of a large mass of gas in the Milky Way (Ewen & Purcell 1951; Muller & Oort 1951; Pawsey 1951).

While the existence of a large mass of molecular gas was suspected by some, its presence was not widely acknowledged until the discovery by Wilson et al. (1970) of emission from carbon monoxide (CO) molecules. It was rapidly realized that the molecular gas, which had a total mass of about $1.6 \times 10^9 M_{\odot}$ (Dame 1993; Miville-Deschênes et al. 2017) was confined mostly inside the solar circle, i.e., within about 8 kiloparsecs (kpc) of the Galactic center, and that it occupied a small fraction of the volume occupied by the atomic gas. The total mass of the latter is about $7 \times 10^9 M_{\odot}$. The atomic gas extends much further out than the molecules, to 20 kpc in the Milky Way.

By about this same time (the middle of the twentieth century), most astronomers had arrived at the view that star formation was an ongoing process, driven primarily by the work of Bethe (1939) and others showing that starlight was powered by nuclear fusion. The high luminosities of O and B stars convinced Bethe that such stars had to have formed recently (by astronomical standards), less than a few hundred million years ago. Our current understanding of stellar evolution indicates that stars of 40 or more solar masses live only 4 million years. Since we observe about 10,000 such stars in the Milky Way, the current estimate is that about two solar masses worth of stars are born every year (Chomiuk & Povich 2011).

1.1 The Phenomenology of the Interstellar Medium (ISM)

The ISM provides the constituents from which stars form, including both molecules of gas, and dust grains. The total mass within $R \leq 60$ kpc of the Galactic center is $M = 4.6 \times 10^{11} M_{\odot}$. Baryons provide $M = 9.5 \times 10^{10} M_{\odot}$ with a gas fraction of 13%. The HI mass is $M = 8 \times 10^9 M_{\odot}$, the warm ionized medium contributes $M = 2 \times 10^9 M_{\odot}$, and molecular gas is $M = 2.5 \times 10^9 M_{\odot}$ (Kalberla & Kerp 2009, p. 35). The hot ionized gas, with temperatures of order 10^6 K or higher, contains little mass, but occupies most of the volume for heights more than one kpc above the disk mid-plane (near the mid-plane, it fills only about 20% of the volume).

1.1.1 Warm Ionized Gas

Regions of warm ionized gas where the gas temperature exceeds several thousand Kelvin (Kalberla & Kerp 2009, p. 47), are common in the inner disk, and are often referred to as HII regions. Warm ionized gas is also seen above and below the neutral gas in the outer disk. Observers see HII regions surrounding massive O stars. The radiation given off by these “rock stars” of the universe is enough to dissociate any molecules, and even strip electrons off protons. These ionized electrons then share their energy (the difference between the energy of the photon that ionized the host atom and the ionization

potential of that host) with the surrounding gas, heating it. I will discuss the radiation from massive stars in Section 1.2.2. The ionized layers overlying the neutral disk at large radii are heated by the cosmic ultraviolet background radiation.

1.1.2 Neutral Gas

Neutral hydrogen, which is traced observationally by its 21-cm line emission (short radio wave), exists in a variety of environments. The densities range from $1 - 10^{-4}$ particles cm^{-3} . Temperatures range from 10 K to temperatures as high as $10^3 \sim 10^4$ K. As Peter Kalberla and Jürgen Kerp succinctly state: “Studying neutral atomic hydrogen means first focusing on the thermal pressure.” (Kalberla & Kerp 2009, p. 47) Observers typically differentiate the neutral gas by temperature, referring to “warm” and “cold” neutral gas. While it is often assumed that the gas is in both thermal and pressure equilibrium, recent work suggests a more dynamic picture, with nearly half the neutral gas in a thermally unstable region (Heiles & Troland 2003).

The width of the 21-cm emission line varies dramatically from sight line to sight line. Along sight lines with the narrowest lines, the width is consistent with thermal broadening. However, in many directions, it is clear that the emitting gas is undergoing large scale high velocity flows, producing linewidths in excess of 30 km s^{-1} .

Warm Neutral Medium (WNM)

There are a multitude of processes that contribute to the “high” temperature of the WNM in the ISM; for example, heating from hydrodynamic and magnetohydrodynamic processes, heating due to interstellar shocks, heating due to soft X-rays and stellar radiation, longward of the Lyman limit. A key take away from this list is that heating in the ISM is dependent upon location within the ISM. In addition, the efficiency of heating depends upon the phase of the material: different heating and cooling mechanisms determine the temperature of the gas, depending upon the current temperature, density and ionization of the medium (Kalberla & Kerp 2009, p. 48). The velocity dispersion in the WNM is $\Delta v \simeq 24 \text{ km s}^{-1}$ (Kalberla & Kerp 2009, p. 49), corresponding to the line

of sight velocity dispersion of $\vec{\sigma}_{\text{los}} \approx 10 \text{ km s}^{-1}$. This is comparable to the thermal line width.

Cold Neutral Medium (CNM)

In contrast to the WNM, the velocity dispersion in the CNM is $\Delta v \simeq 4 \text{ km s}^{-1}$ (Kalberla & Kerp 2009, p. 49). The CNM is heated by a variety of sources, including photoelectric heating by dust grains, by soft X-rays, and hydrodynamic and magnetohydrodynamic effects. Observers have been constrained primarily to fine structure lines, which are visible in the far infrared regime because of the low volume density of the CNM. In these regions neutral hydrogen is no longer the dominant cooling mechanism: “Owing to its low ionization potential below 13.6 eV and its high abundance, [atomic] carbon dominates the cooling of neutral gas traced by the HI 21-cm line” (Kalberla & Kerp 2009, p. 48). In addition, neutral oxygen plays a significant role in cooling neutral gas within the Galactic plane. The dispersion or line width seen in the CNM can often be much wider than can be explained by thermal motions. In other words, the gas exhibits bulk flows that are supersonic.

1.1.3 Molecular Gas

As the CNM approaches the lower temperatures listed above, molecules such as H_2 , CO and NH_3 can begin to form (Kalberla & Kerp 2009, p. 47). While H_2 is the most abundant molecule in the Milky Way, and indeed in the Universe, it is very difficult to detect. Since it is symmetric, it has no dipole moment, and as a result it does not radiate efficiently. However, molecular hydrogen is often accompanied by the second most abundant molecule, CO . In order for either molecule to exist in appreciable abundances, the molecules must not be exposed to large fluxes of Lyman-Werner photons (with energies between 11.2 and 13.6 eV), which are capable of dissociating the molecules. Photons of slightly lower energies can dissociate CO molecules, so the latter are usually found slightly deeper into molecular clouds, inside a protective molecular hydrogen envelope.

Molecular gas accounts for only 10% of the total gas mass in the entire Milky Way

Galaxy. However, much of the molecular gas is inside the Solar Circle (inside the radius from the Galactic Center to our Sun, about 8 - 8.5 kpc). Molecular gas accounts for half or more of the gas mass inside the Solar Circle.

Giant Molecular Clouds

Soon after the discovery of interstellar CO by Wilson et al. (1970), it was realized that most of this emission originated from discrete regions, both on the sky, and in velocity space. These regions came to be called clouds. Much later, Solomon et al. (1987) showed that the bulk of this gas is in large clouds, with masses upwards of $\approx 10^6 M_\odot$. These massive clouds are known as giant molecular clouds (GMCs).

Larson (1981) examined early catalogs of GMCs and extracted three laws, now known as Larson's laws. It was later realized that only two of the laws were independent—the third could be derived from the other two. The most famous law relates the size of a GMC and the linewidth of that cloud:

$$\left(\frac{\sigma}{\text{km s}^{-1}}\right) = 1.10 \left(\frac{L}{\text{pc}}\right)^{0.38}, \quad (1.1.1)$$

where σ is the dispersion velocity, and L is the characteristic size of the cloud. Larson found a similar relation for the interiors of many of his clouds, i.e., the clouds were composed of substructures that had similar properties to those found on the largest (cloud) scale. More recent work finds a somewhat larger exponent relating the linewidth to the scale of the observed region, with values clustering around 0.5.

Larson interpreted this result as evidence that the interstellar medium was turbulent, and that the linewidth reflected a turbulent cascade. He connected this with the Kolmogorov scaling for sub-sonic turbulence

$$\sigma \sim L^{1/3}. \quad (1.1.2)$$

On large scales the linewidth exceeds the thermal linewidth, indicating that the motion is supersonic, a point Larson appreciated and commented on. Typical Mach numbers for large GMCs are $\mathcal{M} \approx 10$ in the Milky Way, with much larger values seen in more rapidly star forming galaxies.

Simulations of supersonic turbulence find a relation of the form $\bar{\sigma} \sim L^{1/2}$, where $\bar{\sigma}$ is the dispersion velocity, and L is the length scale on which the velocity dispersion is measured. This again suggests that the observed linewidths reflect supersonic motions in the ISM.

Larson also showed that the linewidth scaled with the mass of the GMC

$$\left(\frac{\sigma}{\text{km s}^{-1}}\right) = 0.42 \left(\frac{M}{M_{\odot}}\right)^{0.20}. \quad (1.1.3)$$

The size-linewidth relation, with a slightly larger exponent (~ 0.5) has been recovered by dozens of groups over the last thirty years, e.g., Solomon et al. (1987); Rosolowsky et al. (2008); Miville-Deschênes et al. (2017).

Clumps and cores

As Larson noted, GMCs are not the only structures identified in the ISM. Williams et al. (2000) argue that the ISM has structure on all scales, as would be expected if turbulence dominated the kinematics of the gas. Despite the connection they make between the observed properties of the ISM and turbulence, Williams et al. (2000) do pick out two scales other than that of GMCs, which they call clumps and cores. This nomenclature has infiltrated the literature.

They define clumps on a purely observational basis: “Clumps are coherent regions in l - b - v space, generally identified from spectral line maps of molecular emission.” The quantities l and b refer to Galactic longitude and latitude, while ‘ v ’ refers to the observed velocity of the line emission.

This is in contrast to their definition of cores, which makes reference to a physical property, namely being gravitationally bound: “Cores are regions out of which single stars (or multiple systems such as binaries) form and are necessarily gravitationally bound.”

1.1.4 Deviations from Larson’s laws in massive star forming regions

A surprising and suggesting result was obtained by Caselli & Myers (1995), who measured linewidths in massive cloud cores, in which massive stars were forming. In contrast to

measurements on larger scales, and on lower mass cores, the massive cores had a modified size-linewidth relation,

$$\left(\frac{\sigma}{\text{km s}^{-1}}\right) = 0.72 \left(\frac{R}{\text{pc}}\right)^{0.21}, \quad (1.1.4)$$

to be compared with their result for low mass star forming cores

$$\left(\frac{\sigma}{\text{km s}^{-1}}\right) = 0.64 \left(\frac{R}{\text{pc}}\right)^{0.52}. \quad (1.1.5)$$

Following the results of Caselli & Myers (1995), Plume et al. (1997) observed 150 massive star forming regions, using a 30m telescope. They did not even see a statistically relevant line width-size relation; the line width was nearly independent of the size of the core they observed. However, they did find that the line width increases with density; since the density was seen to increase with decreasing radius (the usual result), the implication is that the turbulent line width increased with *decreasing* radius, the opposite of Larson’s law.

1.2 Where Are Stars Born?

How do observers know where stars form? Before the 1970’s there were no efficient far-infrared detectors. Until recently it was impossible to find individual proto-stars, because the regions where they form are optically thick: the visible light from proto-stars is severely diminished. Since observers couldn’t look for young stars directly, they used proxies or tracers instead. The two most commonly used tracers are free-free emission, and far infrared emission.

1.2.1 Star formation tracers

Free-free emission arises from ionized gas. When radiation of sufficient energy hits molecular or atomic gas, it dissociates molecules and ionizes atoms, e.g., it strips electrons from hydrogen atoms, leaving protons. The liberated electron then shares its kinetic energy (the difference between the energy of the photon and 13.6 eV, in the case of a hydrogen atom) with the surrounding gas. As the electron loses energy, it heats the gas,

and emits free-free radiation. The free-free emission is created as the electrons encounter protons and are decelerated, leading to the other name for such emission, bremsstrahlung (“braking radiation”). The associated gas temperatures are around 7,000-10,000 Kelvin.

Free-free emission is associated with recombination radiation, which is emitted when electrons are recaptured onto hydrogen or other ions. Recombination produces H_α and H_β line emission in the optical band, as well as H_{109} and similar radio recombination lines. Emission from other ions, such as [OII] and [OIII] (the square brackets denote ‘forbidden’, or non-dipole, atomic transitions), is also produced. Regions that produce emission from ionized gas are called HII regions. In the Milky Way it is difficult to detect the optical recombination lines, since ISM dust readily absorbs such radiation. However, the optical emission lines are widely used as a star formation tracer in external galaxies. The radio recombination lines are not affected by extinction, but they are very weak, particularly in comparison to the free-free emission.

The most common source of ionization in the Galaxy is radiation from massive ($\sim 40 M_\odot$) stars, which, as we saw above, are less than about 4 Myrs old. Hence free-free emission is a tracer of star formation.

The fact that optical and UV emission is absorbed by dust results in the other most widely used star formation tracer, far infrared (FIR) emission. Starlight (mostly from massive stars, since they dominate the luminosity of a cluster of young stars) heats dust grains, which re-radiate the energy as thermal radiation, typically with temperatures of tens of Kelvin.

More recently, it has become possible to use near- or mid-infrared space-based telescopes to identify proto-stars via their infrared light excess. This occurs when the light from a proto-star hits the surrounding accretion disk. Dust in the accretion disk absorbs the stellar radiation, and then re-emits it in the infrared and far infrared. Thus proto-stars appear far brighter in the near or mid-IR than do more evolved stars of the same mass or luminosity.

1.2.2 Correlation between Free-Free & CO and between FIR & CO

Observations of the galactic plane looking at free-free emission and CO emission show that the two tracers are well correlated on large ($\gtrsim 10$ pc) scales; the same is true of free-free and FIR emission (Scoville & Good 1989; Mooney & Solomon 1988). In particular, HII regions are embedded in much larger CO emitting regions. Images suggest that the hot stars appear to have dissociated or expelled the molecular material in the immediate vicinity of the star cluster that produces the ionizing radiation. Subsequent work by a very large community of astronomers, too numerous to cite, has confirmed that star formation takes place in the densest clumps of GMCs.

1.3 Star formation

Having established that star formation takes place in GMCs, I now very briefly sketch the current large scale picture of star formation. GMCs in the Milky Way have masses ranging from about 10^4 to $10^7 M_\odot$ (ten thousand to ten million solar masses), and are observed to form anywhere from hundreds up to 50,000 M_\odot of stars, the latter exemplified by Westerlund 1 (Andersen et al. 2017).

Astronomers believe (and I will show below) that portions of these GMCs collapse, initially due to turbulent motions, and later under their own gravity. The central parts of the collapsing regions eventually become dense enough that radiation cannot escape; further collapse simply heats the gas. Eventually, the central temperature reaches several to ten million degrees, initiating thermonuclear reactions. At this point, a nascent star is born.

Observations tell us that most of these young stars are surrounded by flattened gas discs. To paraphrase author Terry Pratchett, this is truly “the start of things” astronomical. Recent studies of *Kepler* planetary systems have shown that at least 1 out of 3 stars have planets (Zhu et al. 2018); therefore, at least 1 out of 3 discs contains planets.

1.3.1 Star Formation Efficiency (SFE)

Stars are believed to be responsible for regulating the amount of gas in galaxies – by driving winds out of galactic disks – as well as for the ejection of heavy elements into the intergalactic medium. In doing so, stars regulate the total fraction of gas that ends up in stars and planets.

Observations of galaxies have shown that, at most, only one quarter of the gas available to a given galaxy is converted into stars, e.g., McGaugh et al. (2010); for most galaxies, the fraction is much smaller. Why this should be, and how the fraction is determined, is currently one of the most important topics in astrophysics.

One measure of how effective nature is at converting molecular gas into stars is the star formation efficiency (SFE), denoted by ϵ :

$$\epsilon = \frac{M_*}{M_{\text{gas}}}, \quad (1.3.1)$$

where M_* is the total mass in stars and M_{gas} is the total mass in gas, in a given region.

A second measure of efficiency is how much gas turns into stars in a free-fall time. If we imagine an isolated cloud of gas with constant density, $\rho(\vec{r}) \rightarrow \rho$, we can derive the amount of time required for the cloud of gas to collapse to a single point. This time is the free-fall time:

$$t_{\text{ff}} = \sqrt{\frac{3\pi}{32G\rho}}, \quad (1.3.2)$$

where $G = 6.67 \times 10^{-8} \text{ g}^{-1} \text{ cm}^3 \text{ s}^{-2}$ is Newton's constant. At this point it will be useful to introduce the dynamical time and the virial parameter of a gas cloud. The dynamical time is given by

$$\tau_{\text{dyn}} \equiv \frac{|\vec{v}|}{R}, \quad (1.3.3)$$

where R is the size of the cloud (often taken as the square root of the area of the cloud divided by π) and v is the turbulent velocity (or the sound speed if the motions are subsonic). The dynamical time is essentially the time required for information to spread through the system. The virial parameter is

$$\alpha_{\text{vir}} \equiv 5 \frac{|\vec{v}|^2 R}{GM}, \quad (1.3.4)$$

where M is the mass of the cloud and \vec{v} is the line of sight velocity. The virial parameter is the ratio of two times the total kinetic energy over the potential energy. If the virial parameter is of order unity, then the system is gravitationally bound.

Note that for a uniform density cloud,

$$\alpha_{\text{vir}} = \frac{15}{4\pi} \left(\frac{t_{\text{ff}}}{\tau_{\text{dyn}}} \right)^2 \quad (1.3.5)$$

In the simple model where gravity is the only force acting, if all of the gas collapses to a point in a free-fall time, then the SFE would be 100%. The question we need to answer, is does this zeroth-order model hold observationally, and if not, what physics dominates the dynamics?

1.4 Star Formation on the Galactic Scale, The Kennicutt-Schmidt Law

In fact, the star formation time on galactic scales is long when compared to the dynamical time. Kennicutt (1998) expressed this in the form

$$\dot{\Sigma}_* = \eta \Sigma_g \tau_{\text{DYN}}^{-1} \quad (1.4.1)$$

where $\dot{\Sigma}_*$ is the star formation rate per unit area, Σ_g is the gas surface density, τ_{DYN} is the local dynamical time, and $\eta = 0.017$ is the efficiency factor. The gas surface density is used in this expression (as opposed to the gas volume density) as the surface density is a value which can be found observationally. In addition, the gas surface density also appears in the denominator of the Toomre Q parameter which is used to determine the gravitational stability of protostellar accretion disks.

In our rather naive model, if the gas self-gravity dominates the dynamics, $\eta \sim 1$, so the low efficiency of star formation is surprising. More recent work has refined this and similar relations in regard to its dependence on molecular gas (Bigiel et al. 2008) and by taking into account the error distributions of both $\dot{\Sigma}_*$ and Σ_g (Shetty et al. 2013), but the best current estimates of the efficiency of star formation on galactic scales remains low.

1.5 Star Formation on the GMC scale

Whether this low efficiency applies to scales comparable to giant molecular clouds, with radii of order 100 pc, is debated in the literature. The analog of equation (1.4.1) for a GMC or clump is

$$\dot{\Sigma}_* = \epsilon_{\text{ff}} \Sigma_g t_{\text{ff}}^{-1}. \quad (1.5.1)$$

Heiderman et al. (2010), Lada et al. (2010), Wu et al. (2010), and Murray (2011) find efficiencies $\epsilon_{\text{ff}} \approx 0.1$ or higher, while Krumholz & Tan (2007) and Krumholz et al. (2012a) find $\epsilon_{\text{ff}} \approx 0.01$. On these small scales, observations also suggest that the efficiency is not universal, but instead varies over two to three orders of magnitude, e.g., Mooney & Solomon 1988; Scoville & Good 1989; Lee et al. 2016).

There are a number of explanations for the low star formation rate, on either small or large scales (although they may not be necessary for the former!). These include turbulent pressure support (Myers & Fuller 1992), support from magnetic fields (Strittmatter 1966; Mouschovias 1976), and stellar feedback (e.g. Dekel & Silk 1986).

Numerical experiments investigating turbulence and magnetic fields suggest that, while magnetic support found in MHD simulations can slow the rate of star formation compared to hydrodynamics simulations, neither turbulence nor magnetic support is sufficient to limit the small scale star formation rate to 1-2% per free fall time (Wang et al. 2010; Cho & Kim 2011; Padoan & Nordlund 2011; Krumholz et al. 2012b; Myers et al. 2014; Burkhardt et al. 2015; Mocz et al. 2017).

1.6 Review of Analytic Theories of Star Formation

I summarize analytic theories of star formation, and what each individual step has indicated for our understanding of this process. Beginning in the late 1960's, star formation theory was the idea that clumps destined to form stars started in hydrostatic equilibrium (HSE). The gas in a cloud was assumed to be supported against its self gravity via thermal pressure support. The idea, expressed by Shu among others, was that something, perhaps the conversion of atomic H to molecular H₂, removed the thermal support at

small radii, and the cloud then collapsed to form a star.

1.6.1 Larson (1969) and Penston (1969)

Larson (1969) and Penston (1969) first put forth the idea that the collapse of this core could be described by a self-similar solution.

Larson, in his numerical experiments, began with a sphere of gas with uniform density and temperature initially independent of radius. The initial velocity was zero everywhere, but clearly the gas was not in hydrostatic equilibrium. His numerical integration showed that the density approached a power law, density $\rho \sim 1/\bar{r}^2$, with a core of constant density at small (and shrinking) radii. At a fixed time, at small radii, the region where $\rho \propto \bar{r}^0$ is called the core.

These initial conditions are somewhat artificial, leading Shu (1977) to wonder how the system could have zero velocity while experiencing a non-zero net force.

Larson (1969) finds that at any given instance in time, at small radii the infall velocity decreases with decreasing radius. He also finds that the density approaches a constant at small radii, with the result that $\dot{M} \propto \bar{r}^3$. The mass accretion rate decreases with decreasing radius, at small radii.

It is difficult to extract \dot{M} at large radii from this early published numerical work. However, the numerics were enough to motivate the authors to seek a self-similar analytic solution to describe the results.

For example, Larson (1969) presents a simple self-similar analytic model. In contrast to his numerical model, which had a small infall velocity at large radii, in his analytic model the velocity approaches a constant value, with a Mach number of 3.28, at large radii. The density $\rho \propto c_s^2/r^2$, and this provides a mass accretion, $\dot{M} \propto c_s^3/G$. In other words, the mass accretion at large radii does not depend upon the radius. Note that this asymptotic result applies well inside the outer boundary.

Larson (1969) noted the fact that at small radii, the solution was such that the pressure gradient is a reasonable fraction (0.6) of gravity (see his equation C10).

1.6.2 Shu (1977)

Shu (1977) found that the solution described by Larson (1969) and Penston (1969) was premised on a physically artificial initial condition. One of the issues with the model was the assumption that the flow at large radii be directed inwards at velocity $\vec{v} \rightarrow 3c_s$ as $\vec{r} \rightarrow \infty$. Shu argued that this property is non-physical, nor was it apparent that the flow could stably transition from supersonic to subsonic motion, and then to rest. In addition, only specific initial and boundary conditions could lead to the Larson-Penston flow. Shu (1977) went on to show that the flow during collapse does exhibit self-similar properties described in Larson (1969). To rectify the issue with the boundary condition, Shu (1977) explicitly assumed that the cloud is hydrostatic for radii larger than $r = c_s t$. At $t = 0$ a perturbation causes the central region to collapse. For regions where $r < c_s t$, the layers find that their pressure support has disappeared and begin to fall inwards. This collapse expands outwards in time, leading to the phrase “inside-out collapse”. Following this solution, Shu (1977) estimated the accretion rate onto stars by assuming that stars form from hydrostatic cores supported by thermal gas pressure. The accretion rate in his model was independent of time, given by $\dot{M} = m_0 c_s^3 / G$, where $c_s = (k_b T / \mu)^{1/2}$ is the sound speed in molecular gas, and $m_0 = 0.975$. Shu (1977) predicted a maximum accretion rate of $\sim 2 \times 10^{-6} M_\odot \text{ yr}^{-1}$.

1.6.3 Myers & Fuller (1992)

Shu’s predicted maximum accretion rate is too small to explain the origin of massive ($M_* \sim 50 - 100 M_\odot$) O stars, which have lifetimes $\lesssim 4 \times 10^6$ yrs, but would take 50 Myrs to grow, according to his model. Myers & Fuller (1992) overcame the difficulty with low accretion rates by noting that high mass star forming regions had linewidths much larger than thermal motions could produce. They continued to assume the initial condition was that of a hydrostatic core that is supported by turbulent pressure. Myers & Fuller (1992) also followed Shu (1977) in assuming that there is an expanding collapse wave, but that

the velocity was not c_s , but rather the sum:

$$\sigma^2 = \sigma_T^2 + \sigma_{NT}^2, \quad (1.6.1)$$

where σ_T is the thermal velocity and σ_{NT} is the turbulent or nonthermal velocity.

For radii where the non-thermal velocity dominates the line-width,

$$\dot{M}_* = m_o \mathbf{v}_T^3 / G, \quad (1.6.2)$$

where \mathbf{v}_T is the velocity inferred from the observed linewidth. This is larger than Shu's estimate by a factor of the Mach number cubed, \mathcal{M}^3 ; since the Mach number is often of order 5 or higher, the predicted accretion rates are two orders of magnitude larger than those predicted by Shu (1977).

They also assumed that the turbulence is static and unaffected by the collapse, i.e. $\vec{v}_T(\vec{r}, t) \rightarrow \vec{v}_T(\vec{r})$. McLaughlin & Pudritz (1997) and McKee & Tan (2003) made similar assumptions, and found the same result.

Collectively, these models, (Shu 1977; Myers & Fuller 1992; McLaughlin & Pudritz 1997; McKee & Tan 2003), are referred to as inside-out collapse models; the collapse starts at small radii (formally at $\vec{r} = 0$ in the analytic models) and works its way outward, at the assumed propagation speed (c_s or $\vec{v}_T(\vec{r})$). At any given time, the infall velocity and mass accretion rate both decrease with increasing radius \vec{r} . The analytic models assume the existence of a self-similarity variable $x = r/vt$, where $v = c_s$ in Shu (1977) or the turbulent velocity $\vec{v}_T(\vec{r})$ in Myers & Fuller (1992); McLaughlin & Pudritz (1997); McKee & Tan (2003). These models predict velocity and mass accretion profiles very different than those seen in the simulations of Lee et al. (2015).

1.7 Current Numerical simulations and Observations

Numerical experiments investigating the effects of turbulent pressure and magnetic fields suggest that neither turbulence nor magnetic support is sufficient to reduce the rate of star formation to $\eta \approx 0.02$ on small scales (Wang et al. 2010; Cho & Kim 2011; Padoan & Nordlund 2011; Krumholz et al. 2012b; Myers et al. 2014). Feedback from radiative

effects and protostellar jets and winds may be able to explain the low star formation rate, but the impact of these forms of stellar feedback remains uncertain despite recent progress (Wang et al. 2010; Myers et al. 2014; Federrath 2015).

The following subsections are intended to give the reader a general feel for the state of the field. It is not an extensive, much less complete review.

1.7.1 Krumholz & McKee - The Berkeley Group

The group that I refer colloquially to as the Berkeley Group have typically simulated a turbulent core model. McKee & Tan (2003) present evidence that massive-star forming regions are supersonically turbulent, and show that the molecular cores, out of which individual massive stars form, are as well. The motivation behind this model is the recognition that massive stars form in regions of very high pressure and density.

The Berkeley group performed radiation hydrodynamic simulations using ORION, (Krumholz et al. 2009), and found that the radiation pressure emitted by a simulated massive prestellar core does not halt mass accretion.

Myers et al. (2014), actually has some of the same results that I present in this paper, namely that $M_*(t) \propto t^2$. Figure 7 presents the star formation efficiency vs free-fall time. While the authors fit a tangent line to determine the slope, their data presents the $M \propto t^2$ relation that I have found.

Li et al. (2018) create simulations using magnetic fields, radiative and outflow feedback. They present the SFE vs free-fall time in their Figure 9 and note that their data also shows the same $M \propto t^2$ relation that I find in Chapter 2. In addition, they also find in their Figure 4, that the density goes to $\rho \propto \bar{r}^{-3/2}$.

1.7.2 Klessen & Mac Low Group

One of the major questions in implementing turbulence in numerical simulations is how one decides to drive it. There are two ways in which one can drive turbulence, either solenoidally, think stirring cream into a cup of coffee, or via compression, think clapping your hands together. Depending upon the choice of driver, or even mixture of the two, one

might drastically change the simulated results. So, what choice of driving method best models the turbulence seen in the ISM, and in GMCs in particular? This question was resolved when Federrath et al. (2010b) showed that irrespective of the type of forcing, they found velocity dispersion-size relations consistent with observations, and independent numerical simulations. They found that the forcing they used did not change the physical relations at smaller scales.

Federrath et al. (2010b) achieved this by using high resolution simulations of pure solenoidal and pure compressive turbulence. In addition, they ran several lower resolution simulations with varying mixtures of the drivers. Federrath et al. (2010b) found that, “although likely driven with mostly compressive modes on large scales, turbulence can behave like solenoidal turbulence on smaller scales.” The turbulent cascade had reached equipartition, of 2:1 solenoidal to compressive.

Previous work by the group had found that under typical GMC conditions global collapse could be prevented, but strong shocks would become gravitationally unstable and collapse to presumably form stars (Klessen et al. 2000).

1.7.3 Lee et al. (2015)

Lee et al. (2015) showed that, in simulations with no feedback, the star formation efficiency on parsec scales is not constant in time. This is in contrast to previous work, which had implicitly assumed that the star formation rate on small scales was constant. In particular, many authors have assumed that the star formation rate in their simulations of a GMC (or smaller cloud or part of a cloud) was given by equation (1.4.1), where ϵ was assumed to be constant. Lee et al. (2015) showed that $\epsilon \propto t$, which implies that $M_* \propto t^2$, where M_* is the total stellar mass.

Lee et al. (2015) emphasized that the star formation efficiency on parsec scales is nonlinear in time, i.e., $\epsilon \propto t \rightarrow M_* \propto t^2$, on small scales, where M_* is the total stellar mass. Using a detailed numerical simulation, they showed that this nonlinear star formation rate is driven by the properties of collapsing regions. In particular, they demonstrated that the turbulent velocity near or in collapsing regions follows different scaling relations than does

turbulence in the global environment, which follows Larson’s law, $\vec{v}_T(\vec{r}) \sim \vec{r}^{1/2}$ (Larson 1981). They also showed that the density PDF is not log-normal, but rather develops a power law to high density. The power law tail to the PDF was hinted at in much earlier simulations by Klessen (2000) and shown convincingly, as well as explained, by Kritsuk et al. (2011).

The increasing rate of star formation found by Lee et al. (2015) is important in that it may provide an explanation for the observed range in star formation rates on small scales. It suggests that the star formation rates on small scales vary in part because of the age of the star forming region; slow star forming regions, with very low instantaneous efficiencies, will ramp up their stellar production over time. If this result can be firmly established, it will highlight the need for a form of very rapid feedback. In particular, since the dynamical time in massive star forming regions is much smaller than the time delay of ~ 4 Myrs between the start of star formation and the first supernovae, rapid star formation on small scales would have to be halted by some form of feedback other than supernovae.

The simulations of Lee et al. (2015) explicate the link between the rate of star formation with the gravitational collapse of high density regions, which is an analytically well studied problem.

1.7.4 Murray & Chang (2015)

Motivated by this discrepancy between observation and the current analytical models, Murray & Chang (2015), hereafter MC15, developed a 1-D model of spherical collapse that treats the turbulent velocity, \vec{v}_T , as a dynamical variable and does not assume that the initial condition is a hydrostatically supported region. They used the results of Robertson & Goldreich (2012) on compressible turbulence; the evolution of the turbulent velocity in a collapsing (or expanding) region is described well by the following equation:

$$\frac{\partial \mathbf{v}_T}{\partial t} + \mathbf{u}_r \frac{\partial \mathbf{v}_T}{\partial r} + \left(1 + \eta \frac{\mathbf{v}_T}{\mathbf{u}_r}\right) \frac{\mathbf{v}_T \mathbf{u}_r}{r} = 0 \quad (1.7.1)$$

The first two terms are the Lagrangian derivative, and \mathbf{u}_r is the radial infall velocity. The first term in the brackets describes the turbulent driving produced by the infall, while

the second is the standard expression for the turbulent decay rate; η is a dimensionless constant of order unity.

MC15 used this in place of an energy equation. Together with the equations for mass continuity and momentum, equation (1.7.1) gives a closed set of equations that can be solved in spherical symmetry numerically. In addition, they were able to analytically show that the results of their calculations gave density and velocity profiles that appear to be in line with both recent numerical calculations (Lee et al. 2015) and observations (e.g., Caselli & Myers 1995; Plume et al. 1997).

To summarize, MC15's major results were:

- The gravity of the newly formed star introduces a physical scale into the problem, which MC15 called the stellar sphere of influence, \vec{r}_* . This is an idea familiar from galactic dynamics. The radius \vec{r}_* is where the local dynamics transitions from being dominated by the mass of the gas to being dominated by the mass of the star. As a result, the character of the solution, in particular that of the velocity, differs dramatically between $\vec{r} < \vec{r}_*$ and $\vec{r} > \vec{r}_*$. The existence of this physical scale modifies the form of the self-similarity on which inside-out theories rely.
- The small scale density profile is an attractor solution. MC15 showed numerically and argued analytically that at small scales, the density profile is an attractor solution. In particular, MC15 showed the density profile asymptotes to:

$$\rho(\mathbf{r}, t) = \begin{cases} \rho(r_0) \left(\frac{\mathbf{r}}{r_0}\right)^{-3/2}, & \mathbf{r} < \mathbf{r}_* \\ \rho(r_0, t) \left(\frac{\mathbf{r}}{r_0}\right)^{-k_\rho}, & k_\rho \approx 1.6 - 1.8 \quad \mathbf{r} > \mathbf{r}_*(t). \end{cases} \quad (1.7.2)$$

where r_0 is some fiducial radius.

- The existence of \vec{r}_* implies that the infall and turbulent velocities have different scaling for $\vec{r} < \vec{r}_*$ and $\vec{r} > \vec{r}_*$. In particular, MC15 showed

$$\mathbf{u}_r(\mathbf{r}, t), \mathbf{v}_T(\mathbf{r}, t) \propto \begin{cases} \sqrt{\frac{GM_*(t)}{\mathbf{r}}} \sim \mathbf{r}^{-1/2} & \mathbf{r} < \mathbf{r}_*(t) \\ \sqrt{\frac{GM(\mathbf{r}, t)}{\mathbf{r}}} \sim \mathbf{r}^{0.2} & \mathbf{r} > \mathbf{r}_*(t), \end{cases} \quad (1.7.3)$$

Thus the scaling of the turbulent velocity differs from that predicted by Larson’s law ($\propto r^{1/2}$) inside the sphere of influence. In other words, the turbulent velocity in massive star forming regions will deviate from Larson’s law, which has long been observed, but without theoretical explanation.

- The stellar mass increases quadratically with time. This result arises naturally from the attractor solution nature of the density profile at small \vec{r} , Equation 1.7.2, and the scaling with Keplerian velocity for the turbulent and infall velocities at small \vec{r} , Equation 1.7.3.

The mass accretion rate:

$$\dot{M}(\mathbf{r}, t) = \begin{cases} 4\pi R^2 \rho(R) \mathbf{u}_r(\mathbf{r}, t), \sim t \mathbf{r}^0 & \mathbf{r} < \mathbf{r}_* \\ 4\pi R^2 \rho(R) \mathbf{u}_r(\mathbf{r}, t) \sim t^0 \mathbf{r}^{0.2} & \mathbf{r} > \mathbf{r}_*. \end{cases} \quad (1.7.4)$$

MC15’s predictions for $\vec{r} < \vec{r}_*$ could not be checked using the simulations of Lee et al. (2015) as those fixed grid simulations were too coarse.

1.7.5 Galaxy Scale Simulations

Until very recently, galaxy-scale or larger (cosmological) simulations were not able to reproduce the Kennicutt-Schmidt relation. Nor did the cosmological runs reproduce correctly the mass of stars in galaxies of a given halo mass, despite including supernova and other forms of feedback, e.g., Guo et al. (2010); Governato et al. (2010); Piontek & Steinmetz (2011). To overcome this low resolution driven problem, Hopkins et al. (2011, 2012) performed high resolution (few parsec spatial, few hundred solar mass particle masses) simulations of isolated galaxies, modeling both radiative and supernovae feedback (among other forms). They recovered the Kennicutt-Schmidt relation, a result that they showed was independent of the small-scale star formation law that they employed. The simulations in the second paper also generated galaxy scale outflows or winds, removing gas from the disk, thus making it unavailable for star formation. When the feedback was turned off, the star formation rate soared, demonstrating that in the simulations at least, feedback was crucial to explaining the Kennicutt-Schmidt relation, and the outflows.

Simulations including supernovae but lacking the radiative component of the feedback did not exhibit strong winds and so overproduced stars.

Cosmological simulations employing unresolved (or “sub-grid”) models for both radiative and supernovae feedback are now able to reproduce the halo-mass/stellar mass relation (e.g., Aumer et al. 2013; Hopkins et al. 2014; Agertz & Kravtsov 2015). Again, these simulations *require* stellar feedback to drive the winds that remove gas from the disk, so as to leave the observed mass of stars behind.

1.8 What this Dissertation Does Not Cover

There are a number of groups whose observational, statistical, and analytical, contributions and theories I have not covered. I do not intend to attempt to create an extensive review.

1.8.1 Missing Physics

Our current understanding of star formation suggests that the effects of magnetic fields, radiation from stars, and the heating and cooling rates of the gas can all have significant effects on both the rate of star formation and the initial mass function (IMF) of the stars. We do not include any of this physics in the simulations described in this paper. The simulations presented in this dissertation are focused upon turbulence in hydrodynamic simulations and the effects of protostellar jets.

It is often argued that the turnover in the IMF, somewhere between 0.2 and $0.6 M_{\odot}$, is associated with the thermal Jeans mass of the gas in the collapsing region. There have been other proposed explanations, for instance, Padoan & Nordlund (2002) found that the IMF depends upon turbulent fragmentation, however, this is hard to understand because turbulence does not have a scale associated with it. Krumholz et al. (2016) state that on small scales the dominant mechanism limiting fragmentation of gas is the thermal pressure. They state that this thermal pressure is influenced by stellar radiation: as the gas fragments and collapses the opacity of the gas grows trapping the radiation from

the young stars, leading to a change in temperature of the gas, increasing the thermal pressure. This picks out a mass scale. If so, then our use of an isothermal equation of state suggests that the IMF found in our simulations is likely to be in error. However, as Figures 2-5 and 11 show, both \vec{u}_r and \vec{v}_T exceed c_s , except at the earliest times ($\sim 100,000$ yrs before a star forms), and then only for $\vec{r} \lesssim 0.1$ pc, so that the gas pressure does not dominate the dynamics in most regions and most of the time.

We have undertaken and made some preliminary analyses of magnetohydrodynamic simulations, which we will report on in future publications; as seen by other authors, we find that magnetic fields slow the star formation rate. But the runs of density and velocity have the same qualitative form in our MHD simulations as in the hydro runs presented here, and the MHD runs also give $M_*(t) \sim t^2$.

Radiative feedback will also affect both the IMF and, for massive enough stars, the dynamics of the collapse at late times (after massive stars have formed). Massive stars can emit high velocity winds, up to 3000 km s^{-1} , as these winds leave the star they create shocks when the wind runs into the surrounding gas. Due to the collision of the wind and surrounding gas, the gas heats up to $10^8 - 10^9$ K. The pressure associated with these high temperatures will push the surrounding gas away from the star.

All the figures we show present results for stars with masses no larger than about $4 M_\odot$. To estimate the effects of radiation, we compare the force from the Reynolds stress $\mathbf{F}_T = 4\pi r^2 \rho \mathbf{v}_T^2$, to the radiation force L/c . From Figure 11, the (averaged over many stars) v_T is slightly in excess of 1 km s^{-1} at $r = 0.01$ pc, while from any of the density figures the density is $\rho \approx 5 \times 10^{-18} \text{ g cm}^{-3}$. The force from Reynolds stress is then $F \approx 4 \times 10^{26}$ dynes. The luminosity of a 4 solar mass star on the zero age main sequence is $L \approx 2 \times 10^{36} \text{ erg s}^{-1}$ (Schaller et al. 1992), so the radiation force $L/c \approx 3 \times 10^{25}$ dynes, about a 10% effect. The force from Reynolds stress increases outward, see Figure 13, so this statement holds at larger radii as well.

Thus we expect that the effects of radiation pressure are not particularly significant in the situations we report; the run of density and infall velocity, and hence the $M_*(t) \sim t^2$ scaling should not be affected, at least up to the times we are reporting on. We note,

however, that this estimate neglects the effect of radiative or ionization heating which is an important feedback mechanism.

Simulations including radiative feedback support this simple analysis. Figure 15 of Myers et al. (2014) shows that in their simulations, which include feedback from both protostellar outflows and radiation (as well as magnetic fields), the stellar mass increases as the square of the time, up to masses of $\sim 4.5 M_{\odot}$. Earlier work by the Berkeley group found similar results, forming stars with 10 solar masses, with $M_*(t) \sim t^2$ even for such massive stars, see Figure 13 of Krumholz et al. (2012b). Their simulations included radiative effects, but no protostellar winds.

This dissertation describes my contributions to various parts of our current understanding of the dynamics of star formation. This chapter gives a brief overview of the theory behind star formation and notes gaps in our current understanding. Ch. 2 discusses the initial set up for the majority of my simulations, and the dynamics of gravitational collapse with no feedback or other delaying aspects. Ch. 3 discusses the effects that protostellar and jet feedback have on the stellar mass accretion rate for a cluster of stars. Finally, in Ch. 4, I summarize the results obtained in this dissertation.

Chapter 2

Hydrodynamic Simulations

“If we keep demanding that God yield up His answers, perhaps some day we will understand them. And then we will be something more than clever apes, and we shall dance with God.”

— Marc Robichaux, *The Sparrow*
by Mary Doria Russell

In this chapter we will keep demanding answers to questions about star formation, in hopes that we will eventually come to understand how stars form. Motivated by the nonlinear star formation efficiency found in recent numerical simulations by a number of workers, we performed high-resolution AMR simulations of star formation in self-gravitating turbulently driven gas. As we followed the collapse of this gas, we found that the character of the flow changes at two radii, the disk radius \vec{r}_d , and the radius \vec{r}_* where the enclosed gas mass exceeds the stellar mass. Accretion starts at large scales and works inwards.

If the equations are non-dimensionalized, two dimensionless variables appear, the Mach number \mathcal{M} and the virial parameter $\alpha_{vir} \equiv 5|\mathbf{v}_T|^2 R/GM_{box}$, e.g., Mihalas & Mihalas (1984). We want to model massive star forming regions in the Milky Way, so we choose the Mach Number $\mathcal{M} = 9$ and the virial parameter $\alpha_{vir} = 1.9$ respectively (Solomon et al. 1987). In addition, we choose the size of the box $L = 16\text{pc}$, and the sound speed $c_s = 0.264\text{kms}^{-1}$, so that the turbulent velocity lies approximately on the observed

size-line width relation, Larson’s law. These choices fix both the density and the mass scale.

The simulations described in this chapter disregard several physical effects. They do not include magnetohydrodynamics, radiative, stellar wind, or protostellar jet feedback. While the feedback physics I neglect in this chapter can have significant effects on both the rate of star formation and the initial mass function (IMF), I aim to address the role the random motions captured by the Reynolds stress play in the dynamics of gravitational collapse in turbulent fluids.

Our equation of state is that of an isothermal gas. While we have stated in 1.8.1 that radiation and temperature effects can play a significant role, assuming an isothermal gas is a reasonable approximation. The cooling timescale associated with the environment we simulate is much much shorter than the dynamical time of the system. This means that even though the gas will heat up via shocks etc, the gas rapidly cools well before it affects the dynamics significantly. This dissertation will not address whether thermal effects play a role in setting the initial mass function of stars, e.g Larson (2005). With this in mind, we relegate the discussion of the IMF to the appendix of this chapter, as the details are unlikely to be reliable.

This chapter is organized as follows. In Section 2.1 we describe our numerical methods and simulation setup. In Section 2.2 we present and analyze the results of our simulations. In particular, we make detailed comparisons with the results of MC15. We discuss our results and compare them to previous work in Section 2.3

2.1 Detailed Simulations of Turbulent Collapse

Most of the simulations described in this chapter use the adaptive mesh refinement code FLASH version 4.0.1 (Fryxell et al. 2000; Dubey et al. 2008) to model self-gravitating, hydrodynamic turbulence in isothermal gas with three-dimensional (3D) periodic grids and a minimum of 8 levels of refinement on a root grid of 128^3 , giving an effective

resolution of $32,768^3$. Following Lee et al. (2015) our FLASH runs use the Harten-Lax-van Leer-Contact Riemann solver and an unsplit solver (Lee et al. 2009). We have also extensively used the RAMSES code (Teyssier 2002), but unless explicitly stated otherwise, the results in this chapter come from FLASH simulations.

As just mentioned, we start with a box with the physical length set to $L = 16$ pc using periodic boundary conditions. We fill the box with molecular hydrogen (H_2). The initial mass density is $\rho = 3 \times 10^{-22} \text{ g cm}^{-3}$ (number density of hydrogen molecules $n \approx 100 \text{ cm}^{-3}$), corresponding to a mean free-fall time $\bar{\tau}_{\text{ff}} \approx 3.8 \text{ Myrs}$; the total mass in the box is $M \approx 18,000 M_{\odot}$. The sound speed is set to $c_s = 0.264 \text{ km s}^{-1}$. We use pure molecular hydrogen in this simulation so the ambient temperature $T \approx 17 \text{ K}$.

To initialize our simulations, we drive turbulence by applying a large scale ($1 \leq kL \leq 2$, corresponding to $1.3 - 2.7$ pc) fixed solenoidal acceleration field as a momentum source term. We use solenoidal driving because it is known that compressive turbulence increases the star formation rate compared to solenoidal driving (Federrath et al. 2008). We apply this field in the absence of gravity and star particle formation for 3 dynamical times until a statistical steady state is reached. The resulting Mach number is $\mathcal{M} = 9$, i.e a turbulent velocity of $\vec{v}_{\text{T}} = 2.37 \text{ km s}^{-1}$.

Stirring the initial turbulence using a fixed driving field is a technique used by a number of workers in the field (Padoan & Nordlund 2011; Collins et al. 2011). Other groups initialize the turbulence by initializing the velocity field with Gaussian random perturbations having some assumed power spectrum (Myers et al. 2014; Skinner & Ostriker 2015). While neither of the resulting velocity fields are generated the way the turbulence in the interstellar medium (ISM) of our Galaxy is, the stirring allows one to perform simulations which have nontrivial initial density structures and velocity fields that are at least reminiscent of those inferred from observations of the interstellar medium of our Galaxy.

Federrath & Klessen (2012) use a time varying driving field to produce random motions. They argue that a time-varying driving field allows one to avoid large spatial correlations that would result from a fixed driving field acting for a time longer than the

dynamical time of the simulation box. In our simulations we do not run for longer than a box dynamical time after turning on star formation. We run for $\sim 700,000$ yrs, about 0.18 dynamical times, after the first star forms. The limiting factor on the length of the runs was our available compute time. Hence, we do not expect the large scale turbulent flow to vary much over such a short time. In addition, there is some evidence (Federrath et al. 2010b) that the results of turbulent driving are not sensitive to the exact large-scale mechanism.

This fully developed turbulent state is the initial condition to which we add self-gravity and star particle formation for our star formation experiments. We enable AMR to follow the collapse of over-dense regions. Even after turning on star formation, we continue to drive the large scale fixed solenoidal acceleration field.

To follow these collapsing regions, we have implemented an algorithm for mesh refinement in these simulations, similar to that of Federrath et al. (2010a). In supersonically turbulent flows, certain regions rapidly increase in density. For a given density and temperature, or sound speed, regions larger than the Jeans length

$$\lambda_J \equiv \sqrt{\frac{\pi c_s^2}{G\rho}} \approx 3.5\text{pc} \quad (2.1.1)$$

are prone to gravitational collapse. Our base grid's resolution of $N_{\text{root}}^3 = 128^3$ gives a cell length of 1.25×10^{-1} pc which is sufficient to resolve the Jeans length for the mean density.

In most of our simulations, the AMR grid is refined when the Truelove et al. (1997) criterion

$$\lambda_J \leq N_J \Delta x, \quad (2.1.2)$$

is met. In this expression Δx is the cell length, and N_J is an integer; Truelove et al. (1997) found that in order to avoid artificial fragmentation, one requires $N_J \gtrsim 4$. This condition states that if the Jeans length is less than the specified number of cell lengths, we need to refine to the next level.

This corresponds to a condition on the density

$$\frac{\rho}{\rho_0} = 45 \cdot 4^l \left(\frac{N_{\text{root}}}{128}\right)^2 \left(\frac{N_J}{4}\right)^{-2} \left(\frac{16\text{pc}}{L}\right)^2 \times \left(\frac{c_s}{0.265 \text{ km s}^{-1}}\right)^2 \left(\frac{3 \times 10^{-22} \text{ g cm}^{-3}}{\rho_0}\right) \quad (2.1.3)$$

where l is the refinement level, with $l = 0$ corresponding to the root grid. When this density condition is met the local grid is refined by a factor of 2, provided that the maximum refinement level has not been reached. When the transition to the maximum refinement level is triggered i.e. when l goes from 7 to 8 (the maximum refinement level), the density contrast is $\rho/\rho_0 \approx 10^6$.

At the end of this chapter we describe a number of test simulations in which we refined the grid when $N_J = 4, 8, 16$ or 32 (Federrath et al. 2011). We show that many of the quantities in our runs, including the density and the mass accretion rates, are converged for $N_J = 4$.

The maximum dynamic range is a little larger than 6 orders of magnitude, because we allow the density to increase further before forming star particles. When the Truelove criterion is exceeded by a factor of three at the highest refinement level, the excess mass in a cell is transferred either to a newly created star particle or to a star particle whose accretion radius includes the cell. The factor of three allows only the highest density regions to form star particles. It is inspired by the work of Padoan & Nordlund (2011) whose sink particle formation criteria of $8000 \times$ mean density is a factor of 3-4 above the Truelove criteria at their highest resolution of 1000^3 . Additionally, the 3 cells immediately around a star particle can rise above this density criterion. This is done so that we do not form star particles within 2 cells of each other. Instead these close surrounding cells can only accrete onto the previously formed star particle. We should also note that like our previous work in Lee et al. (2015), our star particle creation prescription is different from the prescription of Federrath et al. (2010a) where additional checks are performed; in the appendix we present the results of runs in which we used these additional checks, finding that they do not affect the t^2 scaling of the stellar mass, or the dynamics of the infall.

To calculate the gravity, we use the same algorithm as described in Lee et al. (2015), which we now briefly describe. To compute the self gravity on gas, we first map star particles to the grid and then use a multi-grid Poisson solver (see Ricker 2008), coupled with a fast-Fourier transform (FFT) solution on the root grid, to solve for gravity. To compute the gravitational acceleration on the star particles, we first compute the particle-particle forces using a direct N-body calculation. To compute the particle-gas forces, we use the same multigrid solver (with root grid FFT) on the grid, but with the star particle *unmapped*. As a result, two large scale gravity solutions (one with and one without mapped star particles) must be found per timestep as opposed to one. This allows us to avoid the computationally expensive task of computing gas-star particle forces via direct summation. As discussed in Lee et al. (2015), this splitting of particle-particle and particle-gas/gas-particle forces does not strictly obey Newton’s second law, breaking down on order the size of the smallest grid cell. As a result, errors in the orbits of particles may result. However, we believe that our runs are short enough to avoid buildup of significant errors.

In the FLASH runs, to obtain a useful number of star particles with long accretion histories, we have taken the initial turbulent box and have only run our refinement algorithm (and hence, star particle algorithm) on only one octant at a time. This forces us to run eight high resolution simulations, each on a different octant and so allows us to treat each octant as a separate distinct simulation. This is necessary as FLASH does not have individual timesteps, which results in the code grinding to a halt once a single region collapses.

2.2 Results

In Figure 1 we show a projection along the z-axis of the entire simulation volume for one of the high resolution octant simulations, 2.8 Myr after gravity has been turned on. The image shows up to 8 levels of refinement, giving an effective resolution of 32768^3 , or a minimum cell size of 5×10^{-4} pc. Regions that are highly refined are the densest regions,

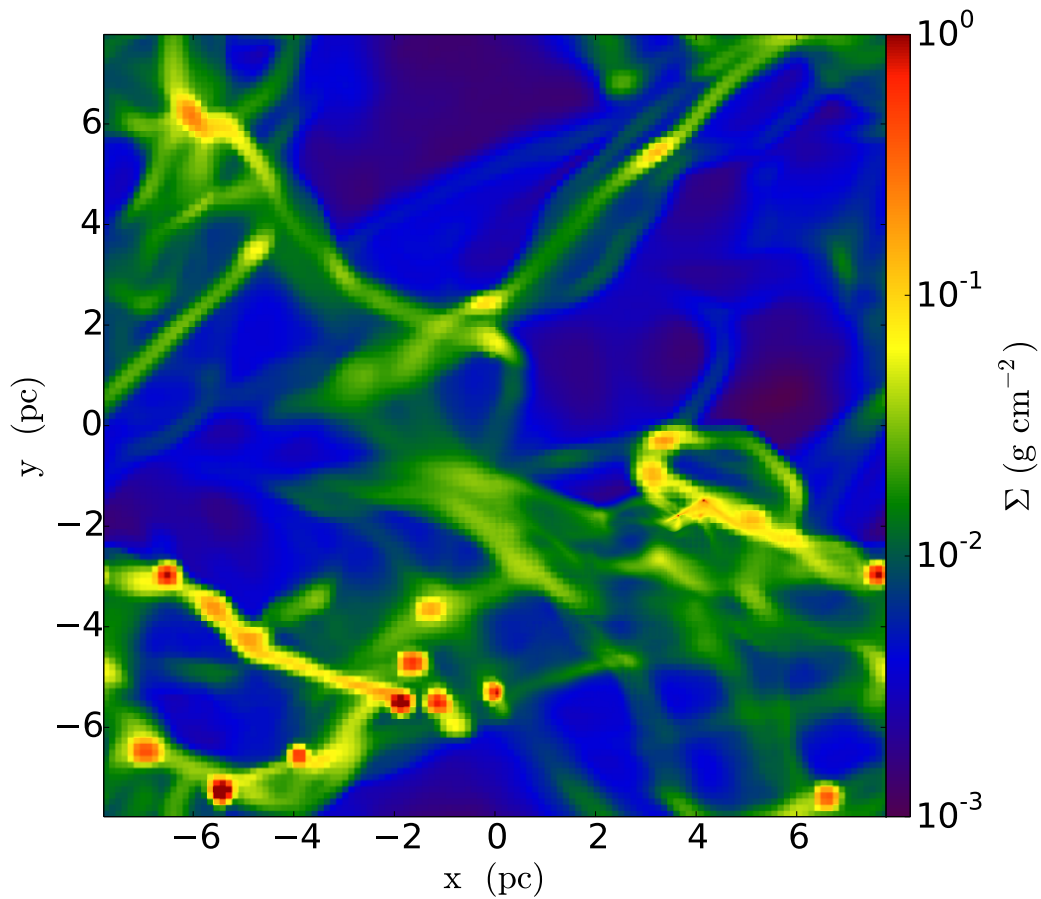


Figure 1 : Projection of the density along the z -axis of the entire simulation volume. The root grid is 128^3 with up to 8 levels of refinement, giving an effective resolution of 32768^3 . This snapshot is taken 2.8 Myr after star formation was turned on.

for which the image is smoother than the low-density more pixelated regions. Note that the highly refined regions are limited to the lower right, which is the octant that this particular simulation focused on. The other seven simulations refine the other octants.

The high density regions are organized into filaments. These filaments span most of the simulation box, with lengths up to several parsecs and widths of order a few tenths of a parsec. Some filaments appear to flow into large clumps. This is in accord with many previous simulations, e.g., (Padoan et al. 1998; Lee et al. 2015). These clumpy regions have the highest densities and, hence, are the first to fulfill the criterion for star particle formation.

In this section we focus on the regions around two individual star particles, which we refer to as particle A and particle B.

Particle A formed about a quarter of a parsec away from its nearest neighbor star particle. At the end of the run it was $\sim 736,000$ years old and had a mass of $\sim 17.5 M_{\odot}$, although it was still accreting rapidly.

Particle B formed and remained in isolation. At the end of the run, the particle was $\sim 512,000$ years old and had a mass of $\sim 10.7 M_{\odot}$. Throughout the simulation particle B had a steady supply of gas.

2.2.1 The Run of Infall ($|\vec{u}_r|$), Circular (\vec{v}_{ϕ}), and Random Motion (\vec{v}_T) Velocities

Figure 2 shows the infall, $|\vec{u}_r|$, circular, \vec{v}_{ϕ} , and random motion, \vec{v}_T , velocities as a function of radius (top panel) and the density in a slice of the local volume (bottom panel) around the density peak that will form particle A 100,000 years in the future. In Appendix 2.5.1, we describe how we calculate each of these velocities.

We will compare \vec{v}_T to what MC15 referred to as a turbulent velocity. Our current definition of \vec{v}_T is simply that of a random velocity. We are agnostic about whether or not \vec{v}_T characterizes an isotropic turbulent pressure; close examination of the velocity field indicates that the random motions are not isotropic on the scale of their distance from the density peak. It is also clear, however, that \vec{v}_T characterizes a Reynolds stress that does provide a net outward support against gravitational collapse. This follows from a simple energy argument; the infall velocity in the vicinity of the density peak is well below the local free-fall velocity, and remains so throughout the simulation, even after a star particle forms. Thus, some of the potential energy released by the infall goes into some channel other than inward motion. A fraction of the potential energy release goes into shocks, and in our code is effectively removed immediately. At this early stage, the rotational motion represents a small fraction ($\lesssim 10\%$) of the energy at all but the smallest radii. But the inward flattening of the green line in Figure 2, and the inward increase seen in later figures, shows that a substantial fraction of the potential energy released by the

inflow goes into random motions. By energy conservation, this fraction is not available to the inflow, so that $|\vec{u}_r|$ is smaller than it would be if the random motions were not absorbing some of the energy. This shows that there is an effective outward force on the infalling gas.

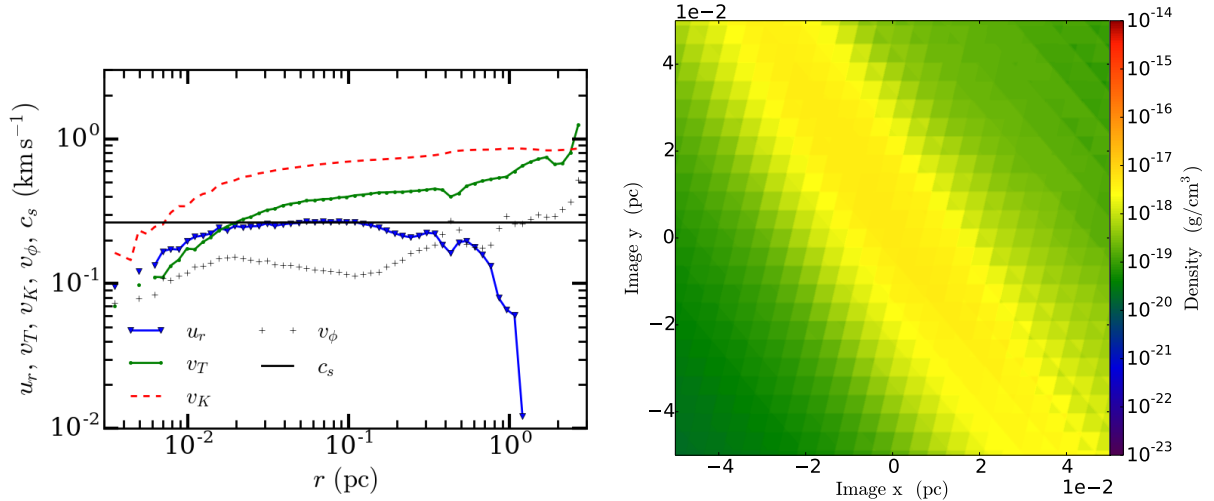


Figure 2 : The left plot shows the run of velocity with radius measured from the density peak; this density peak will develop into particle A in 100,000 years. The sound speed is the black horizontal line while the infall velocity $|\vec{u}_r|$ is given by the blue triangles, connected by a solid blue line. The green circles connected by a solid green line show \vec{v}_T while the black crosses show the rotational velocity \vec{v}_ϕ . The red dashed line is the Keplerian velocity $\vec{v}_K \equiv \sqrt{GM(\vec{r})/\vec{r}}$. Even at this early stage the structure is far from hydrostatic equilibrium, as the infall velocity is $\sim 25\%$ of the free-fall velocity. The refinement level is $l = 6$, which corresponds to a cell size of $\sim 2 \times 10^{-3}$ pc. The right plot shows the density in a slice along the direction of the angular momentum vector centered on that peak.

The infall velocity, $|\vec{u}_r|$, and random motion (\vec{v}_T) velocity are similar in magnitude, and somewhat smaller than the Keplerian velocity, $\vec{v}_K = \sqrt{GM(<\vec{r})/\vec{r}}$. Note that $|\vec{u}_r|$ is roughly equal to the sound speed while \vec{v}_T is supersonic. The fact that the infall velocity is $\sim 25\%$ of the free-fall velocity over all radii less than a parsec shows that this system is not in hydrostatic equilibrium. The density distribution is smooth and filamentary. The run of density versus radius, not shown, is a simple power law with a small inner core.

Figure 3 shows the region around the same density maximum some 70,000 years later, 30,000 years before star particle A forms. Once again the infall velocity is a substantial fraction of the Keplerian velocity, showing that the core remains far from hydrostatic

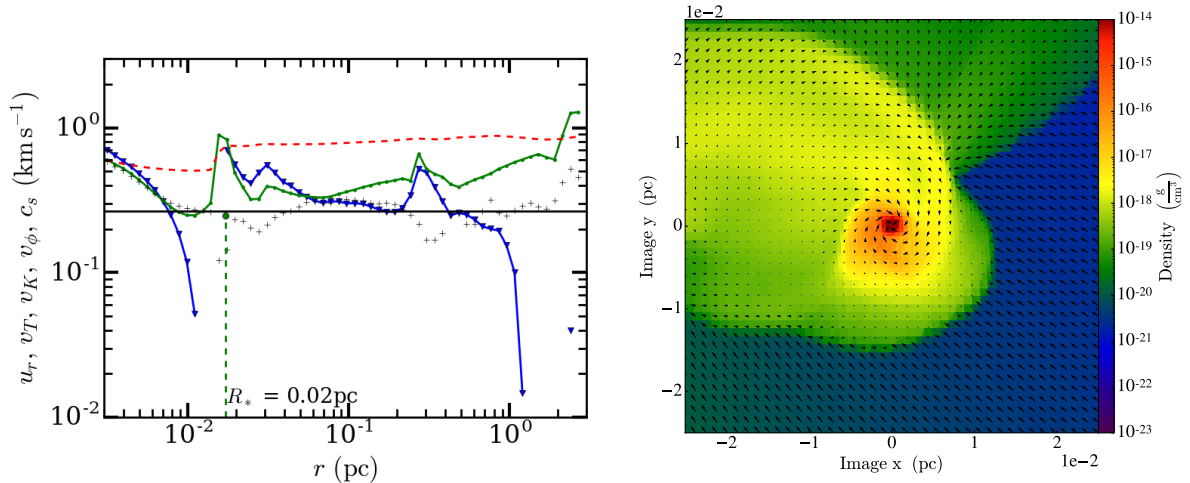


Figure 3 : The left panel shows the run of velocity around the same density peak as that shown in Figure 2, but now only $\sim 30,000$ years before the formation of particle A . The color and linestyles are the same as in the left panel of Figure 2. The right panel again shows the density in a slice centered on the density peak. The plotted arrows show the velocity in the plane of the slice. The longest arrows correspond to roughly 2 km s^{-1} . In the intervening $\sim 70,000$ years since the time shown in Figure 2, an accretion disk-like structure has formed, which has a mass of $\sim 0.7 M_\odot$. The radius of the sphere of influence (of the disk) is ~ 0.02 pc. All three velocities, \vec{v}_T , \vec{v}_K , and \vec{v}_ϕ , increase inward of \vec{r}_* ; the inflow is disrupted at $\vec{r} \sim 0.015$ pc a feature that we interpret as a shock, where the flow meets the nascent accretion disk, at which point \vec{v}_T also drops in magnitude. At yet smaller radii the infall resumes, because at this early time the disk is not yet fully rotationally supported. The resolution at the location of the star particle has reached the refinement limit $\Delta x = 5 \times 10^{-4}$ pc; the errors in the calculation of the velocities that are associated with the finite resolution are substantial inside $\vec{r} \approx 0.002$ pc, so features inside this radius are not reliable, and thus not plotted.

equilibrium. However, \vec{v}_ϕ in the innermost regions (inside 0.01 pc) is comparable to both \vec{v}_K and \vec{v}_T , showing that the innermost region is partially rotationally supported. The density slice, shown in the right panel of Figure 3, confirms this interpretation, showing a disk-like structure with a radius of order ~ 0.01 pc. The mass inside this radius is $\sim 0.7 M_\odot$. We note that the particle forms near the tip of a filament (not shown).

2.2.2 The Stellar Sphere of Influence

We begin by developing an operational definition of \vec{r}_* . We choose to define \vec{r}_* as the radius where the enclosed mass, $M(< \vec{r}, t)$ is three times the mass of the star, i.e.,

$$3M_*(t) = M(< \mathbf{r}_*(t), t) \quad (2.2.1)$$

similar to Murray & Chang (2015). We chose the factor of 3 to ensure that the gravity of the gas dominates the gravity of the star.¹ In particular, the factor of 3 essentially means that the mass in gas is twice the mass of the central mass (star and disk) and implies that the gravitational acceleration of the gas is twice that of the central mass. This radius is where the dynamical effects of the gas begins to dominate the dynamical effects of the central mass.

Equations (1.7.2), (1.7.3), and (2.2.1) predict that the character of the solution should change at \vec{r}_* and that \vec{r}_* increases with time. Our numerical results support this prediction. Figure 4 shows that \vec{v}_T decreases with decreasing radius down to \vec{r}_* and then increases with decreasing radius inside the sphere of influence. We see that \vec{v}_T reaches a minimum near $\vec{r} = \vec{r}_*$. The inward decrease in $\vec{v}_T(\vec{r})$ is not monotonic near 0.2 pc, probably due to a shock, as suggested by jumps in both the infall and random velocities, and in the density, at $\vec{r} \sim 0.02$ pc. This trend of increasing \vec{v}_T with decreasing radius inside \vec{r}_* is repeated in Figure 5.

We don't see an increase in the infall velocity for $\vec{r} > \vec{r}_*$ for this object because the star particles are forming about 1 pc from the end of a filament, but we do see an increase in $|\vec{u}_r|$ in other particles, see below.

Comparing Figure 4, which shows the velocity and density of the same region 24,000 years after star particle A forms, with Figure 3 demonstrates that the radius of the change in character of the flow associated with \vec{r}_* increases over time. In particular, the global minimum of the random motion velocity is now at 0.06 pc rather than somewhere between 0.01 – 0.02 pc.

The drop in $|\vec{u}_r|$ at large radii in Figure 4 reflects the vagaries of the large scale Reynolds stress pressure gradient; we already mentioned that this particle is forming near the end of a filament.

Figure 5 shows the velocities and the density in a slice centered on particle B, 100,000

¹The gas in the disk around the protostar is rotationally supported, so it essentially acts as a part of the star. We include the mass of the disk when calculating \vec{r}_* and discuss how we define the disk mass in 2.2.5.

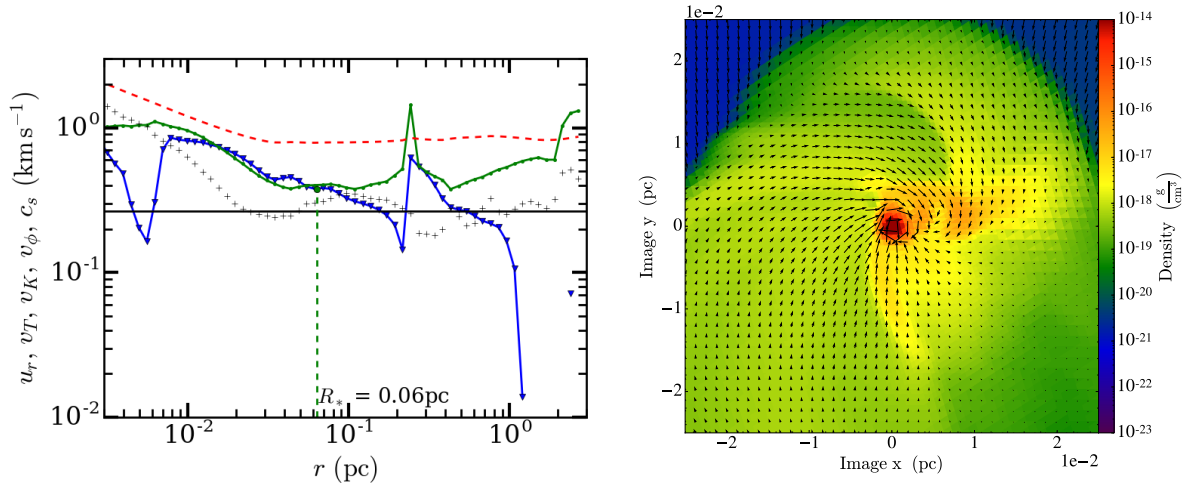


Figure 4 : The run of velocity (left panel) of particle A 24,000 years after star particle formation. The color and linestyles are the same as in the left panel of Figure 2. This panel shows that the disk around the particle is rotationally supported for $r \lesssim 5 \times 10^{-3}$ pc; inside that radius, the black pluses are higher than either the green or blue points, i.e., the rotational velocity is larger than either the random motion or infall velocity. The radius of the sphere of influence is $r_* \sim 0.06$ pc. The star mass is $2.47 M_\odot$ and the disk mass is $0.58 M_\odot$, thus the disk is about 23% the mass of the star. The bottom panel is a density slice centered on particle A, in the center of mass frame, face-on to the rotationally supported disk. The arrows show the velocity in the plane of the slice. The longest arrows correspond to nearly 3 km s^{-1} . With a cell size of $\Delta x = 5 \times 10^{-4}$ pc, we have ~ 20 cells across the diameter of the disk.

years after that star particle forms. This star is more isolated than particle A, and as a result $|\vec{u}_r|$ increases from $\vec{r} \gtrsim \vec{r}_*$ out beyond $\vec{r} \approx 3$ pc. This is in accord with equations (1.7.3) and (1.7.4), but it contrasts with the result in Figure 4.

The behavior of $|\vec{u}_r(\vec{r})|$ at large radii is not set by the collapse dynamics, but rather by the properties of the random motions, most importantly the outer scale of the Reynolds stress gradient. In particular, we do not expect $|\vec{u}_r(\vec{r})|$ to be significant on scales larger than some moderate fraction, say $1/4$, of the outer scale. In our simulations, the outer scale is given by $k = 2$, or $L/2$, and we use solenoidal stirring, so that the cascade starts out with no compressive component, although one develops as the cascade proceeds. In fact we will show in §2.2.7 that the typical radius of a converging region is more like $\vec{r} \approx 1$ pc in our simulations.

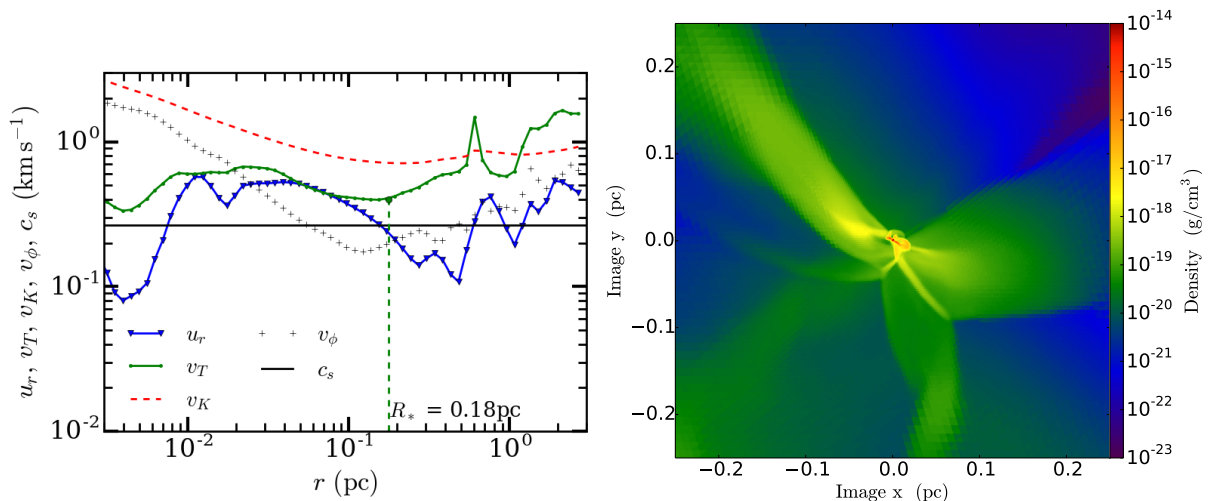


Figure 5 : The left panel shows the run of velocity for particle B $\sim 100,000$ years after formation. The radius of the sphere of influence is ~ 0.18 pc. The stellar mass is $4.5 M_\odot$ and the disk mass is $2.47 M_\odot$ so the disk is $\sim 55\%$ of the stellar mass. The right panel shows the density in a slice centered on particle B .

2.2.3 A Fixed Point Attractor for $\rho(\vec{r}, t)$ Inside \vec{r}_*

One of the most striking findings of MC15 was that the run of density is independent of time for $\vec{r} < \vec{r}_*$. Our simulations confirm that finding, as illustrated in Figure 6. The plot shows the run of density for two separate times. The dotted blue line shows the run of density $\sim 40,000$ years before particle A forms, while the solid green line is the run of density $\sim 540,000$ years after the star particle forms. The elapsed time corresponds to nearly two tenths of the mean free-fall time of the box, and to many free-fall times at radii less than a tenth of a parsec. We emphasize that the density can change on the local free-fall time, which is much smaller than the global free-fall time (by a factor of 10 or more for $\vec{r} < 0.1$ pc). We will show that in fact the density inside \vec{r}_d does change rather rapidly, after the star particle forms, but that for $\vec{r}_d < \vec{r} < \vec{r}_*$ the density does not change; see §2.2.7

The mean power law slope of the density before the star forms (the blue dashed line in the figure) is $k_\rho \approx 1.9$, consistent within the star-to-star variations we see with the range $k_\rho \approx 1.6 - 1.8$ from equation (1.7.2) for $\vec{r} > \vec{r}_*$ (since in this case $\vec{r}_* = 0$).

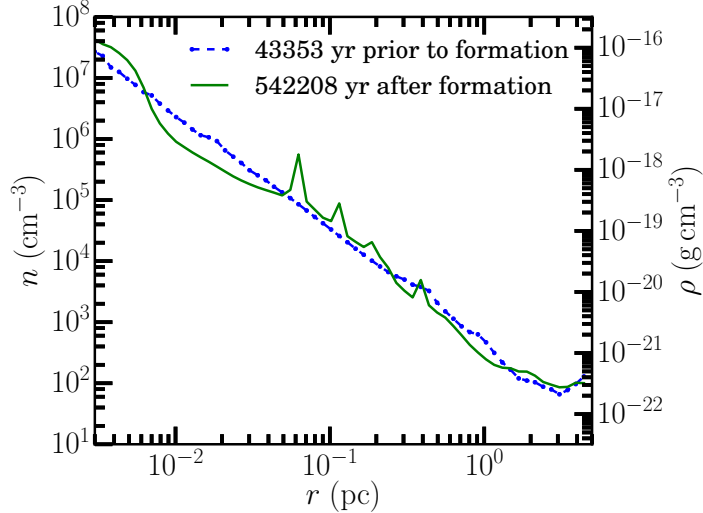


Figure 6 : The run of density for particle A . The dotted blue line is the density $\sim 40,000$ years before the star forms. The solid green line is the run of density $\sim 540,000$ years after formation. The gap in time corresponds to the free-fall time at a radius of 0.24 pc. For $\bar{r} < 0.24$ pc the range of time spanned in the plot is more than a local free-fall time, yet the density does not vary significantly. There are fluctuations in the density, e.g. the spikes around $\bar{r} \sim 0.1$ pc. In Figure 9 we average over a number of objects to remove these fluctuations: we also demonstrate that the density in the disc does increase.

2.2.4 Mass Accretion Rate

In Figure 7 we show the mass accretion rate \dot{M} as a function of \bar{r} around a star particle ($t - t_* > 0$) and from the corresponding density peak in which the star particle eventually formed ($t - t_* < 0$). This plot is taken from a RAMSES simulation. Before the star particle forms, \dot{M} decreases inward at all radii.

Following the establishment of the power law solution for the density, at $t = t_*$, a star particle forms and the \dot{M} profiles flatten at small radii. An examination of the density profile (not plotted) reveals that $\rho \propto \mathbf{r}^{-3/2}$, while for $t - t_* = 24$ kyrs, the gravitational force (and hence \mathbf{u}_r) is dominated by the central mass for $\mathbf{r} \lesssim 0.1$ pc, so that $\mathbf{v} \propto \mathbf{r}^{-1/2}$ out to that radius. We also note that while the \dot{M} profile is flat, it does increase in time as shown by the difference between the $t - t_* = 24.6$ kyrs and 154 kyrs curves. All this behavior agrees well with the prediction of Equation (1.7.4).

At all times, the accretion rate is either nearly flat or increasing with radius, which is a natural result of the near balance between gravity and Reynolds stress support, as

posited in the theory of MC15. We contrast this with an inside-out collapse model, which we exemplify using a Shu (1977) solution (blue dashed line) obtained by directly integrating equations 11 and 12 of Shu (1977) at a fixed time. The asymptotic behavior of \dot{M} follows from Shu's equations 15 and 17; recall that $x = r/(c_s t)$ is a function of the radius. In the limit of small x , \dot{M} approaches a constant. However, for large values of x , $\dot{M}(r, t) = -A(A-2)c_s^3/Gx$ (Equation [15] of Shu 1977), i.e., the mass accretion rate falls like $1/r$ at a fixed time at large r as seen in Figure 7.

In other words, for inside-out collapse models, the accretion rate is monotonically decreasing with increasing radius. This is qualitatively different from the prediction of MC15 or the results of this work. We note that while we have chosen to plot the Shu solution, other collapse solutions (McLaughlin & Pudritz 1997; McKee & Tan 2002, 2003) have the same general profile: the mass accretion rate is roughly independent of r at small radii, and decreases with increasing r at large radii.

In summary, at no time do we see any indication of an inside-out collapse in our simulated massive star forming regions.

2.2.5 Rotationally Supported Disks

Many of the qualitative and even quantitative features predicted by MC15 are found in our simulations as discussed above, including the approach of the density profile inside \vec{r}_* to an attractor solution, the minimum in the velocity profile around the sphere of influence, and the expansion of the sphere of influence with time. However, our simulations display additional dynamics that were not modeled by MC15.

A particularly interesting bit of dynamics neglected by MC15 is the development of a rotationally supported disk, which we alluded to above. This development is evident in the velocity plots, starting from the absence of a disk in Figure 2 to a proto-disk with no central star particle in Figure 3, to a fairly well developed rotationally dominated disk, at $\vec{r} \lesssim 0.05$ pc in Figure 4.

We define the outer edge of the accretion disk \vec{r}_d as the largest radius where \vec{v}_ϕ exceeds both $|\vec{u}_T|$ and \vec{v}_T , that is, where the disk is rotationally dominated. The development of

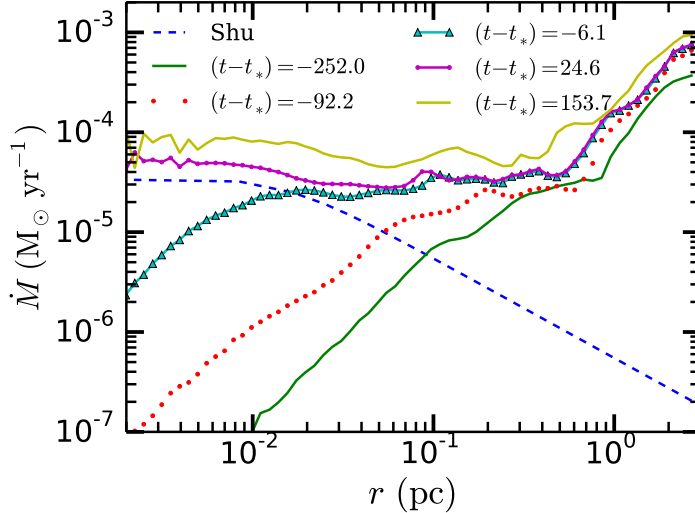


Figure 7 : The run of \dot{M} for a star particle in a simulation with $N_J = 32$ cells per jeans length resolution, at a maximum effective resolution of 16384^3 . The lowest solid (green) line is the run of \dot{M} for the density peak that will form the star particle 252,000 years after the time plotted. The accretion rate is about an order of magnitude lower at small radii (say 10^{-2} pc) than at 1 pc. The purple line connecting the dots is the run of accretion soon after the star particle forms, when the stellar mass is about a solar mass. The accretion rate at 1 pc still exceeds that at all smaller radii, showing that the collapse is outside-in, not inside-out. As an example of an inside-out collapse, we show the accretion rate for the Shu (1977) model (the dashed line) for a star of a solar mass with $A = 5.5$.

the disk is best followed by examining the rotational velocity seen in Figures 2, 3 and 4. In the last figure, $\vec{r}_d \approx 7 \times 10^{-3}$ pc. We have also used a second definition for the disk radius, i.e., where the derivative of the density has a sharp drop, see footnote 1. The two definitions of the disk radii agree well with each other.

We note that the disks in our simulation have $\vec{r}_d \sim 1,000$ AU. This is somewhat larger than the radii of the largest observed disks, e.g., Padgett et al. (1999) find $500 \text{ AU} \lesssim \tilde{r}_d \lesssim 1000 \text{ AU}$. Of course we are simulating massive star formation, and most observations of disks are of nearby, low mass stars. Another factor to keep in mind is that we are doing hydrodynamic simulations, so there are no magnetic fields, which are believed to be effective at transporting angular momentum; the inclusion of magnetic fields might therefore tend to reduce the sizes of the accretion disks in our simulations.

2.2.6 Gravitationally Unstable Disks

The plot of \dot{M} in Figure 7 shows that the accretion rate varies little across the transition from the rotationally supported disk to the radial infall dominated part of the flow at slightly larger radii. In other words, the disk is transporting angular momentum efficiently enough so that the disk accretion rate matches the rate at larger radii. Since our simulations do not include magnetic fields, this efficient disk accretion is not due to the magneto-rotational instability (Balbus & Hawley 1991, 1998).

Following Kratter et al. (2010), we suggest that angular momentum is transported via gravitational torques. We have not yet tried to calculate these torques, but as a first check, we have calculated the Toomre Q parameter, as shown in Figure 8; recall that

$$Q = \frac{\mathbf{v}_\phi \sqrt{\mathbf{v}_T^2 + c_s^2}}{\pi G r \Sigma}. \quad (2.2.2)$$

In this expression Σ is the gas surface density of the disk, \mathbf{v}_ϕ is the rotational velocity of the disk, and \mathbf{v}_T is the turbulent velocity in the disk. The Toomre Q parameter (also referred to as the Safronov-Toomre criterion) is used to determine approximately whether a razor thin disc is gravitationally unstable or not. If $Q > 1$ then the system is stable against collapse, and we would expect little angular momentum transport via gravitational torques. On the other hand if $Q < 1$ then it is at least plausible that gravitational torques can transport angular momentum and hence drive accretion. The figure shows Q for the disk around particle B at the time shown in Figure 5. For the region $3 \times 10^{-3} \lesssim \mathbf{r} \lesssim 6 \times 10^{-3}$ pc, Q is below one, which supports the notion that the efficient accretion is due to gravitational torques resulting from a gravitational instability in the disk. However, in the next section, we find results suggesting that the accretion disks in our simulation are not gravitationally unstable at all times.

2.2.7 Average Profiles

Thus far, we have focused our attention on two of our stars and shown that their \vec{v}_T , $|\vec{u}_r|$ and ρ profiles are qualitatively similar to the profiles predicted in the analytic work of MC15. Now we will show that this behavior is generic, in the sense that this is true on

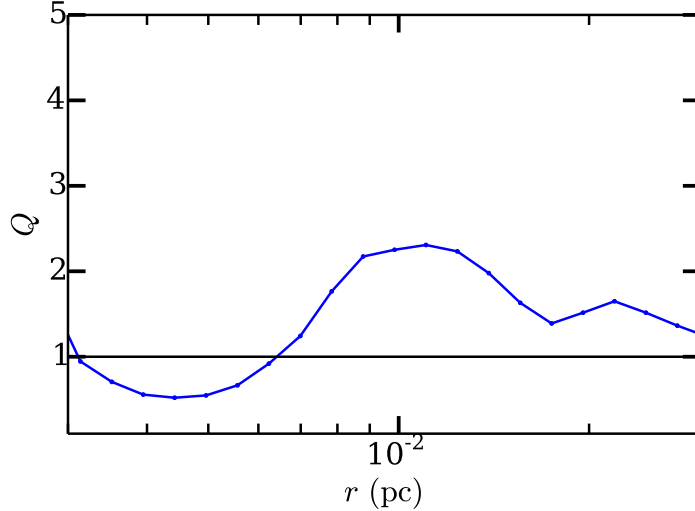


Figure 8 : The Toomre Q parameter for particle B , at the same time as shown in Figure 5: $\sim 100,000$ years after star particle formation. From Figure 5 we see that the disk is rotationally dominated for $r < 2 \times 10^{-2}$ pc. For $3 \times 10^{-3} \lesssim r \lesssim 6 \times 10^{-3}$ pc, $Q \lesssim 1$. This indicates that the disk is gravitationally unstable at these radii, while it is marginally stable at larger radii. Figure 14 provides a more representative view of disk stability.

average over all the star particles in our simulations.

At the end of our base FLASH simulations, we have found roughly 60 star particles. To study these systems in a generic way, we look at the average velocity and density profiles. Motivated by the results of MC15, we average the profiles at fixed stellar mass; by fixing the stellar mass, we fix \vec{r}_* , and hence the velocity, ρ , and \dot{M} profiles.

For epochs before a star particle forms, it is less clear how these profiles should be averaged. However, equation (1.7.2) predicts that $\rho(\vec{r}, t)$ approaches a time independent function as soon as any non-pressure supported structure, such as a disk, forms. As a result, we elect to follow the methodology in Lee et al. (2015) and average profiles at fixed times (10 and 100 kyrs) before the formation of a star particle. The choice of these two times allows us to study the conditions in the collapsing region immediately before and well before the formation of the star particle, while retaining several (six to seven) density peaks and hence reasonable statistics.

In Figure 9, we plot n as a function of \vec{r} , 10,000 and 100,000 years before star particle formation (left plot), and for stellar mass $M_* = 1$ and $4 M_\odot$ (right plot). The plots show

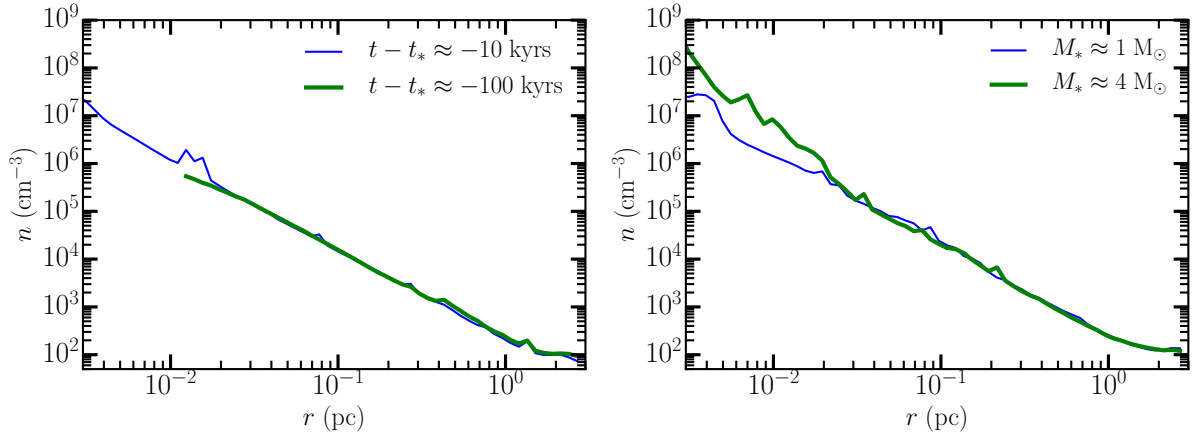


Figure 9 : Number density as a function of radius at 10,000 and 100,000 years before the star particle forms (left plot) and when the star reaches 1 and 4 M_{\odot} (right plot). For the left plot, we average over 6 and 7 regions that are within 25% of 10,000 and 100,000 years prior to star particle formation. The line corresponding to $t - t_* = -100,000$ yrs terminates at $\mathbf{r} = 0.02$ pc because that corresponds to the level of refinement for the local density peak ($n \approx 10^6 \text{ cm}^{-3}$) at that time. For the right plot, we average over 14 and 6 regions that contain 1 or 4 M_{\odot} star particles (within $0.5 M_{\odot}$). A power law fit to either curve between 0.02 pc and 1 pc gives a power law of $n \propto r^{-\kappa_{\rho}}$ with $\kappa_{\rho} \approx 1.8$. At $r = 0.1$ pc the free fall time is $\approx 250,000$ years, roughly the span of time show across the two panels of the plot. For radii between $\vec{r}_d \approx 0.02$ pc and 1 pc the density profile does not change appreciably between the left and right plots. The lack of change for $0.1 \text{ pc} \lesssim r \lesssim 1 \text{ pc}$ is unsurprising, since the elapsed time is less than the local dynamical time at these radii. However, the same cannot be said about the lack of evolution of $\rho(\vec{r}, t)$ in the range $\mathbf{r}_d < \mathbf{r} \lesssim 0.1$ pc. The collapse theories of (Shu 1977; McLaughlin & Pudritz 1997; McKee & Tan 2003) predict that the density should vary with time, but this is not what we see. Note that the density profile does increase for $\mathbf{r} < \mathbf{r}_d$; compare the green line (the $4 M_{\odot}$ profile) versus the blue line (the $1 M_{\odot}$ profile) in the right hand panel. This is consistent with mass accreting onto the disk faster than it is transported in towards the star, in such a way that $Q \approx 1$ at all times. The change in the density for $\mathbf{r} < \mathbf{r}_d$ demonstrates that the density *can* evolve on the time scale of our simulations. Thus the fact that the density *does not* change for $\vec{r}_d < \vec{r} < \vec{r}_*$ between the two plots is striking. It is, however, what is predicted by Equation (1.7.2).

that $\rho(\vec{r}, t) \rightarrow \rho(\vec{r})$ for $\vec{r}_d < \vec{r} < \vec{r}_*$, i.e., the density approaches the attractor solution, early in the collapse, and this profile persists through formation of the star particle and well after. This generalizes what we found for our two example star particles in §2.2.3.

It is important to note that the lack of change in the run of density is not due to the fact that we integrate for only a few tenths of a global free fall time. To emphasize this point, observe that the density at $\vec{r} < \vec{r}_d$ *does* increase, while the density for $\vec{r}_d < \vec{r} < \vec{r}_*$ *does not* increase with time.

The reason for the increase of $\rho(\vec{r}, t)$ with time for $\vec{r} < \vec{r}_d$ is easy to understand: the

gas is in a rotationally supported disk, which (as Figure 8 shows) is marginally unstable. As the central stellar mass grows, the mass of the disk surrounding it will grow as well, in such a way that $Q \sim M_d/M_*$, where M_d is the disk mass, is roughly constant.

The fact that the density inside \vec{r}_d increases illustrates the general point that the relevant time scale for the run of density to change can be much shorter than the global dynamical time scale. If one had to wait for a global dynamical time, the density in the disk would not change over the entire course of our simulation, but Figure 9 shows that the density in the disk does change over a tenth of the global dynamical (or free-fall) time. Thus the result that $\rho(\vec{r}, t) \rightarrow \rho(\vec{r})$ for $\vec{r}_d < \vec{r} < \vec{r}_*$ is not a result of our short (relative to the global dynamical time) integration.

The one dimensional numerical models in MC15 also showed that $\rho(\vec{r}, t) \rightarrow \rho(\vec{r})$; MC15 find that the fixed point solution is approached from outside-in (see their Figure 1). We see the same behavior in the simulations we have run with $N_J = 16$ and with $N_J = 32$. In those runs we see the flattening of the density at small radii and early times, before the star particle forms.

In simulations without self gravity we see a log normal distribution in the density probability distribution function (PDF). Robertson & Goldreich (2018) provide a conceptual picture of the physics, that I will briefly describe. In a turbulent box, one will end up with two flows that converge, creating a shock. With an isothermal simulation the temperature will not increase, but the higher density of the shock will create a pressure gradient. The net momentum of the converging flows will result in a net acceleration.

The acceleration will be of the form:

$$\mathbf{a} \approx \rho \mathbf{v}^2 / \Sigma_{\text{shock}}, \quad (2.2.3)$$

where, \mathbf{a} is the acceleration due to the net ram pressure of the flow, ρ is the upwind gas density, \mathbf{v} is the velocity of the wind relative to the shock, and Σ_{shock} is the gas surface density of the shock. The gas downstream of the shock will feel the acceleration of the shock, creating a situation where the downstream gas can reach hydrostatic equilibrium,

given by:

$$\frac{dP}{dz} = -\rho \mathbf{a}. \quad (2.2.4)$$

In the case of an isothermal ideal gas, $P = \frac{\rho}{m_p} k_b T$, plugging this into equation 2.2.4 and then integrating shows that

$$\rho \propto e^{-z/H}, \quad (2.2.5)$$

where $H = c_s^2/\mathbf{a}$ is the scale height of the region of gas downstream of the shock that is in HSE. This gives an exponential distribution, Robertson & Goldreich (2018) show how this becomes a log-normal distribution of ρ .

In Figure 10, we show the density PDF of one of our simulations. The black line shows the result for the full box. The blue thin dot-dash line shows the result when we excise a 1 pc sphere around each star particle. Finally, the thin blue dashed line shows the PDF of all the 1 pc spheres around each star particle. At high densities, the PDF exhibits power law behavior, as found by previous workers (Klessen 2000; Kritsuk et al. 2011; Lee et al. 2015). Moreover these high density regions are localized around star particles, as the PDF with 1 pc spheres excised around star particles shows (blue dot-dashed line). We also note that the regions around star particles are not devoid of low density regions, as the PDF of the 1 pc spheres around star particles (blue dashed line) shows. Kritsuk et al. (2011) first argued that the power law tail of the density PDF at high densities is related to the scaling of the density with radius; for $\rho \propto \mathbf{r}^{-\alpha}$, the density PDF $\propto \rho^{-3/\alpha}$. For the values of α ($\alpha \approx 1.5 - 2$) that we expect from analytic theory (MC15) and from previous numerical calculations (Lee et al. 2015), we expect the density pdf to scale like ρ^{-2} to $\rho^{-3/2}$. We fit a power law between $n = 10^4 - 10^9 \text{ cm}^{-3}$ (red dotted line) and find a scaling like $n^{-1.7}$, in line with these expectations.

The power law shows a break to a flatter slope at $n \approx 10^8 \text{ cm}^{-3}$. A similar break was seen by Kritsuk et al. (2011), who argued that at very high densities, the density PDF flattens due to the presence of disks, which they also found. In our simulations, we have found that material with $n > 10^9 \text{ cm}^{-3}$ always resides within 0.01 pc of a star particle. Since 0.01 pc is the typical outer radius of our simulated disks, this suggests that the highest density material is strongly associated with the disk.

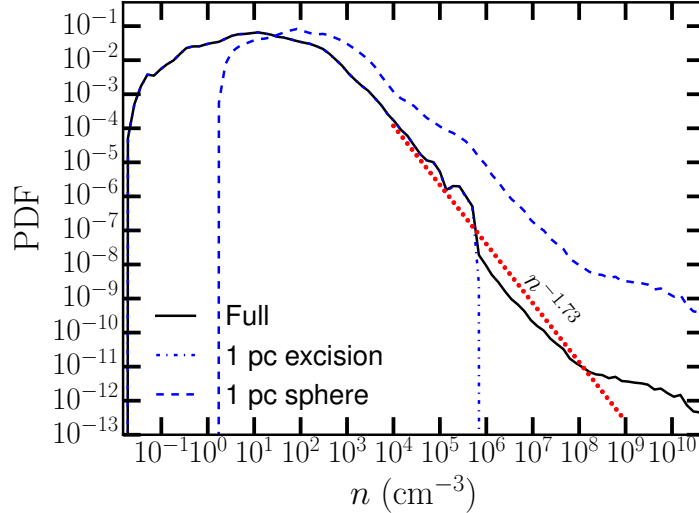


Figure 10 : The probability distribution function of n . The black thin solid line shows the full PDF, the blue thin dot-dashed line shows the PDF with 1 pc spheres cut out around star particles, and the blue thin dash line shows the PDF within those spheres. The red dotted line show the power law $\propto n^{-1.73}$.

Figure 11 shows the averaged $|\vec{u}_r|$, \vec{v}_T , \vec{v}_ϕ , \vec{v}_K as a function of \vec{r} before the star particle forms (left) and after (right panel). As in Figure 9, we have selected the same fixed times (10 and 100 kyrs) before the star particle forms and the same fixed masses (1 and $4 M_\odot$) after star particle formation. Here the dynamics of \vec{v}_T follow quantitatively the behavior of \vec{v}_T found in MC15. In MC15, \vec{v}_T scales with radius as $\mathbf{r}^{1/2}$ at very large \vec{r} , where self-gravity is not important. For example, at $t = 100$ kyrs before the star particle forms, we find that $\vec{v}_T(\vec{r}) \sim \mathbf{r}^{0.48}$, in line with Larson’s law, i.e., $\propto \mathbf{r}^{1/2}$.

However, at $t = 10$ kyrs before star particle formation, one can see that the \vec{v}_T scaling has reversed itself at small radii ($\vec{r} \lesssim 0.1$ pc) due to the accumulation of mass in a proto-disk; the gas in the disk deepens the potential well, but does not provide radial pressure support. The figure also shows that $|\vec{u}_r|$ increases inward from $\vec{r} \approx 0.1$ pc.

The reversal of the power-law form of both $|\vec{u}_r|$ and \vec{v}_T as a function of radius tracks the position of \vec{r}_* , as can be seen comparing the lines for $t = -10$ kyrs in the left plot with $M = 1$ and $M = 4 M_\odot$ in the right plot. This confirms another aspect of the MC15 solution — that as \vec{r}_* moves outward with time the inflection point in $|\vec{u}_r|$ and \vec{v}_T moves outward as well, as we found earlier in §2.2.2.

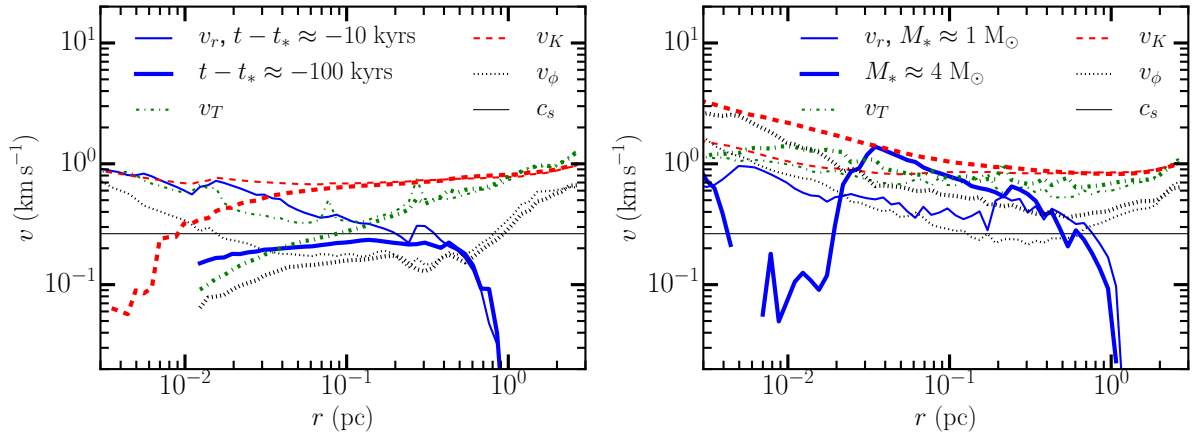


Figure 11 : $|\vec{u}_r|$, \vec{v}_T , \vec{v}_ϕ and \vec{v}_K as a function of \vec{r} at 10,000 (thin lines) and 100,000 (thick lines) years before the star particle forms (left plot) and when the star reaches 1 and $4 M_\odot$ (right plot). The averages are over the same regions as those used in producing Figure 9. The infall $|\vec{u}_r|$ and random \vec{v}_T velocities show the behavior predicted by the theory of adiabatic turbulent heating for times later than $-10,000$ years: at large radii, where $|\vec{u}_r|$ is small, $\vec{v}_T > |\vec{u}_r|$ and \vec{v}_T decreases inward, but more slowly than in non-collapsing regions; $p \approx 0.2$ rather than $p = 0.5$. Inside \vec{r}_* , where $|\vec{u}_r| > \vec{v}_T$ (or $|H| > \vec{v}_T$ in the notation of Robertson & Goldreich (2012)) \vec{v}_T increases towards $|\vec{u}_r|$ as \vec{r} decreases, with both increasing inward.

The steady outward march of the sphere of influence is demonstrated in Figure 12, which shows the run of enclosed mass at four different times. At $t = -100,000$ years, in Figure 9 the density cusp is not yet in place; correspondingly, at small radii the enclosed mass is convex, curving down as \mathbf{r} decreases. By $t = -10,000$ years cusp formation is complete, and a small disk has formed, evidenced by a slight upward concavity in the enclosed mass profile inside 0.02 pc. The radial extent of this upward concavity is increased to $\mathbf{r} \approx 0.1$ pc for $M_* = 1$, and further to $\mathbf{r} \approx 0.3$ pc by the time the stellar mass reaches $M_* = 4 M_\odot$. The position of \mathbf{r}_* can be inferred by the position in the curves where the concave portion of the curve meets the linear portion. The concave regions are dominated by a central mass and hence are inside of \mathbf{r}_* .

The growth of the central mass forces $\mathbf{r}_*(t)$ outward because $\rho(\vec{r})$ is independent of time, and hence the gas mass at small radii remains fixed, while $M_*(t)$ grows.

Returning to the velocities, the fact that $\mathbf{v}_T(\vec{r}) \sim \mathbf{r}^{0.48}$ for $t = -100$ kyrs in the left plot of Figure 11 shows that the turbulence in the initial collapse obeys the same scaling law found in non-collapsing regions in the molecular cloud (Lee et al. 2015). This

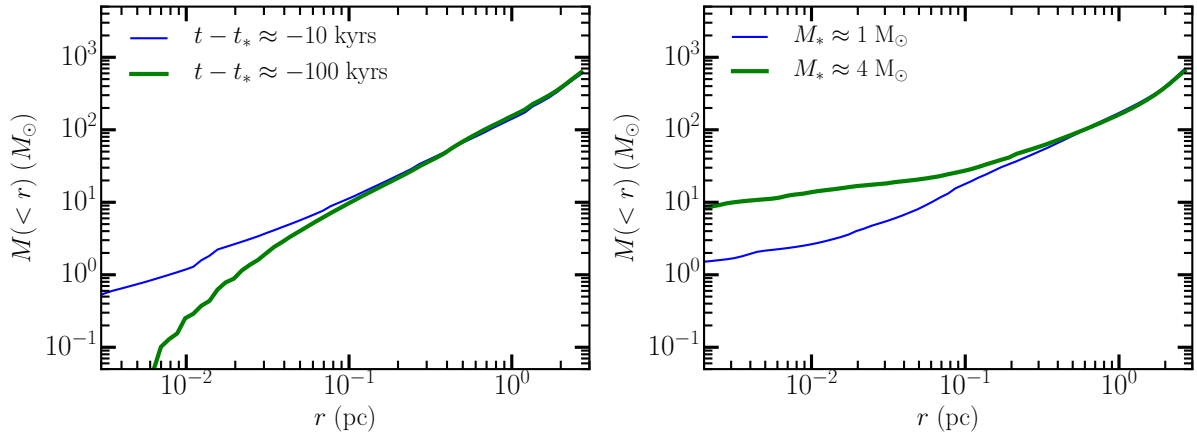


Figure 12 : Mass of gas and stars as a function of r at 10,000 (thin lines) and 100,000 (thick lines) years before the star particle forms (left plot), and when the star reaches 1 and 4 M_{\odot} (right plot). Averages are as described in Figure 9.

suggests that the turbulence in incipient collapsing regions is governed by the same large scale turbulent cascade as in non-collapse regions.

However, the flattening and reversal of $\mathbf{v}_{\text{T}}(\vec{r})$ at small radii and late times shows that some mechanism other than a turbulent cascade is at work at these radii and times. We interpret the behavior of $\mathbf{v}_{\text{T}}(\vec{r})$ as the combined result of compressional heating and turbulent decay, as suggested by MC15 and by Robertson & Goldreich (2012).

The relatively large infall velocity demonstrates that, even 100,000 years before the proto-disk or star particle forms, these regions are not in hydrostatic equilibrium, in which Reynolds stress or turbulent pressure balances the force of gravity. This calls into question the assumption made by previous analytic models of massive star formation, such as the turbulent core model. At early times, $|\vec{u}_{\text{r}}|$ is between $\vec{v}_{\text{K}}/3$ and \vec{v}_{K} , except at $\vec{r} \gtrsim 1$ pc, where the clump fades into the ambient molecular cloud. These high ratios of $|\vec{u}_{\text{r}}|/\vec{v}_{\text{K}}$ show that hydrostatic equilibrium is not a valid description of the star forming regions at any time.

In fact, these plots show that $|\vec{u}_{\text{r}}|$ is of order $\vec{v}_{\text{K}}/3$ or larger at all times for $\vec{r}_d \lesssim \vec{r} \lesssim 1$ pc.

At small radii, the fact that $\rho(\vec{r}, t) = \rho(\vec{r}) \sim \mathbf{r}^{-3/2}$ for $\vec{r} < \vec{r}_*$, combined with the fact that $|\vec{u}_{\text{r}}(\vec{r}, t)| \sim \mathbf{r}^{-1/2}$, ensures that $\dot{M}(\vec{r}, t) = \dot{M}(t)$, i.e., the mass accretion rate is

independent of radius for $\mathbf{r} < \mathbf{r}_*$.

This result for the accretion rate was shown previously in Figure 7. At early times, $(t - t_*) \sim -100$ Kyrs (the red dotted curve), \dot{M} decreases by a factor of 20 between $r = 0.5$ pc and $r = 0.01$ pc because the density profile is still evolving toward the attractor solution. But for later times $\dot{M}(\vec{r})$ is flat at small radii. This demonstrates that the attractor solution, once established, imposes a major effect on the accretion profile.

While the gas is never hydrostatic, the gradient of the Reynolds stress does roughly balance gravity as can be seen in Figure 13. The figure shows the rotational support, which we define as $\mathbf{v}_\phi^2/\mathbf{r}$ (solid blue line), Reynolds stress plus thermal pressure support $\rho^{-1}d\mathbf{P}/d\mathbf{r} = \rho^{-1}d\rho(\mathbf{v}_T^2/2 + c_s^2)/d\mathbf{r}$ (dashed line), and total pressure support $\rho^{-1}d\mathbf{P}/d\mathbf{r} + \mathbf{v}_\phi^2/r$ (thick red line). We have scaled these quantities to the local gravitational acceleration, $g = GM(< \mathbf{r})/\mathbf{r}^2$.

Inside of $\mathbf{r} \approx 0.01$ pc, the gas settles into a rotationally supported disk and the support from other sources drops. However, the sum of the Reynolds stress and rotational support (thick red line) nearly balances the local gravity.

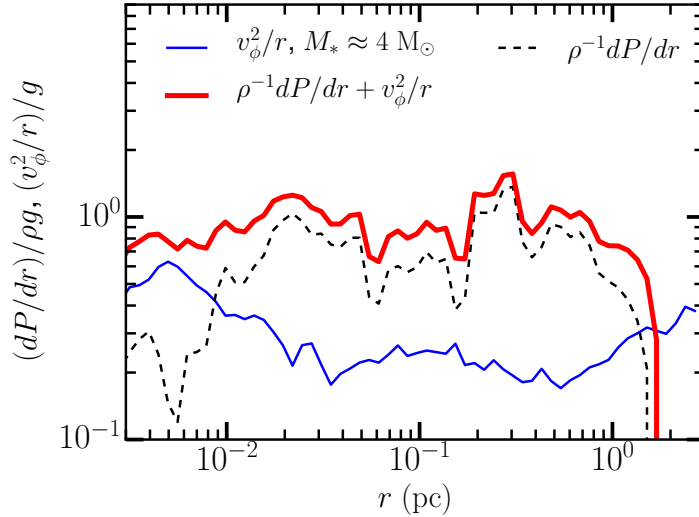


Figure 13 : The ratio of rotational (solid line) support, Reynolds stress and gas (dashed line) pressure support to the local gravitational acceleration $g = GM(< \mathbf{r})/\mathbf{r}^2$, as a function of \mathbf{r} when the star reaches $4M_\odot$.

The rotationally supported disks in our simulations are, on average, roughly marginally

stable, as seen in Figure 14, which should be compared with Fig. 3 in Kratter et al. (2010). For $0.007 \text{ pc} \lesssim r \lesssim 0.02 \text{ pc}$, we find $1 \lesssim Q \lesssim 1.6$. Examining individual disks, some of the time the disk is unstable and rapidly dumps material toward the central star, while at other times the disk is stable, building up material to approach marginal stability. For $r \gtrsim 0.02 \text{ pc}$, Q rises, though the interpretation of Q as a measure of stability is questionable, as the gas is no longer rotationally supported, nor is it in a flattened or disk-like configuration.

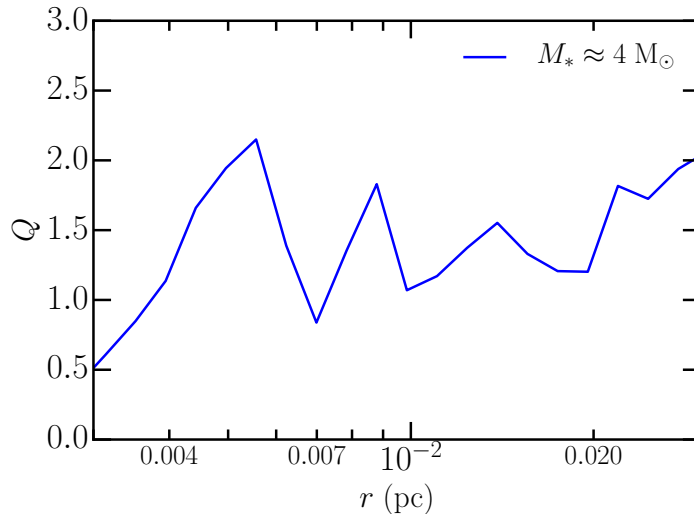


Figure 14 : The average (over many disks) of Toomre Q as a function of r when $M_* \approx 4 M_\odot$.

2.2.8 Mass Accretion Rates

Finally, we discuss the mass accretion rates in our simulation. Previously, Lee et al. (2015) (see also Myers et al. 2014) found that the star formation efficiency is nonlinear in time, with $M_* \propto t^2$. This nonlinear rate is evident in the work of previous workers, but was often interpreted as an initial transient (Padoan & Nordlund 2011). MC15 showed that $M_*(t) \sim t^2$ is a natural consequence of the density approaching an attractor solution and the scaling of the infall velocity with the Keplerian velocity at small radius, as we have clearly demonstrated in this work.

First we address the question of whether the $M_* \propto t^2$ phase is an initial “transient”.

Tackenberg et al. (2012) and Traficante et al. (2015) estimate the lifetimes of massive star-forming clumps found using the Apex telescope and the Herschel telescope, respectively. Tackenberg et al. (2012) identify clumps with column densities $\Sigma_g > 0.1 \text{ g cm}^{-2}$, masses up to $10^5 M_\odot$. Since they have a fairly complete catalog of such clumps, they can estimate the typical lifetime of a clump by comparing to the number of massive stars formed in the Milky Way every year. They find a mean clump lifetime of $6 \times 10^4 \text{ yr}$, and a clump free-fall time of $\approx 1.5 \times 10^5 \text{ yr}$; the clumps live 1 free-fall time.

Similarly, Traficante et al. (2015) identify clumps with sizes ranging from $0.1 - 1 \text{ pc}$, masses ranging up to $10^4 M_\odot$. They estimate an upper limit lifetime for the starless phase of 10^5 yr for clumps with $M > 500 M_\odot$, and a ratio of starless to total clumps (the rest of the clumps host protostars) of 39%. Thus the total lifetime of clumps in their mass range (above $500 M_\odot$) is $\sim 2 - 4 \times 10^5 \text{ yr}$. The clumps in their sample have $10^4 \text{ cm}^{-3} \lesssim n_{\text{H}} \lesssim 10^5 \text{ cm}^{-3}$, so free-fall times $1.6 \times 10^5 \text{ yr} \lesssim \tau_{\text{ff}} \lesssim 5 \times 10^5 \text{ yr}$. The clumps live $0.2 - 2.5$ free-fall times, similar to the estimate of Tackenberg et al. (2012).

Thus the lifetimes of massive star forming clumps, when measured in units of free-fall times, is similar to the lifetimes of GMCs, again measured in free-fall times, e.g., Blitz et al. (2007), who find that GMCs live 2-3 free-fall times.

Our simulations run for only a fraction of a free-fall time, but those of other workers have often run for two to three (Wang et al. 2010; Padoan & Nordlund 2011), or, in some cases, up to five free-fall times. The simulations are often halted when $\sim 10 - 30\%$ of the mass has been converted into stars, since that is a rough observational estimate of the maximum fraction of clump gas turned into stars, e.g., Lada & Lada (2003). In most cases this star formation efficiency is reached in one or two free-fall times, while the $M_*(t) \sim t^2$ behavior is still apparent from the plots. In the case of Federrath (2015), in the MHD run with stellar wind/jet feedback, the $M(t) \sim t^2$ behavior ceases after 4 free-fall times, when the star formation efficiency is about 15%. Since it is unlikely that star forming clumps live so long, the simulated star formation rate is probably too low.

We conclude that the time scale over which the t^2 scaling is seen in simulations is similar to the lifetimes of massive star forming regions, so that, while the behavior we

focus on may be of short duration, it is not “transient”.

In Figure 15 we show the total M_* as a function of time since the first star particle was formed, t_* . This is exactly the same analysis as Lee et al. (2015). However, because the simulations are distributed among the eight different octants, each with a different star formation time, we produce the total SFE history as follows. First, we analyze the simulations to find the earliest time at which a star particle formed, which we define as t_* . We then look at all of the octant simulations to find the earliest time at which a simulation ended or t_{end} , which defines the time over which all our simulations have data. Because each snapshot for each simulation is taken at different times, we define a number of times at fixed intervals between t_* and t_{end} and interpolate the total stellar masses for each simulation on those times. These masses are then summed to produced $M_*(t)$, which we plot in Figure 15

As shown in Figure 15, $M_*(t)$ grows roughly linearly for $\approx 100,000$ yrs after the first star particle is formed. However once the total stellar mass reaches about $M_* \gtrsim 10 M_\odot$, at a time $t - t_* \gtrsim 100$ kyrs, $M_* \propto t^2$. At this stage, $M_*/M_{\text{GMC}} \sim 0.001$. This agrees well with the results of Lee et al. (2015), who found $M_* \sim t^2$ for stellar masses between $M_*/M_{\text{GMC}} \approx 0.015$ and 0.3. Due to the computationally expensive nature of our much higher resolution simulations, even given the use of AMR, we are not able push our simulation to the same total M_*/M_{GMC} as Lee et al. (2015) were able to in their fixed grid, but much lower resolution, simulations. However, our simulations do show that their simulations were already at sufficiently high spatial resolution to recover the scaling relation.

The reason for this is not hard to find. Figure 9 shows that at $\mathbf{r} \approx 1$ pc the density has already settled onto its time-independent form, while Figure 11 shows that the infall velocity is scaling as $\mathbf{r}^{-1/2}$ for $\mathbf{r} \lesssim 0.3 - 0.7$ pc, with the smaller value corresponding to the time of star particle formation, and the larger value to times for which $M_* \approx 1 M_\odot$. As long as a simulation resolves this radius (which corresponds roughly to \vec{r}_*), it will recover the $M_* \sim t^2$ scaling.

The slower growth at earlier times is due to fact that, at the time of star formation,

the infall velocity is non-zero, despite there being no star to attract the gas; see Figure 11. In other words, the initial infall velocity is larger than $\sqrt{GM_*/r}$; it takes time before the Reynolds stress can slow the infall to the steady state value given by equation (1.7.3), and hence before the mass accretion rate settles onto the steady state value given by equation (1.7.4).

The same comments apply to the accretion rates of individual stars; individual stars start out accreting mass at a roughly constant rate. At later times, when they have substantial masses, the accretion rate grows linearly in time. This happens only with the most massive star particles in our simulation.

The total number of star particles also grows roughly linearly with time; the combination of this linear growth in number of stars, together with the roughly linear mass growth of most of the stars, produces the over all $M_* \sim t^2$ scaling we see for the simulation region as a whole. In regions where the summed accretion rate is highest, individual star particles are not able to accrete all the collapsing mass, leading to the formation of new star particles in the immediate vicinity. In other words, our simulations produce clustered star formation. This is similar to what has been found in other recent simulations (Lee et al. 2015; Gong & Ostriker 2015).

We interpret Equations (1.7.2-1.7.4) as a description of star cluster formation; the total mass of the cluster will grow as t^2 ; the most massive stars may spend a significant fraction of their accretion history growing as t^2 , but many of the less massive stars will not undergo such rapid growth in their accretion rate.

2.3 Discussion

2.3.1 Basic Results of this Work

We begin with a summary of our results.

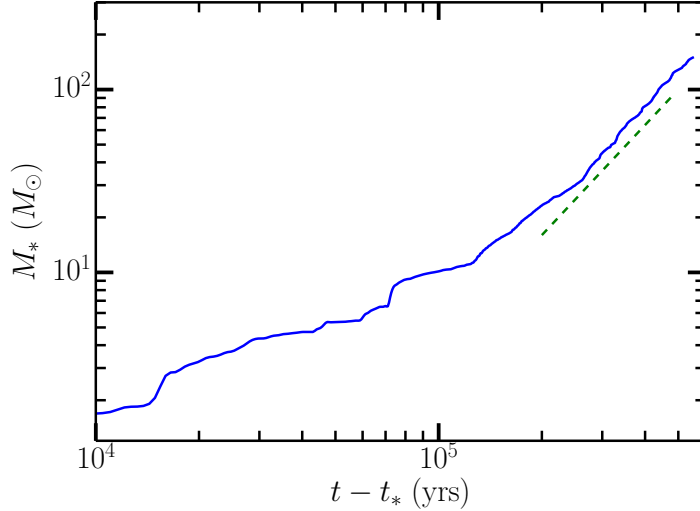


Figure 15 : The total mass in stars plotted as a function of time since the first star particle formed, t_* . The final value of the total stellar mass $M_* \approx 180M_\odot$ is about 1% of the total gas mass in the box, while the final $t - t_* \approx 0.6$ Myrs, about 15% of the free fall time 3.8 Myrs for the mean density of the box. The dashed green line shows a slope of 2.

Collapse is not self-similar

First, in our isothermal, driven turbulence simulations, star formation is not a self-similar process. Two length scales, in addition to the radius of the outer boundary condition or turbulence outer scale, and the stellar radius, enter the problem: The Keplerian or outer disk radius, \vec{r}_d , i.e., the radius at which the gas becomes rotationally supported, and the radius, \vec{r}_* , of the stellar sphere of influence, the smallest radius at which the gravity of the gas dominates the gravity from the star and disk. The existence and significance of \vec{r}_d has been known since the time of Kant and Laplace; the recognition that \vec{r}_* plays a role in star formation is recent, so we concentrate on the effect of \vec{r}_* on the dynamics in what follows. The value of \vec{r}_* increases monotonically with time, since the stellar mass increases monotonically, while \vec{r}_d may vary in or out with time, depending on the (turbulently determined) distribution of angular momentum of the accreting gas.

The non-self-similar behavior of the collapse is most strongly reflected in the variation of \vec{v}_T with radius; for $\vec{r}_d < \vec{r} < \vec{r}_*$, the random motion velocity is a decreasing function of radius $\mathbf{v}_T(\vec{r}) \sim \mathbf{r}^p$ with $p \approx -1/2$, while for $\mathbf{r}_* < \mathbf{r}$, it is an increasing function of \mathbf{r} ,

scaling like $\mathbf{r}^{0.2}$. Similarly, the infall velocity $|\vec{u}_r| \sim r^{-1/2}$ for $r_d < r < r_*$, while for $r_* < r$ it is flat or even increasing outward (as in the top panel of Figure 5), with substantial variations both from particle to particle and at different times for the same particle, due to the vagaries of the turbulent flow at large radii.

Density approaches an attractor solution

Second, we find that inside the sphere of influence of the star, the density remains constant over several to tens or even hundreds of (local) dynamical or infall times; for $r_d < r < r_*$, $\rho(\vec{r}, t) \rightarrow \rho(\vec{r})$. This is illustrated by Figures 6 and 9. One implication of this result is that one cannot use observations of the free-fall or crossing time of collapsing structures to infer either the age or lifetime of those structures.

The fact that $\rho(\vec{r}, t) = \rho(\vec{r}) \sim \mathbf{r}^{-3/2}$ for $r < r_*$, combined with the fact that $|\vec{u}_r(\vec{r}, t)| \sim \mathbf{r}^{-1/2}$, ensures that $\dot{M}(\vec{r}, t) = \dot{M}(t)$, i.e., the mass accretion rate is independent of radius for $r < r_*$ (see Figure 7).

Since $|\vec{u}_r|$ increases with stellar mass and hence with time where $r < r_*$ (see the second panel in Figure 11), while ρ is fixed, $\dot{M}(t)$ increases with time, a result seen in many previous papers (Padoan & Nordlund 2011; Bate 2012; Krumholz et al. 2012b; Federrath & Klessen 2012; Myers et al. 2014), although this fact was usually not commented on. After some initial transient behavior, we find $M(t) \sim t^2$ (Figure 15) in line with the results of Lee et al. (2015).

Partitioning of the Collapsing Region's Potential Energy

Our third result is to show how the potential energy released in collapse is partitioned. In our simulations, the support from random motions slows the rate of infall, so that $|\vec{u}_r|$ is significantly smaller than the free-fall velocity, but large enough to maintain \vec{v}_T at a sufficient level that the acceleration due to the Reynolds stress is close to the acceleration of gravity (Figure 13). In contrast, Sur et al. (2010) and Federrath et al. (2011) find an infall velocity which is equal to the free-fall velocity just outside their core. The dynamics in their simulation is very different to the dynamics in ours; in their case the

acceleration due to the pressure gradient is negligible compared to the acceleration due to gravity. Their initial conditions incorporate transonic turbulence, but no driving. Since the collapse in their simulation does not take place for roughly four free-fall times, by the time the collapse starts, the turbulence is subsonic.

Because the infall in our simulations is typically supersonic, some of the kinetic energy can then be converted into thermal energy by shocks; of course, even in the absence of shocks, normal (molecular) adiabatic heating will convert a small fraction of the liberated potential energy into heat.

Figures 3, 4, and 5 show that for $\mathbf{r} > \mathbf{r}_*$ the bulk of the potential energy goes into random motion, and thence into shocks. Inside \vec{r}_* , but outside of the disk, the potential energy that is not immediately radiated is shared roughly equally between the infall and random motions. Inside of the disk, the potential energy is converted to rotational and random motion, in roughly equal measure, and thence to thermal emission. At any radius, the ratio of kinetic energy to potential energy is typically around a quarter to a half, although at large radii ($\mathbf{r} \gtrsim 1 \text{ pc}$) the turbulent kinetic energy can exceed the potential energy: on the scale of our box, the ratio $\mathbf{v}_T / \sqrt{GM_{\text{GMC}}/r_{\text{GMC}}} \approx \alpha_{\text{vir}}^{1/2} \approx 1$, where M_{GMC} is the total mass contained in the simulation volume and $r_{\text{GMC}} = 8 \text{ pc}$ is the "radius" of the simulation volume, i.e., half of the side of the box. This ratio scales as $\sim 1/\sqrt{\mathbf{r}}$, so at $\mathbf{r} \approx 1 \text{ pc}$ the ratio is $\sim \sqrt{8}$.

We also found evidence that the ratio of radial to transverse random motion depends on whether the collapse leads to radial compression (for $\vec{r} > \vec{r}_*$) or dilation (for $\vec{r} < \vec{r}_*$), and on the tendency for hydrodynamic turbulence to isotropize motions down the cascade; see Figure 19 and the discussion in §2.5.4.

Modification of Larson's Law

Our fourth result is the confirmation that the adiabatic heating of the turbulence alters Larson's law. On large scales or away from collapsing regions, Larson's law is $\mathbf{v}_T \sim \mathbf{r}^p$ with $p \approx 0.4 - 0.5$. It emerges naturally from the decay of supersonic turbulence that is driven on large scales. We find, as did Lee et al. (2015), that in rapidly collapsing regions

the decay of $v_T \sim r^p$ with decreasing radius is slowed for $r_* < r \lesssim 1$ pc. Least squares fits to $\vec{v}_T(\vec{r})$ for over this range of radii result in exponents between $0.1 \lesssim p \lesssim 0.4$, with an average around $p \approx 0.2$, in fair agreement with the prediction of equation (1.7.3). Inside of \vec{r}_* , we find $p = -1/2$, as predicted by equation (1.7.3), representing a reversal of Larson's law.

Collapse does not proceed in an inside-out manner

A fifth result is that the gathering and accretion of mass starts from large scales, and that, both before and after a star particle forms, $\dot{M}(\vec{r}, t)$ is larger at large \vec{r} than it is at small \vec{r} ; in other words, the collapse proceeds in an outside-in manner. The first point, that the accretion starts from large scales, is illustrated by Figures 2, 3, and the left panel of 11, which show that $|\vec{u}_r(\vec{r})| \sim (1/3)\vec{v}_K(\vec{r})$ out to $\vec{r} \sim 1$ pc or farther, and is trans- or supersonic tens or hundreds of thousands of years before the density cusp forms, and hence before star or even disk formation starts².

Figure 7 shows that just after the cusp/star particle forms, the mass accretion rate is actually larger at larger radii. This behavior is the opposite of that predicted by inside-out collapse models, either that of Shu or of the turbulent core model. In Figure 7, this inside-out behavior is illustrated with a Shu-type solution, shown by the dashed line; in that solution, the mass accretion rate decreases with increasing radius, in contrast to the results of our simulation.

Figures 5 and 11 (right panel) show that just after and well after the star forms, the surrounding region is also far from hydrostatic equilibrium.

We conclude that there is no indication of gas in hydrostatic equilibrium prior to, during, or after star particle formation in our simulations. Nor is there any indication of inside-out collapse.

The violation of self-similarity and evidence against inside-out collapse shows that the assumptions made by previous analytic collapse models (Shu 1977; Myers & Fuller 1992;

²We remind the reader that the scale of the infall region in our simulations, and possibly in the ISM of galaxies, is a simply a fraction of the driving scale of the turbulence.

McLaughlin & Pudritz 1997; McKee & Tan 2003), are not fulfilled in our simulations. In addition, the collapsing regions in our simulations do not start from a hydrostatic equilibrium.

The magnitude of the pressure gradient term is comparable to that of the gravity term for $\vec{r} > \vec{r}_d$

Figure 13 shows that the acceleration due to the pressure gradient is comparable to the acceleration of gravity for $\vec{r}_d < \vec{r} < \vec{r}_*$. Thus Reynolds stresses slow the infall compared to the free-fall rate, i.e., $|\vec{u}_r(\vec{r}, t)| < \sqrt{GM(\vec{r})/\vec{r}}$. At small radii ($\vec{r} < \vec{r}_d$), the rotational support becomes important and the support from \vec{v}_T becomes much smaller than the radial component of gravity.

The total stellar mass increases as t^2

The total stellar mass in our simulation region, and in individual star forming sub-regions, increases as the square of time after the first star (in the box, or in the individual star forming region) forms. Low mass (less than a few solar masses) stars have $M_*(t) \sim t^\gamma$, with $0 \lesssim \gamma \lesssim 2$, with a typical value $\gamma \approx 1$, but the total number of low mass stars $N(t) \sim t$, so that the total mass in low mass stars grows as t^2 . High mass stars, which tend to sit at density peaks (or at the bottom of potential wells) have $M_*(t) \sim t^2$.

2.3.2 Comparisons to Observations

Caselli & Myers (1995) showed that massive star forming regions have shallower line width-size relations than the classical Larson result, i.e., $\vec{v}_T(\vec{r}) \sim \mathbf{r}^p$ with $p = 0.21 \pm 0.03$, compared to $p \approx 0.53 \pm 0.07$ in low mass star forming regions. Plume et al. (1997) also found that Larson's law breaks down in massive star forming regions, i.e., their measured line widths are larger for a given source size than those found in low mass star forming regions. As noted in §2.3.1, we find the same behavior in our simulations, and we interpret this as the effect of adiabatic heating in a collapsing flow at $\mathbf{r} > \mathbf{r}_*$.

In addition, Plume et al. (1997) plotted the mean velocity dispersion as a function of

number density, which they derived from an excitation analysis of CO. They found that, contrary to expectations, the velocity dispersion increased with increasing density, which is opposite to the expectation based on Larson’s law or supersonic turbulence driven from large scales. They concluded that the conditions in dense star forming cores are different from the rest of the cloud. The simulations presented here, and the analytic results of MC15, show the same behavior. In particular, the theory suggests that the enhanced turbulence or velocity dispersion at small radii in dense star forming regions is the result of gravitational collapse adiabatically heating the turbulence.

We find qualitative agreement between the observations of Plume et al. (1997) and our results, i.e., enhanced line-widths at high densities, which are associated with smaller radii. Performing a more detailed comparison is more difficult as we have selected regions with the same stellar mass, whereas the stellar mass in Plume et al. (1997) is not well known. However, it is promising that the linewidths in our simulations are of similar magnitude and show the same trend with density as do the observations.

There are now numerous measurements of infall at large radii $\sim 0.1 - 1$ pc in the literature. For example, Csengeri et al. (2011) Cygnus X, $D = 1.7$ kpc see infall $|\vec{u}_r| = 0.1 - 0.6$ km s $^{-1}$, $\sigma_T \sim 0.6 - 2$ km s $^{-1}$ at $\vec{r} \approx 0.1$ pc, $n \sim 10^5 - 10^6$. Other examples include Ragan et al. (2012, 2015) and Peretto et al. (2013).

Infall is also seen on larger scales, $\vec{r} \approx 1$ pc, by Wyrowski et al. (2016), who observe $|\vec{u}_r|$ in the range $0.3 - 3$ km s $^{-1}$, corresponding to a fraction of the free-fall velocity (1.4 the Keplerian velocity) of $0.03 - 0.3$. In words, the gas at $\vec{r} = 1$ pc is not in hydrostatic equilibrium, nor is it in free-fall. The turbulent velocity in the same clumps at the same radii is comparable or slightly in excess of the infall velocity, $\vec{v}_T \approx 1.0 - 2.3$ km s $^{-1}$.

Ho & Haschick (1986), Klaassen & Wilson (2008), and Klaassen et al. (2011) see infall at three different radii, $\vec{r} \approx 0.5$ pc, $\vec{r} \approx 0.3$ pc, and $\vec{r} \approx 0.03$ pc using different molecular tracers in the same object, G10.6-0.4. The infall velocity is large at large \vec{r} , small at $\vec{r} \approx 0.3$ pc, and large again at $\vec{r} \approx 0.03$ pc. As noted by MC15, this is in qualitative agreement with the picture of adiabatically heated turbulence.

2.4 Conclusions

Motivated by recent analytic (MC15) and numerical (Padoan et al. 2014; Lee et al. 2015) results, we perform deep AMR simulations of star formation in self-gravitating continuously driven hydrodynamic turbulence. We show that two length scales emerge from the process of star formation, \vec{r}_* and \vec{r}_d , and demonstrate that these length scales are clearly associated with physical effects. In particular, the character of the solution changes at $\vec{r}_*(t)$, inside of which (but outside \vec{r}_d) $|\vec{u}_r|$ and \vec{v}_T are both $\propto \mathbf{r}^{-1/2}$; outside of \vec{r}_* , $\vec{v}_T \sim \mathbf{r}^p$ (with $p \approx 0.2$), while $|\vec{u}_r|$ is on average about constant. We emphasize that the length scales at which the character of the solution changes are time dependent. As the star grows in mass, the radius where the stars' gravity exceeds the gravity of the surrounding gas increases outwards away from the star, $\vec{r}_*(t) \propto M_*^{2/3}(t)$. The disk radius, \vec{r}_d , also changes as a function of time as a result of the advection and transport of angular momentum from large scales to small scales (and vice versa).

We also found that the density profile evolves to a fixed attractor, $\rho(\vec{r}, t) \rightarrow \rho(\vec{r})$ in line with the results of MC15 and the earlier numerical results of Lee et al. (2015).

Our results strongly support the basic premise of MC15, that turbulence is a dynamic variable which is driven by adiabatic compression (Robertson & Goldreich 2012), and that the turbulence in turn acts to slow the collapse. We note, as did MC15, that observations of massive star forming regions also find $\mathbf{v}_T \propto \mathbf{r}^p$ with $p \sim 0.2 - 0.3$, and that at small radii or high density, \mathbf{v}_T increases with increasing density, as seen in observations of massive star forming regions (Plume et al. 1997). We find these departures from Larson's law only in collapsing regions in our simulations. We also show that the acceleration due to the pressure gradient is comparable to that due to gravity at all $\vec{r} > \vec{r}_d$. As a result, the infall velocity is substantially smaller than the free fall velocity even very close to the star or accretion disk. Inside \vec{r}_d , rotational support takes over and as a result $|\vec{u}_r|$ and \vec{v}_T both decrease.

Our simulations capture rotational dynamics that MC15 did not capture in their 1-D model. In particular, we find the development of rotationally support disks at $\vec{r}_d \sim 0.01$

pc. These disks have radii comparable to or slightly larger than disks seen around young stars in Taurus (Padgett et al. 1999) in which stellar feedback effects are minimal, and where the undisturbed disks are larger than in more active star forming regions such as Orion, where the disk radii are ~ 100 AU (Williams & Cieza 2011). This is despite the fact that we do not include magnetohydrodynamic effects in our numerical computations; large scale magnetic fields may transfer angular momentum away from these disks, shrinking them.

Like the disks modeled by Kratter et al. (2010), our simulated disks are marginally gravitationally stable, suggesting that large scale gravitational torques are responsible for transport of material and angular momentum in our simulations; this may also be true at early times in real protostellar disks.

We have shown that the assumptions made by previous analytic collapse models (Shu 1977; Myers & Fuller 1992; McLaughlin & Pudritz 1997; McKee & Tan 2003), are not fulfilled in our simulations. In particular, the collapsing regions in our simulations do not start from a hydrostatic equilibrium, nor do they show any evidence of inside-out collapse. The gathering of material before collapse, i.e., before the central cusp in the density power law is formed, involves transonic bulk motions and supersonic random motions (see Figure 11). The accretion of mass starts at large scales ($\vec{r} \sim 1$ pc) with large initial infall velocities. In addition, we find that \vec{v}_T scales differently in collapsing regions as opposed to the rest of the simulation box, whereas the turbulent collapse models (McLaughlin & Pudritz 1997; McKee & Tan 2003) assume that the scaling of \vec{v}_T with \vec{r} remains fixed.

Finally, we close this chapter with a brief discussion of how our results relate to turbulence regulated theories of star formation. Here we find several points of disagreement. First, we find that the star particles accrete continuously from the surrounding large scale turbulent flow; there is no hydrostatic “core” that is cut-off from the turbulent medium. Second, the density distribution does not remain log-normal, but rather develops a power law tail that is directly related to the density profile (Kritsuk et al. 2011; Lee et al. 2015). Third, the fact that the density profile approaches an attractor solution that scales like

$\mathbf{r}^{-3/2}$ for $\mathbf{r} < \mathbf{r}_*$ and \mathbf{u}_r scales with the Keplerian velocity guarantees that \dot{M} is constant with radius and $\dot{M}_* \propto t$ and hence a non-linear star formation efficiency, i.e., $M_* \propto t^2$ results. This is in contrast with turbulence regulated theories of star formation that predict a constant star formation rate, i.e., $\dot{M}_* = \text{const}$ and, hence, a linear star formation efficiency $M_* \propto t$.

2.5 Appendix

Prior to proceeding directly into the inclusion of protostellar jets, we wish to note several things.

2.5.1 Notes on Calculating the Random Motion and Rotational Velocity

In this section, we discuss how we calculate the random motion, v_T , infall, $|u_r|$, and rotational velocities, v_ϕ from the full three dimensional numerical solution. To begin, we adopt a series of concentric, logarithmically spaced, spherical shells around either a star particle (if available) or around a density maximum in the case where the star particle has not yet formed. We then removed the bulk velocity from these shells by first calculating the enclosed mass, $M(< r)$, and momentum in each sphere $\mathbf{P}(< r)$, then dividing the two to find the bulk velocity, $\mathbf{V} = \mathbf{P}(< r)/M(< r)$ of the sphere of matter. We then subtract this bulk velocity from the corresponding *shell*.

We also tried defining the bulk velocity using the total momentum in each of the spherical shells (rather than in the enclosed spheres), and found very similar results.

We then subtract the bulk velocity from the raw velocity of each cell in the spherical shell. We denote the result by \mathbf{v} .

Having removed the bulk velocity, we then calculate the radial infall velocity, $v_r = \mathbf{v} \cdot \hat{\mathbf{r}}$ per cell, where \mathbf{v} is the velocity of the gas in a cell and $\hat{\mathbf{r}}$ is the radial unit vector (with the origin at the location of the star or local density peak). Finally we find $u_r = \langle v_r \rangle$ as the average over the spherical shell, where

$$\langle v_r \rangle \equiv \Sigma_i m_i v_{r,i} / M_{\text{shell}} \quad (2.5.1)$$

denotes a mass weighted average over each spherical shell, and M_{shell} is the mass of the shell. The sum is over all the cells in the thin spherical shell.

To calculate the velocity in the ϕ direction, where ϕ is defined by taking the z axis along the angular momentum vector of the shell, we first calculate the angular momentum $\mathbf{L}_{\text{shell}} = \int_{\text{shell}} \mathbf{r} \times \mathbf{v} dm$, where m is the mass in a cell. We next calculate the moment of inertia tensor \mathbf{I} of each spherical shell. In component form, \mathbf{I} is

$$I_{ij} = \int_{\text{shell}} (\delta_{ij} r^2 - x_i x_j) dm \quad (2.5.2)$$

We then find the rotation vector $\boldsymbol{\Omega}$ by inverting

$$\mathbf{L} = \mathbf{I}\boldsymbol{\Omega}, \quad (2.5.3)$$

e.g., (McKee & Zweibel 1992). Next we calculate the rotational velocity in each cell from

$$\mathbf{v}_\phi = \boldsymbol{\Omega} \times \mathbf{r}. \quad (2.5.4)$$

This amounts to assuming that the gas in each spherical shell rotates rigidly; in other words we are averaging over the random motions in the shell. Finally, we calculate the spherical shell average as $v_\phi = \langle |\mathbf{v}_\phi| \rangle$, i.e., the mass weighted average of the norm of \mathbf{v}_ϕ .

Armed with the coherent infall (u_r) and rotational (v_ϕ) velocities, we define the remaining velocity as the random motion velocity (per cell) as

$$\mathbf{v}_T = \mathbf{v} - u_r \hat{\mathbf{r}} - \mathbf{v}_\phi \quad (2.5.5)$$

and the spherical average as $v_T = \langle |\mathbf{v}_T| \rangle$. As a check that we were accounting for all of the velocities, we added the velocities in quadrature: $v_{\text{sum}} = \sqrt{u_r^2 + v_T^2 + v_\phi^2}$ and verified that it traces the mass weighted average total velocity, $v_{\text{tot}} = \langle |\mathbf{v}| \rangle$ accurately.

2.5.2 Filamentary or Spherical Accretion?

Figures 2-5 show that the density in the vicinity of collapsing regions is decidedly non-spherical. Despite this, the results of MC15 appear to describe the accretion process well.

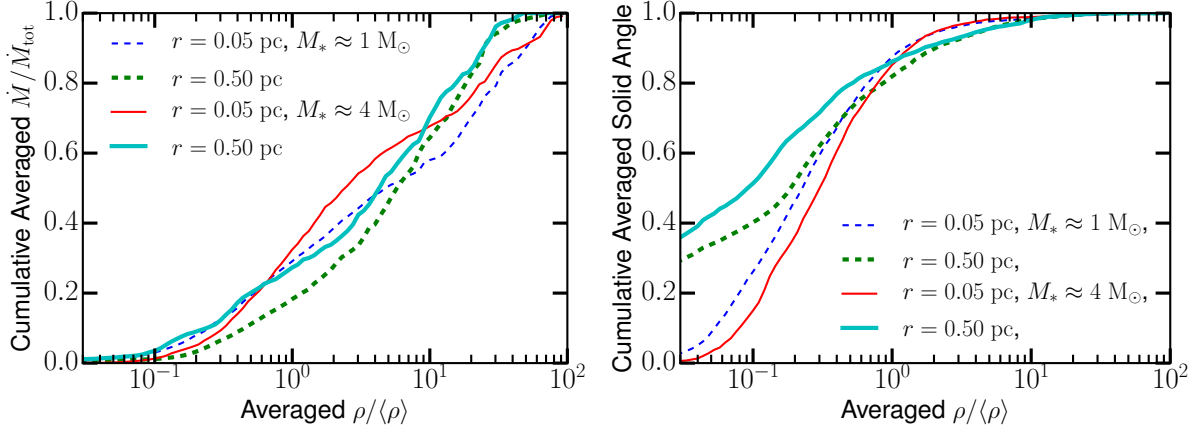


Figure 16 : Histogram of the cumulative normalized \dot{M} (left) and cumulative normalized solid angle (right) as a function of normalized density for $r = 0.05$ and 0.5 pc when the star reaches 1 and $4 M_\odot$.

For example, in those same Figures we have shown *mass-weighted* infall, random motion, and rotational velocities, the first two of which behave as predicted by MC15 (they made no predictions for v_ϕ).

To understand this better, we examine how \dot{M} depends on ρ , and how both are distributed on the sky as seen by the accreting particles. The left plot of Figure 16 shows a histogram of cumulative $\dot{M}(\rho)/\dot{M}_{tot}$ through two spherical shells at $r = 0.5$ pc and 0.05 pc, as a function of $\rho/\langle\rho\rangle$, where $\langle\rho\rangle$ denotes the density average over the (finite thickness) shell. We show average histograms when the central star has a mass $M_* = 1M_\odot$ (dashed lines) and $M_* = 4M_\odot$ (solid lines). The plot shows that 50% of the accretion through the sphere occurs via gas that has a density less than 2-5 times the average density of the shell, where the low end of this range occurs at small radii at late times, with the high end occurring at large radii and early times.

Since the mean density at $r = 0.5$ pc is $\langle\rho\rangle \approx 3 \times 10^{-21} \text{ g cm}^{-3}$, see Figure 6 or Figure 9, an examination of Figure 5, where gas with three times the mean density is depicted by dark green (and less dense gas is blue), shows that more than half of the accretion is coming from gas that covers most of the sky as seen from each of those accreting particles; most of each slice is colored blue. If we take filaments to consist of gas that is colored light green or yellow (with $\rho > 10^{-20}$, or ~ 3 times the mean density $\langle\rho\rangle$ inside $r = 0.5$ pc),

the filaments account for less than half the accretion.

A similar statement holds for the accretion inside $r = 0.05$ pc, shown as the thin lines in Figure 16.

To see more quantitatively how this gas is distributed on the sky, we plot in the right panel of Figure 16 the cumulative solid angle as a function of $\rho/\langle\rho\rangle$, again for $r = 0.5$ pc (thick lines) and for $r = 0.05$ pc (thin lines). Roughly 90% of the sky is covered by gas that is at three times the average shell density or lower, consistent with the qualitative analysis in the previous paragraph.

Figure 17 shows a histogram of the cumulative normalized \dot{M} as a function of the cumulative normalized solid angle. The plot shows that half the accretion occurs over about 10% of the sky where the density is ~ 3 or more times the mean density of the spherical shell. So, while about half the gas accretes from over most of the sky, and at about the mean density, very dense gas entering the sphere from a very small covering fraction of the sky contributes the other half of the total accretion budget.

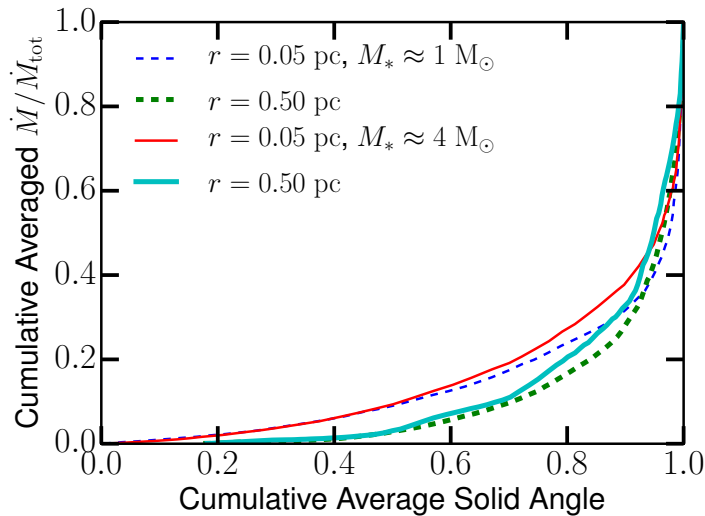


Figure 17 : Histogram of the cumulative normalized averaged \dot{M} as a function of the cumulative normalized averaged solid angle for $r = 0.05$ and 0.5 pc when the star reaches 1 and $4 M_{\odot}$.

Thus, while the filaments are readily identifiable by eye, and are important sources of accreting gas, much of the accretion (and much of the mass) lies in gas that is more nearly spherically distributed.

2.5.3 Star Formation Criteria

The majority of our simulations used a simple density condition of three times the Trulove condition (Equation 2.1.3) at the maximum refinement level inspired by the sink particle formation criteria of Padoan & Nordlund (2011) as discussed in §2.1. We have ex-

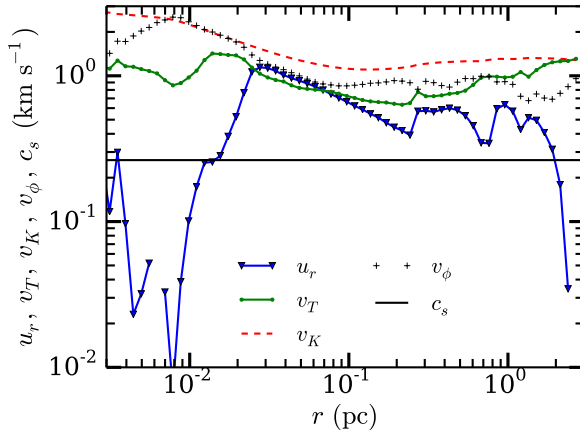


Figure 18 : The run of velocity for a particle formed in a simulation using FLASH’s built in particle formation checks (as well as the density condition proposed by Padoan & Nordlund (2011)). This shows that the dynamics of collapse are not overly sensitive to the star particle creation algorithm.

perimented with additionally including the sink particle checks of Federrath et al. (2010a) to check the robustness of our results to these additional checks. In Figure 18 we show the run of velocity in a simulation in which we included the star particle formation checks used in the default used in FLASH. The results do not differ significantly from runs lacking such checks. For example, both show that the stellar mass increases like $t - t_*$ squared, $M_*(t - t_*) \propto (t - t_*)^2$. There are however stochastic variations in the stellar mass ratio from runs with and without the extra checks. The mass ratio at a given $(t - t_*)$ can vary by a factor of roughly 2. For example, a hundred thousand years after the first star forms, in one run the total stellar mass is $10M_\odot$ while in another it is $15M_\odot$.

2.5.4 Radial and Lateral Components of the Random Motion Velocity

Figure 19 shows the radial $v_{T,r}$ and lateral $v_{T,l} \equiv (v_{T,\theta} + v_{T,\phi})/2$ ³ components of the random motion velocity for the same collapsing region as shown in Figure (5), where $v_{T,\theta}$ and $v_{T,\phi}$ are the random motion velocities along the $\hat{\theta}$ and $\hat{\phi}$ directions defined from the z-axis. In the absence of self-gravity, a turbulent hydrodynamic cascade to small scales tends towards equipartition, ($v_{T,r} \approx v_{T,l}$), with a scaling behavior $v_T \sim r^{1/2}$, similar to that seen in Larson’s size-linewidth relation; this is what we see in non-collapsing regions in our simulation.

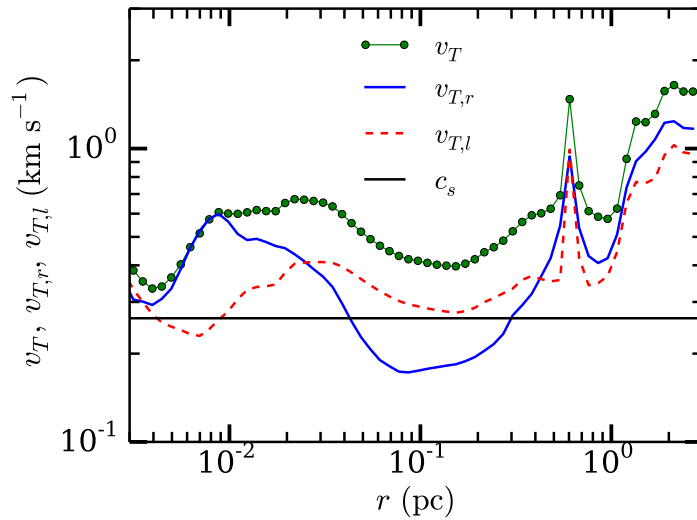


Figure 19 : The radial $v_{T,r}$ (blue solid), lateral $v_{T,l} = (v_{T,\theta} + v_{T,\phi})/2$ (red dashed) and total (green line over-plotted with dots) random motion velocities as a function of radius for particle B 100,000 yrs after the particle formed. The sound speed c_s is shown for comparison (black horizontal line). At large radii $v_{T,r} \approx v_{T,l}$; for $0.04 \text{ pc} \lesssim r \lesssim 0.4 \text{ pc}$ $v_{T,r} < v_{T,l}$, while inside of 0.03 pc $v_{T,r}$ quickly recovers and then exceeds $v_{T,l}$. The behavior of the lateral and radial velocities is dictated by the radial infall velocity in Figure 5 (see the main text).

Figure 19 shows that both the radial and transverse components of the random motion velocity decrease with decreasing r for $0.4 \lesssim r \lesssim 3 \text{ pc}$ (except for a spike at $r \approx 0.6 \text{ pc}$). Furthermore, the ratio $v_{T,r}/v_{T,l} \approx 1$. We interpret the decrease as the decay of turbulence down a cascade. However, the decrease in both the total and in the longitudinal component, when fit with a simple power law, gives $v_T \sim r^p$ with $p = 0.2$, while the

³Note that we define $v_{T,l}$ as an average so that we can compare it directly to $v_{T,r}$.

decrease in the radial component of the turbulence corresponds to $p \sim 0.35$. Since both exponents are less than the value $p \approx 0.5$ that we see on larger scales or away from collapsing regions, we conclude that adiabatic heating is affecting both the radial and transverse components of the turbulence.

At smaller radii, $0.04 \text{ pc} \lesssim r \lesssim 0.4 \text{ pc}$, the inward decrease of both $v_{T,r}$ and $v_{T,l}$ slows and then reverses, as the flow passes r_* . However, the ratio $v_{T,r}/v_{T,l}$ is now only $1/2$. Finally, at and inside the disk radius $r_d \approx 0.02 \text{ pc}$, the lateral turbulence once again decreases inward, while the radial component grows until much smaller radii, before decreasing again.

If adiabatic heating is responsible both for the slower than normal decrease with random motion velocity at $r > r_*$, and for the increase in random motion velocity inside r_* , why does the ratio of the radial and lateral components of the turbulence vary?

In Figure 5, $|u_r|$ is decreasing with decreasing radius over the range $0.4 \text{ pc} \lesssim r \lesssim 3 \text{ pc}$. What this decrease means physically is that as the gas falls in towards the center, it is being compressed not just in the θ and ϕ directions, but also radially. This compression along the radial direction should drive radial turbulence, while the lateral compression should drive lateral turbulence. This is why the radial and lateral components of the random motion velocity have the same magnitude.

This physical reasoning also tells us that as the infall velocity increases inward over the range $0.04 \text{ pc} \lesssim r \lesssim 0.4 \text{ pc}$ (see Figure 5), the gas dilates in the radial direction even as it continues to compress in the transverse (θ and ϕ) directions. Compression in the θ and ϕ directions will tend to drive an increase in the lateral components of the random motion velocity, but dilation in the radial direction will tend to drive a decrease in the radial component; of course both tendencies have to compete with (or add to, in the case of radial motion) the usual tendency for turbulence to decay, and the tendency, mentioned above, for hydrodynamic turbulence to tend to equipartition as the motion cascades to small scales.

We interpret the rapid inward decline of $v_{T,r}$ starting at $r \approx 0.4 \text{ pc}$ as the effect of adiabatic cooling. The result is that the ratio $v_{T,r}/v_{T,l} \approx 1/2$ for $0.04 \text{ pc} \lesssim r \lesssim 0.4 \text{ pc}$.

Between $r_d \approx 0.02$ pc and the local maximum of $|u_r|$ at $r \approx 0.04$ pc, the infall velocity is large but roughly constant, meaning that the radial dilation ceases. We interpret the up-tick in $v_{T,r}$ toward small radii as the result of the cascade of $v_{T,l}$ driving the radial component, as the turbulence strives to reach equipartition, combined with the cessation of adiabatic cooling associated with the cessation of radial dilation.

Inside $r \approx 0.02$ pc the infall takes place primarily through a rotationally supported disk, in which both the vertical $v_{T,\theta}$ and azimuthal $v_{T,\phi}$ component of the turbulence is greatly reduced (although we do not show the separate components in the figure). At the outer edge of this disk we see a sharp rise in the radial component of the random motion velocity, followed at yet smaller radii by a decrease in the total turbulent velocity. We interpret the drop in the total turbulent velocity at small radii as the flow settling into more ordered motion in an accretion disk.

2.5.5 The Initial Mass Function

For completeness we report the IMF in this subsection, though we caution the reader again that, because we do not handle the thermal physics properly, the location of the break in the IMF is unlikely to be correct; however it is commonly believed that the slope at the high mass end is set by the turbulence so that the thermal properties will not have much effect there. Figure 20 shows the IMF at the end of our Ramses run with $N_J = 32$. The plot includes a total of 90 stellar particles, with a total mass of $240M_\odot$, or about $\approx 1\%$ of the total mass in the simulation. The time that Figure 20 is plotted corresponds roughly to the right edge ($\approx 600,000$ years after the first star forms) in figure 21. It shows a form that is roughly consistent with observed IMFs, in that it has a power law at high masses, a peak around a solar mass, and a fall off at lower mass. The peak however, is at $2M_\odot$ which is about a factor of four higher than observed IMFs, and the fall off at high mass is too flat, indicating that we are top heavy. If the Salpeter slope is denoted by $\Gamma = 2.35$, our slope is $\Gamma = 1.36$.

Figure 21 shows the average stellar mass as a function of time. We see that the average mass is significantly higher than that of observed IMFs, where it is in the range

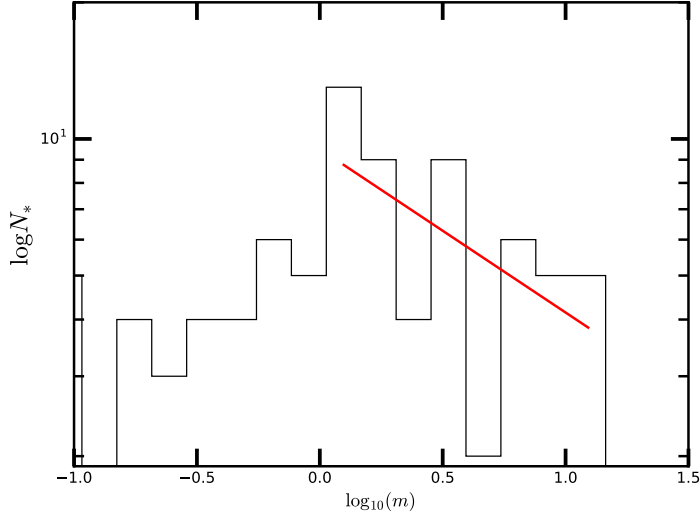


Figure 20 : Initial mass function for the Ramses run with $N_J = 32$. The peak of the IMF is at $2M_\odot$ and the high mass slope is $\Gamma = 1.36$, where the Salpeter slope is $\Gamma = 2.35$. The red line shows the least-squares fit to the mass function for $M \geq 1.0M_\odot$. Our IMF varies with time with the peak mass moving to lower mass and the value of Γ increasing with time.

of $0.3 - 1.0$. In addition, we see that this average mass rises initially as the massive stars grow and then decreases as low mass star formation kicks in.

2.5.6 Convergence with N_J

In this appendix, we examine how our results for the mass accretion rate depend on the resolution of the Jeans length, as quantified by N_J .

Figure 22 shows the total mass in stars plotted as a function of time since the time t_* at which the first star particle formed, for $N_J = 4, 8$, and 32 . For the $N_J = 32$ run, the final value of the total stellar mass $M_* \approx 240M_\odot$, for $N_J = 32$) is about 1% of the total gas mass in the box, while the final $t - t_* \approx 0.6$ Myrs, about 15% of the free fall time 3.8 Myrs for the mean density of the box. The green line shows the total stellar mass for $N_J = 8$, while the red line shows the same quantity for $N_J = 4$.

The figure shows that for $t - t_* > 200,000$ years the stellar mass as a function of $t - t_*$ is converged to within 10%, and to even better accuracy at late times.

We have also done a convergence study for the average mass, see figure 21, showing that the mean stellar mass is converged for $N_J = 4$. This is consistent with the IMF

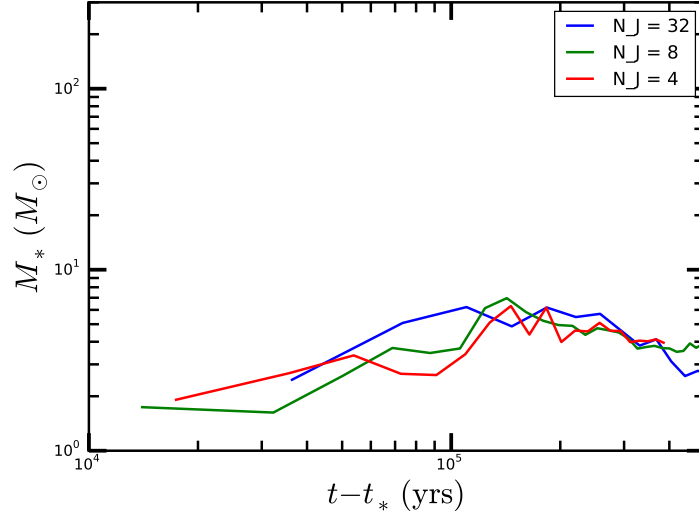


Figure 21 : Average stellar mass as a function of time for the Ramses run with $N_J = 32$ in green. Average stellar mass starts at $\approx 1M_\odot$ increasing to $\approx 6M_\odot$ and then decreasing as low mass star formation begins. We also show the average stellar mass for $N_J = 8$ (blue) and $N_J = 4$ (red). This demonstrates that $N_J = 4$ runs are converged.

being converged, albeit to a form that is not in good agreement with observations. We remind the reader that because of our use of an isothermal equation of state, we do not expect the IMF to match measured IMFs.

As a further convergence check, Figure 23 shows the run of density as a function of radius for three different Ramses simulations. The $N_J = 32$ (blue) run had 3 star particles at $0.5M_\odot < M_* < 3M_\odot$, while both the $N_J = 8$ (green line) run and the $N_J = 4$ (red line) had 9 star particles. We see convergence for all radii larger than the disk radius, r_d . This illustrates that the density approaches an attractor solution that is robust against the underlying numerical technique.

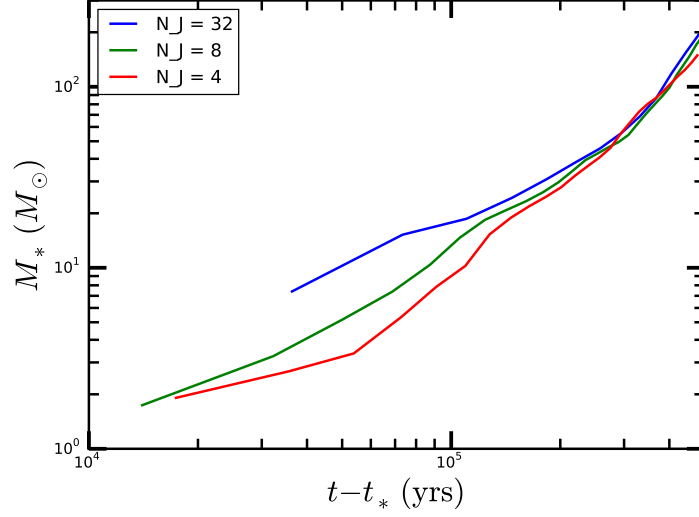


Figure 22 : Plot of $M_*(t - t_*)$ for Ramses runs with $N_J = 32$ (blue), $N_J = 8$ (green), $N_J = 4$ (red). At the end of the $N_J = 32$ run, the total stellar mass was $M_* \approx 240M_\odot$.

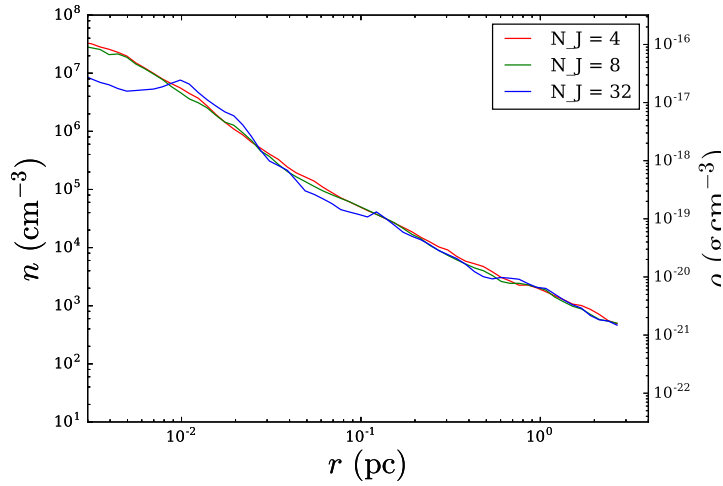


Figure 23 : Plot of $\rho(r)$ for Ramses runs with $N_J = 32$ (blue), $N_J = 8$ (green), $N_J = 4$ (red). These are the averaged profiles of the density for star particles with $0.5M_\odot \leq M_* \leq 3M_\odot$. Each simulation had $\approx 88M_\odot$ worth of gas in star particles. The density for $r > r_d$ is the same all three runs, showing that the $N_J = 4$ run is converged for $r > r_d$.

Chapter 3

The Effects of Protostellar Jet

Feedback on Turbulent Collapse

“I favored the dictaphone with a few fast comments, then got to work reprogramming the autopilot. Luckily what I wanted was simple. The X-force was but an X-force to me, but now I knew how it behaved. I might actually live through this.”

— Beowulf Shaeffer, *Neutron Star*
by Larry Niven

In the previous chapter, we found that the turbulence was driven at small scales by the collapse, and that it had a direct impact on the dynamics of star formation. Despite that, the star formation rate was rapidly approaching the free fall rate as the simulations proceeded; the turbulence merely delayed the inevitable.

Now we have to ask the question: Does the relation $M_*(t) \sim (t - t_*)^2$ hold when one of the physical processes ignored in the hydrodynamic simulations, in particular, feedback from protostellar jets, is included?

3.1 Current State of the Field

As a reminder to the reader, early work (Shu 1977; Myers & Fuller 1992; McLaughlin & Pudritz 1997) assumed that the pressure, which appears in the momentum equation, was

given by $P = \rho c_s^2$ with $c_s = \text{const}$ or $P = \rho v_T^2$ with $\mathbf{v}_T = \mathbf{v}_T(\vec{r}) \propto \mathbf{r}^{\kappa_r}$, i.e., a prescribed function of \mathbf{r} , and κ_r is typically chosen to be 1/2 to reflect Larson’s law (Larson 1981). In contrast, MC15 used the results of Robertson & Goldreich (2012) on compressible turbulence including both decay and compression, treating the turbulent velocity as a dynamical variable.

In any case, the issue of the slow rate of large scale star formation remains. One possibility is that stellar feedback acting on large (galactic disk) scales controls the rate of star formation on those scales. Cosmological simulations including both radiative and supernova feedback can reproduce Kennicutt’s observational results, e.g., Hopkins et al. (2011); Agertz et al. (2013); Hopkins et al. (2014). If these simulations are to be believed, the physics of stellar feedback from protostellar jets, which are not included, may not control the global galactic rate of star formation.

However, jets may control the rate of small (parsec) or medium (GMC) scale star formation and may power the observed turbulence in molecular clouds (Matzner 2007). As a result, a number of groups have recently studied the effects of protostellar jets and outflows on star formation (Wang et al. 2010; Myers et al. 2014; Federrath 2015). Nakamura & Li (2007, 2011) found that the effect of protostellar outflows was important for driving turbulence. Cunningham et al. (2011) and Hansen et al. (2012) found that protostellar outflows enhanced the effectiveness of radiative feedback. In addition, Federrath (2015) found that a combination of turbulence, jets, and magnetism is able to reproduce the observed low efficiency (to within a factor of four) of star formation in contrast to galactic scale simulations that rely on radiative and supernovae feedback.

The results of Lee et al. (2015), Murray & Chang (2015), and Murray et al. (2017) demonstrated that the small scale dynamics are intimately linked to the star formation rate. The question we address in this chapter is, do protostellar jets affect the small scale physics of accretion in a turbulent medium? In particular, does the stellar mass still increase as t^2 with the inclusion of protostellar jet feedback? The answer as we will argue below is no and yes, respectively.

The chapter is organized as follows. In § 3.2, we describe the numerical implementation

of the jet outflow (§ 3.2.1). In § 3.2.2 we describe our protostar evolutionary model, which is based on the one-zone models of Nakano et al. (2000) and Offner et al. (2009). We then present our results in § 3.3, describing the large (pc) scale jet effects (qualitatively) in § 3.3.1. In § 3.3.2 we show that the star formation rate is reduced by the ejection of mass in the jet, but the jets do not, surprisingly, significantly change accreting gas properties (in a spherically averaged sense) in § 3.3.3 - 3.3.5. We discuss the effects of the jet on the gas in terms of momentum depositions in § 3.3.6 and the driving of turbulence in § 3.3.7. We discuss our results in § 3.4 and give our conclusions in § 3.5.

3.2 Numerical Implementation

3.2.1 Jet Feedback Prescription

We have implemented a model of jet feedback in the adaptive mesh refinement (AMR) code, RAMSES (Teyssier 2002). Ramses is a mature AMR code that includes self-gravity, sink particle formation (Dubois et al. 2010; Bleuler & Teyssier 2014), and radiative transfer (Rosdahl et al. 2013; Rosdahl & Teyssier 2015). RAMSES has been used in a number of problems including cosmological structure formation (e.g., see for instance Ocvirk et al. 2016), star cluster formation (Gavagnin et al. 2017), colliding winds (Lamberts et al. 2011, 2017), and relativistic astrophysics (Lamberts et al. 2013; Lamberts & Daigne 2018). More recently, we have added a turbulent stirring module and have used this for star formation simulations in a turbulent gas without feedback (Murray et al. 2017).

Here we build on our previous work (Murray et al. 2017) by adding jets to the sink particle implementation in RAMSES (Dubois et al. 2010; Bleuler & Teyssier 2014). A jet is launched once a star particle has a mass in excess of $0.01M_{\odot}$ at which point it also has a well defined spin angular momentum. When the sink particle accretes gas from nearby cells, a fraction, f_{jet} , with a fiducial value $f_{\text{jet}} = 0.3$, of this gas is launched along the spin axis of the protostar. Numerically, this involves the injection of mass and momentum into nearby cells, while subtracting the ejected mass from the sink particle. The injection region consists of a bi-cone with an opening angle of 0.3 radians (≈ 17 degrees) about

the spin axis of the sink particle and a radial extent between 4 and 8 cells (at the highest refinement level) away from the sink particle. In particular, we set per cell in the injection regions:

$$\dot{\rho} = \sum_i^{n_{\text{sink}}} f_{\text{jet}} \mathcal{R}(r) \mathcal{T}(\theta), \quad (3.2.1)$$

$$\dot{\pi} = \sum_i^{n_{\text{sink}}} \dot{\rho}_i \mathbf{v}_{\text{jet}}, \quad (3.2.2)$$

where \mathcal{T} is the angular distribution, \mathcal{R} is the radial distribution, r is the radial distance of the cell center from the i th sink particle.

For the angular distribution, \mathcal{T} , we assume a Gaussian jet (in angle) about the spin axis of the sink particle:

$$\Theta(\theta) \propto \exp\left(-\frac{\theta^2}{\theta_0^2}\right) \approx \exp\left(\frac{1 - \cos\theta}{\cos\theta_0 - 1}\right), \quad (3.2.3)$$

where we choose $\theta_0 \ll 1$. In practice we use the approximation in equation (3.2.3) because $\cos\theta = \hat{\mathbf{l}}_{\text{sink}} \cdot \hat{\mathbf{r}}_{\text{sink}}$, where \mathbf{l}_{sink} is the angular momentum vector of the sink particle, and $\hat{\mathbf{r}}_{\text{sink}}$ is the direction from the i th sink particle to the cell in question, which simplifies the numerical implementation and computation, i.e., we avoid an \cos^{-1} computation.

For the radial distribution, \mathcal{R} , we set the deposition of mass and momentum to be constant between $r_{\text{jet,in}} = 4$ and $r_{\text{jet,out}} = 8$ grid cells from the sink particle. To ensure that this region is resolved, we force the region $r < r_{\text{jet,out}}$ around a sink particle to be refined to the maximum level.

To further ensure that the injection of mass and momentum per grid cell is as accurate as possible, we have integrated the injection of mass and momentum over the entire cell rather than evaluate the value at the cell center. This is necessary as the injection region depends on the grid cell size and is not necessarily a physical region. Here, we discretized the cell into n_{sg}^3 sub-cells, where n_{sg} is typically set to 3. This gives 27 evaluations of the mass and momentum injection per cell. The central value of the injected mass and momentum was taken for each of the sub-cells, and subsequently averaged to find the effective mass and momentum deposition over the entire cell. This algorithm was used because it gave more accuracy in the jet feedback implementation. Our method is similar

to the methodology in Cunningham et al. (2011) and Myers et al. (2014) to conserve mass and momentum where they compute the normalization of the jet kernel — effectively $\Theta(\theta)$ — numerically. Similarly, Federrath et al. (2014) iterates over the deposition of jet mass and momentum per star particle to conserve mass and momentum exactly.

We use the protostellar mass and radius to set the jet velocity. In particular, we set

$$v_{\text{jet}} = f_K \sqrt{\frac{GM_*}{r_{\text{p}*}}}, \quad (3.2.4)$$

where f_K is the fractional percentage of the Keplerian velocity the jet reaches asymptotically, and $r_{\text{p}*}$ is the radius of the accreting protostar. We take $f_K = 1/3$, following Myers et al. (2014). To set $r_{\text{p}*}$, we use two methods. First, following Federrath et al. (2014) we fix the protostellar radius at $r_{\text{p}*} = 10 R_\odot$. We use this only in the next section for our test problem. Second, we implement a one-zone protostellar model described by Offner et al. (2009, hereafter known as O09) and utilized in Myers et al. (2014). This latter model is used in our turbulent star formation simulations below.

Test Problem

To test the physics of the jet and our numerical implementation, we consider the following test problem. We simulate a periodic box with a length of 0.2 pc on each side and a fixed background density $\rho_0 = 3 \times 10^{-20} \text{ g cm}^{-3}$ ($n_0 = 10^4$ for H_2) of isothermal gas with a temperature of ≈ 17 K, which corresponds to a sound speed of 0.265 km s^{-1} . This setup is similar to the turbulent star formation simulations performed below and in Lee et al. (2015) and Murray et al. (2017), but with a larger density and a smaller box. In the center, we place a region of higher density, i.e., a clump, with a Gaussian density distribution, $\rho(\vec{r}) = \rho_m \exp(-\mathbf{r}^2/r_0^2)$, with maximum density of $\rho_m = 3 \times 10^{-16} \text{ g cm}^{-3}$ and a characteristic radius $r_0 = 0.017$ pc. The total mass of this dense region is approximately $M = 100 M_\odot$. The entire clump is set to solid body rotation about the z-axis with an angular frequency corresponding to 10% of the breakup velocity of the clump. The sink particle that forms also has a spin along the z-axis.

In Figure 24, we plot 4 snapshots of the collapsing clump. At $t = 0$ (upper left panel),

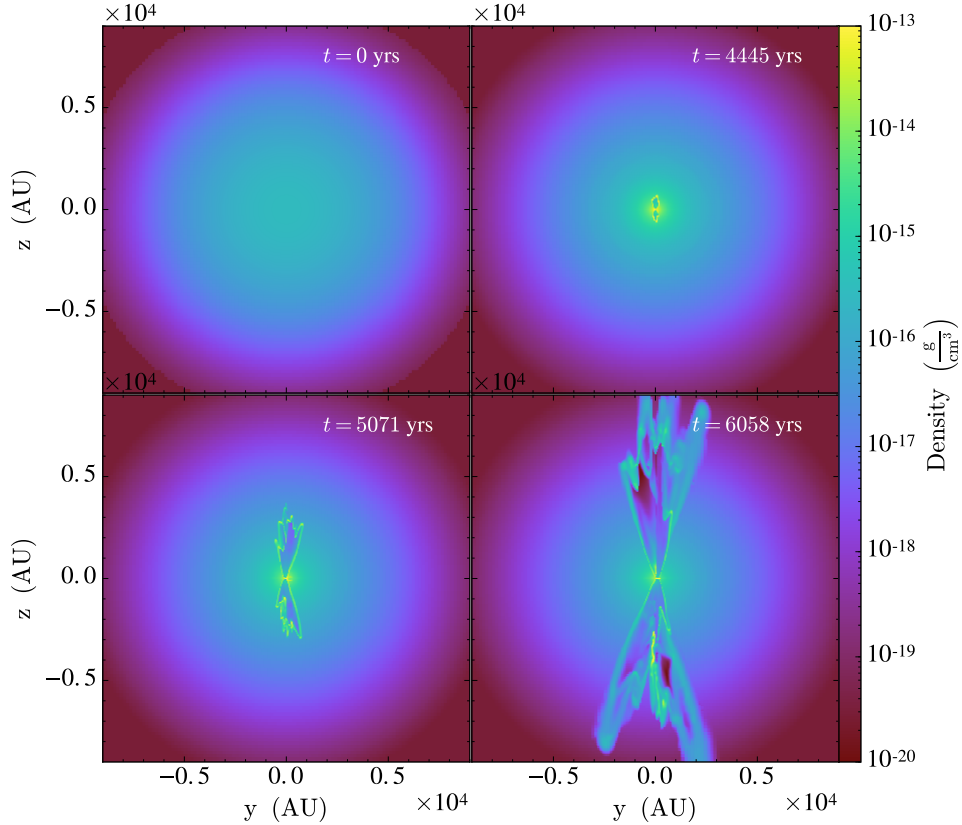


Figure 24 : Sequential plots of density structure perpendicular to the disk plane through the center of the sink particle. Columns from left to right show different times, from $t = 0$ to $t = 4820$ yrs, showing the effect of jet feedback on the test problem.

the simulation is initialized as described above. This clump begins to collapse, reaching a peak density of $10^{-13} \text{ g cm}^{-3}$ and forms a sink particle with its spin axis oriented along the z -axis at $t = 4445$ yrs (upper right panel). A jet develops and launches $f_{\text{jet}} = 1/3$ of the accreted mass along that axis. This jet grows and extends across the entire plotted region by $t = 6058$ yrs (lower left and right panels).

3.2.2 Protostar Evolution Prescription

In our jet model, the jet velocity is scaled to the Keplerian velocity at the surface of the protostar. Hence, both the mass and radius of the protostar is required. As discussed above, we can either fix the radius of the protostar as Federrath et al. (2014) have done

or implement a one-zone protostellar model (O09).

We now describe the latter case. Our treatment follows that of Myers et al. (2014) and O09. This 1-zone model, which is originally due to Nakano et al. (2000), describes the evolution of the radius of the protostar due to accretion, cooling, gravitational contraction, and nuclear burning.

Following the formation of a sink particle, we step through the following algorithm.

1. If the sink particle has M_* below $0.01M_\odot$ (the “pre-collapse” state) no jet is launched.
2. Once a star particle exceeds $0.01M_\odot$ it is assigned a radius and polytropic index based on the mass accretion rate (their equations (B1)-(B3) in O09). The deuterium mass is scaled to the mass of the sink particle times the cosmological abundance of deuterium. The protostar’s state is set to be “no burning,” because its core temperature is below that needed to burn deuterium.
3. We evolve the protostar in accordance to O09’s equation (B4), which is a discretized version of equation (8) of Nakano et al. (2000). We reproduce it here for convenience:

$$\begin{aligned} \Delta r_{\text{p}^*} = & 2 \frac{\Delta M_*}{M_*} \left(1 - \frac{1 - f_k}{\alpha_g \beta} + \frac{1}{2} \frac{d \log \beta}{d \log M_*} \right) r_{\text{p}^*} - 2 \frac{\Delta t}{\alpha_g \beta} \\ & \times \left(\frac{r_{\text{p}^*}}{GM_*^2} \right) (L_{\text{int}} + L_{\text{ion}} - L_D) r, \end{aligned} \quad (3.2.5)$$

where $\alpha_g = 3/(5 - n)$ describes the gravitational binding energy of a polytrope, and $\beta(n, M_*, r_{\text{p}^*})$ is the ratio of gas pressure to the total pressure for a polytrope of index n and (proto)stellar mass M_* and radius r_{p^*} as defined above. f_k is the fraction of kinetic energy of the infalling material that is radiated away (typically $f_k = 0.5$), L_{int} is the luminosity leaving the stellar interior, L_{ion} is the luminosity required to dissociate and ionize all infalling material, and L_D is the luminosity which is supplied by deuterium burning. We precompute β as a function of n , M_* , and r_{p^*} and linearly interpolate with that table for specific values. The luminosities, L_{int} , L_{ion} , and L_D are determined from equations (B6)-(B9) of O09 respectively.

4. Once the central temperature, reaches $T_c \geq 1.5 \times 10^6$ K, the protostar advances to a “core burning at fixed temperature” state. Following O09, we also reset $n = 1.5$. We

proceed to burn deuterium at a rate to maintain a fixed temperature in accordance with O09 (their equation (B8)).

5. Once the deuterium mass in the star drops to zero, the protostar switches to “core burning at variable core temperature”; deuterium is burned as rapidly as it is accreted (O09, their equation (B9)).
6. At this point the star can take two paths. If the radius of the star falls below r_{ms} , where r_{ms} is the radius of the main sequence star of the same mass (from Ezer & Cameron (1967),) we set $r_{\text{p*}} = r_{\text{ms}}$ and the state of the star is set to “main sequence”. However, if $L_D > 0.33L_{\text{ms}}$, where L_{ms} is the main sequence luminosity, we set the protostellar state to be “deuterium shell burning”, $n \rightarrow 3$, and the radius is expanded by a factor of 2.1 to mimic swelling due the formation of a radiative zone (O09). Subsequently the star then shrinks down to the main sequence.

This model provides a protostellar radius for each star particle, which we then use in equation (3.2.4) to determine the jet velocity. Though we wait until the initial mass of our protostar is $0.01M_{\odot}$, our choice for the threshold mass does not greatly alter the evolution of the system. As stated in equation (3.2.4): $v_{\text{jet}} \propto M_*^{1/2}$. The mass expelled by the jets is determined by: $m_{\text{jet}} = f_{\text{jet}}\delta M$, where δM is the total mass that would be accreted by the sink particle in the absence of jet feedback. It can be shown that $\dot{m}_{\text{jet}} \propto m^{1/2}$. The momentum of the jet is simply: $\vec{p}_{\text{jet}} = m_{\text{jet}} \times \vec{v}_{\text{jet}}$; thus, the time rate of change in momentum due to the mass is: $\dot{\vec{p}}_{\text{jet}} \approx \dot{m}_{\text{jet}} \times \vec{v}_{\text{jet}}$. Writing this expression solely as a function of mass: $\dot{p}_{\text{jet}} \propto m^{1/2} \times m^{1/2} = m_*$. Therefore the total integrated momentum: $\vec{p}_{\text{jet}} \approx \frac{2}{3}m^{3/2}$. So, if we do a comparison between the momentum of the jet from our threshold mass of 0.01 to 0.1 M_{\odot} vs 0.1 to 1.0 M_{\odot} , we see that changing our threshold mass from 0.01 M_{\odot} to 0.1 M_{\odot} affects our result by $\approx 0.1\%$.

3.3 Jet Feedback in Turbulent Star Formation

We use our protostellar star and jet model in RAMSES (Teyssier 2002) to model self-gravitating, hydrodynamic turbulence in isothermal gas with three-dimensional (3D),

periodic grids. We use eight levels of refinement on a root grid of 128^3 , giving an effective resolution of $32K^3$. We also performed runs at $8K^3$ and $16K^3$ to confirm convergence. We start with a box with the physical length set to $L = 16$ pc using periodic boundary conditions with an initial mass density of $\rho = 3 \times 10^{-22} \text{ g cm}^{-3}$ (number density $n \approx 100 \text{ cm}^{-3}$ for molecular hydrogen), corresponding to a mean free-fall time $\bar{\tau}_{\text{ff}} \approx 3.8 \text{ Myrs}$. This gives a total mass in the box $M \approx 18,000 M_{\odot}$. We fix the sound speed to be $c_s = 0.264 \text{ km s}^{-1}$, which for pure molecular hydrogen corresponds to an ambient temperature of $T \approx 17\text{K}$.

To initialize our simulations, we drive turbulence by applying a large scale ($1 \leq kL \leq 2$) fixed solenoidal acceleration field as a momentum source term. We apply this field in the absence of gravity and star particle formation for about 3 dynamical times until a statistical steady state is reached. At this point, the density is no longer uniform, instead it has a log-normal distribution.

After this statistical steady state is reached, we turn on self-gravity and star particle formation for our star formation experiments. We refine collapsing regions using a modified Truelove criterion, where $\lambda_J \leq N_J \Delta x$, where Δx is the cell length and N_J is the number of cells per Jeans length, λ_J (Truelove et al. 1997). This corresponds to a condition on the density

$$\frac{\rho}{\rho_0} = 11 \cdot 4^l \left(\frac{N_{\text{root}}}{128} \right)^2 \left(\frac{N_J}{8} \right)^{-2} \left(\frac{16 \text{ pc}}{L} \right)^2 \left(\frac{c_s}{0.265 \text{ km s}^{-1}} \right)^2 \times \left(\frac{3 \times 10^{-22} \text{ g cm}^{-3}}{\rho_0} \right) \quad (3.3.1)$$

where l is the refinement level, with $l = 0$ corresponding to the root grid. We use $N_J = 8$ to ensure that the Jeans length is resolved by at least 8 cells. When this density condition is met the local grid is refined by a factor of 2, provided that the maximum refinement level has not been reached.

When the Truelove criterion is exceeded by a factor of three at the highest refinement level, the excess mass is either accreted onto a nearby sink particle, used to create a new sink particle, or left alone. If the distance to the nearest sink particle is less than 2 grid cells, then the material is accreted onto that sink particle. On the other hand, if the gas

is contracting (local divergence of velocity is negative), a local potential minimum, and sufficiently far away from other sink particles, then the excess mass is used to produce a sink particle. Finally, if these additional checks are not satisfied, then the gas is left alone. We should note that this star formation criteria differs Chapter 2, which did not include these additional checks. We have found that jet feedback produces small pockets of high density as a result of shocks from the jet. This is why we have included these new checks in this work. To make a fair comparison between the feedback and no-feedback cases, we run the same numerical experiments both with and without jets.

Whether a star particle is newly formed from the collapsing gas or accreting the surrounding gas, it keeps track of its angular momentum. As a result each star particle is endowed with an angular momentum vector from which we can apply our jet feedback prescription. In addition, we have also modified each star particle to track its protostellar state which changes based on the conditions laid out above.

3.3.1 Parsec Scale Effects of the Jets

In Figure 25 we plot sequential projections of the entire simulation without (left column) and with (right column) jet feedback. We show the plots at $t = 0.8$ Myrs (top), which is right after the first stars form, to $t = 1.33$ Myrs (middle) and $t = 1.84$ Myrs (bottom). The images show up to seven levels of refinement, giving an effective resolution of 16384^3 or a minimum cell size of ~ 200 AU. The black dots in the $t = 1.33$ Myrs and 1.84 Myrs panels are representative of one or more sink particles. We state one or more, as the full box projections are zoomed out such that small clusters of two or three sinks have been plotted under one black dot. The black dots are also partly enlarged so that the reader may more readily compare our star formation sites between the jet and no jet simulations. We briefly note that we do not make a specific attempt to simulate either isolated or clustered star formation. Given our setup, we could expect to form moderate sized star clusters, of mass $\approx 2000M_{\odot}$, but this does not preclude isolated star formation.

Like previous simulations, e.g. Padoan et al. (1998); Lee et al. (2015), we see that the high density regions are organized into filaments, which appear to flow into large clumps.

The clumpy regions have the highest densities and as expected form sink particles first. The star formation efficiency (SFE) advances from $\epsilon_* \equiv M_*/M_{\text{tot}} = 0$ (right top) to 0.019 (right bottom) for the case with jet feedback, where M_* is the mass in stars and M_{tot} is the total gas mass; for the case without jet feedback, $\epsilon_* = 0$ (left top) to 0.06 (left bottom). The jet feedback case has substantially reduced SFE (by a factor of 3) and the gas shows evidence of driving by jets; note the bubble near $x = 1$ pc, $y = 5$ pc in the right column at 1.84 Myrs for example, which is not present in the left column.

Figure 26 displays a thin slice 1 pc on a side centered on a star particle, showing the bubble inflated by the jet from the central star. The total extent of the bubble, which has a bi-conical shape, is roughly a parsec.

Despite the fact that the morphology of the filament and the surrounding gas on parsec scales is dramatically affected by the protostellar jets, we show in the next subsection that the total stellar mass accretion rate in the box is not strongly affected by the large scale effects of the jets (although it is affected, at the factor of two or three level, by the direct removal of mass from the protostar/protostellar disk by jets).

3.3.2 Star Formation Rate

We begin with a discussion of the overall star formation efficiency (SFE). MC15 developed an analytic model of turbulent collapse, motivated by the work of Lee et al. (2015), who found that the SFE was $M_* \propto t^2$. The prediction for the SFR is:

$$\dot{M}_* = f 4\pi \mathbf{r}^2 \rho(\mathbf{r}) \sqrt{\frac{GM_*(\mathbf{r}, t)}{\mathbf{r}}}, \quad (3.3.2)$$

where $f = 1 - \Delta M_{\text{jet}}/\Delta M = 1 - f_{\text{jet}}$ is the fraction of mass that accretes onto the star particle. We have modified the expression in MC15 by including the factor f to account for the ejection of mass by the jet, the expression for \dot{M} can be written as $\dot{M} = f\beta M_*^{\frac{1}{2}}$, where β is a constant in time. We integrate from the star particles formation time to the current time to obtain:

$$M_*(t) = f^2 \left(\frac{\beta}{2}\right)^2 (t - t_*)^2. \quad (3.3.3)$$

In the analytic model the t^2 dependence arises from the following two results. First,

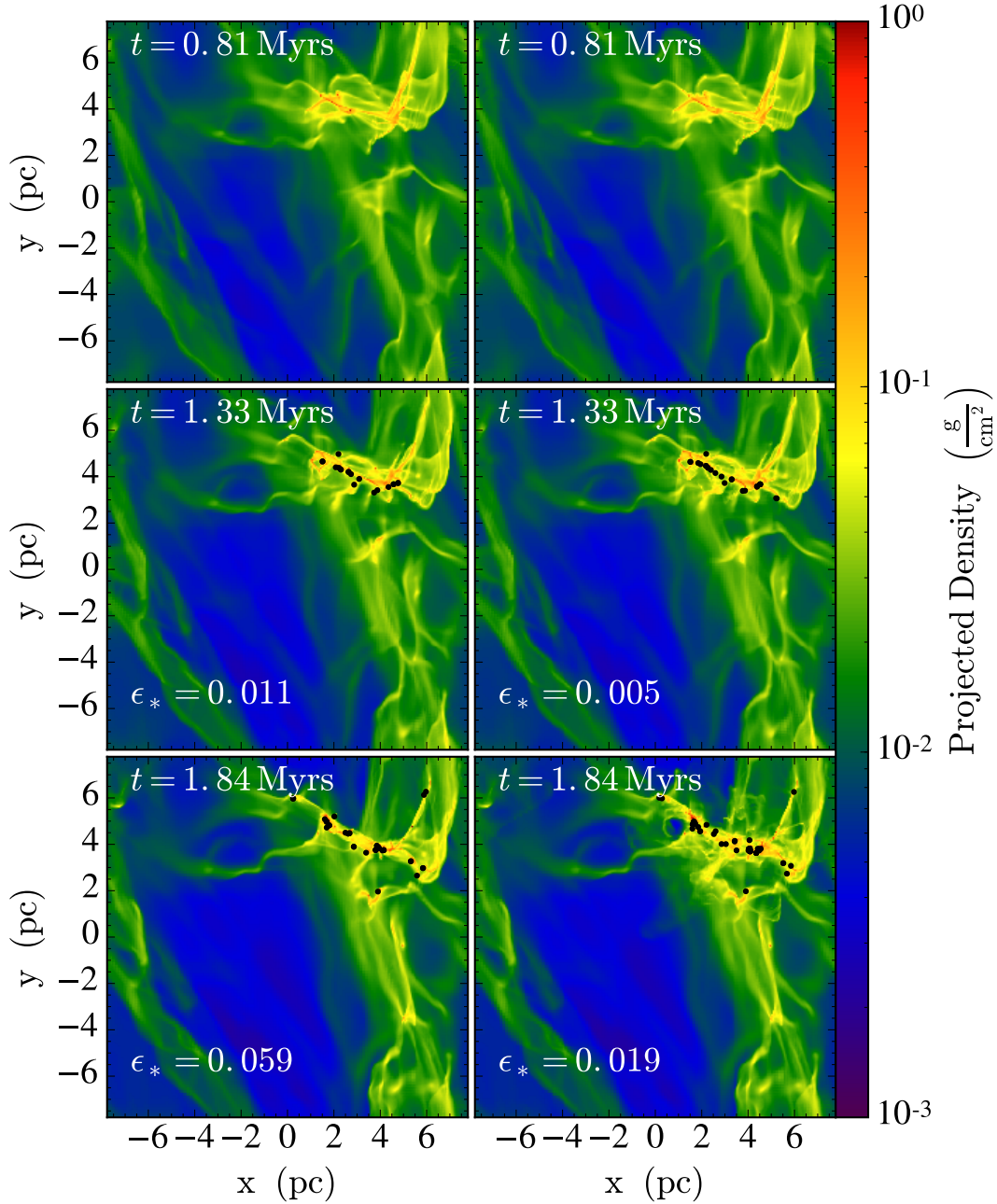


Figure 25 : Sequential projections of the density structure of the entire simulation domain along the z-axis for simulations with (right column) and without (left column) jet feedback. From top to bottom, we show the plots at $t = 0.8$ Myrs (top), which is right after the first stars form to $t = 1.33$ Myrs (middle) and $t = 1.84$ Myrs (bottom). The SFE advances from $\epsilon_* = 0$ (right top) to 0.019 (right bottom) for the case with jet feedback and from $\epsilon_* = 0$ (left top) to 0.06 (left bottom) in the case without jet feedback. The black dots represent locations where one or more sink particles have been created. We state one or more sink particles, as the full box projections are zoomed out such that small clusters of two or three sinks have been plotted under one black dot. In the bottom panels ($t = 1.84$ Myrs), the no jet feedback (left panel) simulation has a total of 46 sink particles accounting for $\approx 1072M_\odot$, while the jet feedback simulation (right panel) has 49 sinks for $\approx 342M_\odot$. Both jet and no jet simulations have a total box mass of $18,000M_\odot$.

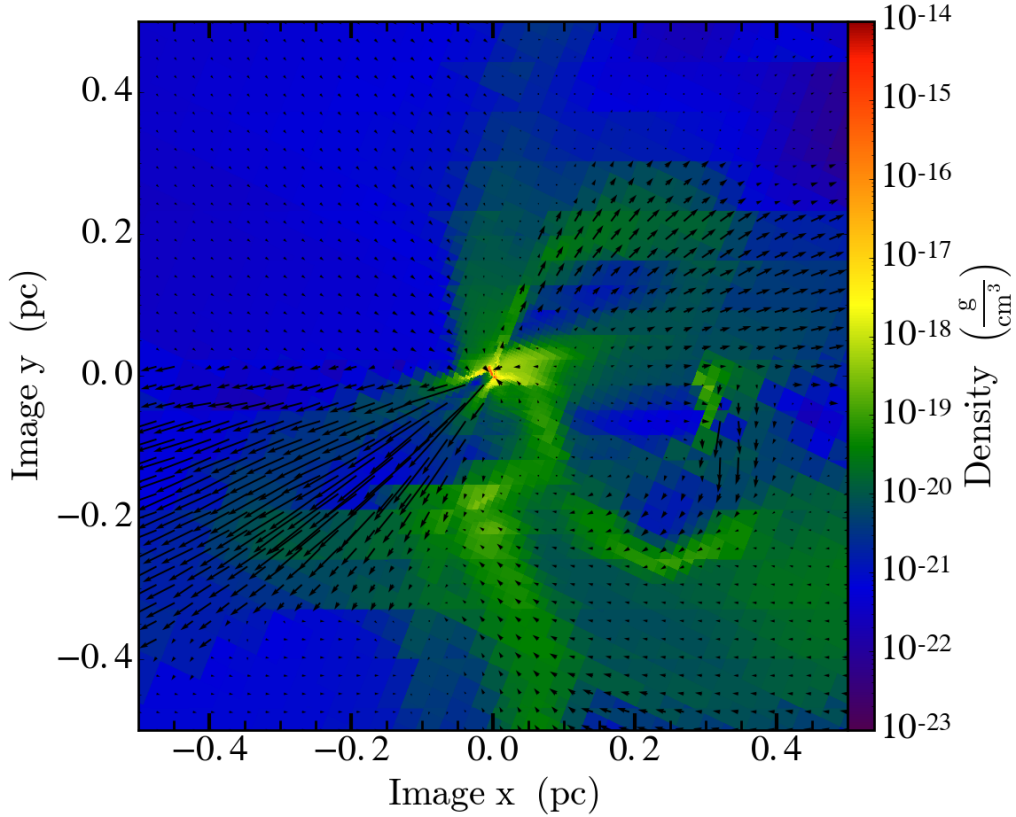


Figure 26 : A slice of the density structure centered on a sink particle of $\approx 3M_{\odot}$ viewed along the angular momentum axis. Annotated in black arrows is the gas velocity, where length corresponds to relative magnitude. The jet is blowing two bubbles opening in opposite directions, partially disrupting the filament in which the star particle formed. The maximum extent of the jet is ≈ 0.5 pc about 300,000 yrs after formation.

the density around a collapsing region approaches an attractor solution, $\rho(\vec{r}, t) \rightarrow \rho(\vec{r})$. Second, the velocities inside the “sphere of influence” \vec{r}_* , where \vec{r}_* is the radius at which the gas mass enclosed is roughly equal to the stellar mass, is controlled by gravity, i.e., $\vec{v}_r, \vec{v}_{\perp} \propto \sqrt{GM_*/r}$. Both the fact that the density approaches an attractor, and the growth of the infall velocity at a fixed radius with $M_*(t - t_*)$ were also later verified by Murray et al. (2017) using high resolution AMR simulations.

Does this story change in the presence of jet feedback? It appears that qualitatively it does not. In Figure 27 we show the SFE, $M_*(t - t_*)$, as a function of time since the first star particle was formed, t_* . We also report power law fits to the SFE (for $M_*/M_{\text{tot}} > 10^{-3}$),

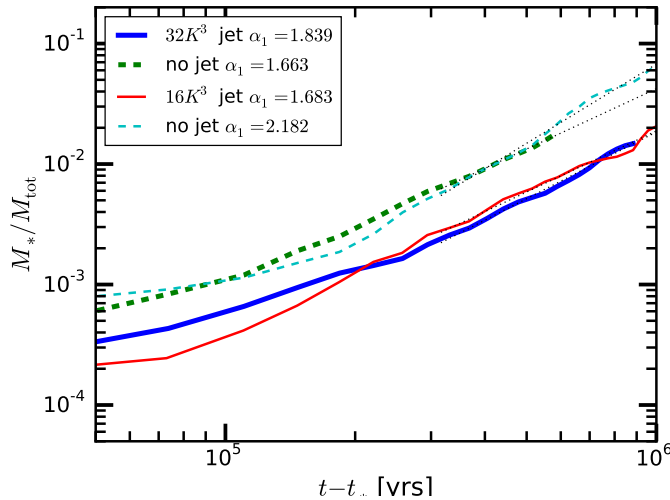


Figure 27 : Star formation efficiency (SFE) as a function of time since the formation of the first star, $t-t_*$. Power law fits to the SFE for $M_*/M_{\text{tot}} > 10^{-3}$ for an effective resolution of $32k^3$, $M_*/M_{\text{tot}} \propto (t-t_*)^\alpha$, give $\alpha \approx 1.8$ and ≈ 1.7 for the jet and no jet cases, respectively. We have done runs at $8k^3$, (not shown) for which the SFR does not appear to be converged. We note that the power law fits for both jet and no jet simulations are roughly equivalent. That is, the inclusion of protostellar jets does not affect the general dynamics of star formation. However, it is important to note that the case without protostellar jets has a larger percentage of mass in stars at any given time compared to the jet simulations. This indicates that while the inclusion of jets does not affect the power law of the accretion rate, it does reduce the mass accreted onto any given star particle at a fixed time after birth, by construction in our simulations, and by disk and/or X winds in real stars; see §3.3.2.

for both the $16k^3$ and $32k^3$ effective resolution runs. The fit gives $M_*/M_{\text{tot}} \propto (t-t_*)^\alpha$ with $\alpha \approx 1.8$ for both the jet and no jet cases. If the emergence of this t^2 law is due to the same physics as was shown in the no-jet case, then again the density approaches an attractor solution and velocity inside of the sphere of influence of the star particle is controlled by the stellar gravity. We demonstrate these two facts below in § 3.3.3 and 3.3.4, which show that the inclusion of protostellar jet feedback does not strongly affect the dynamics of star formation.

The normalization in Figure 27 shows that at a given time, the no jet case has approximately 2.5 times the mass of the jet case. Calculating the ratio of the stellar masses at a fixed time after star formation for the no jet vs jet runs, we find a ratio of 2.5 and 2.6 for the $16k^3$ and $32k^3$ resolutions. However, an examination of equation (3.3.3) reveals that the change in the normalization is explained almost entirely by the fact that the

jet case ejects $f_{jet} = 0.3$ of the mass accreted onto the star back into the interstellar medium in the form of a jet. In particular, equation (3.3.3) indicates that $M_* \propto f^2$, which implies that if the jet is ejecting a fraction $f_{jet} = 0.3$ of the accreted mass then the star's mass is only $f^2 = (1 - f_{jet})^2 = (0.7)^2 \approx 0.5$ of what its mass would be if there was no jet. MC15 and Murray et al. (2017) assumed $f_{jet} = 0 \rightarrow f = 1$, so it appears that the incorporation of jet feedback into the analytic theory of MC15 can be accomplished with a simple physical parameter!

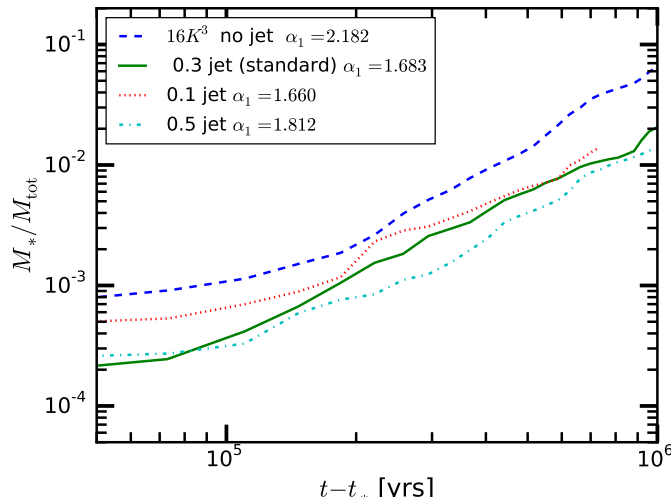


Figure 28 : Star formation efficiency (SFE) as a function of time since the formation of the first star, $t - t_*$ for 4 simulations, all with an effective resolution of $16k^3$. The jet simulations differ only in the fraction of accreted mass that they eject, the total momentum is the same across all jet simulations. The no jet (blue dashed) is the same simulation as the cyan dashed in Figure 27 and the 0.3 jet (solid green line) is the same as the thin solid red line in Figure 27. The dotted red line is $f_{jet} = 0.1$, while the cyan dot-dashed line is $f_{jet} = 0.5$. The effective resolution, jeans length and initial conditions are identical for all simulations in this plot.

Figure 28 plots the SFE for four different simulations, where we varied f_{jet} while keeping p_{jet} constant. The ratio predicted by equation (3.3.3) with $f = 0.7$ is 2.04 and accounts for 75% of the difference between the two runs. Thus the (indirect) effect of the jet on accretion onto star particle (from turbulent driving, expulsion of accreting gas, etc) is $\approx 25\%$, showing that the dynamical effect of jets on the mass accretion rate is minor. Comparing the left to right hand columns in Figure 25, this is not too surprising, since the differences are rather subtle; Figure 26 shows a zoom-in on a proto-star with a

jet-inflated bubble, which shows that, while the jet moves gas on scales of order a parsec, accretion continues along directions perpendicular to the jet axis.

In the next subsections we check the other predictions of MC15, $\rho(\vec{r}, t) \rightarrow \rho(\vec{r})$ is an attractor solution, $|\vec{u}_r| = \sqrt{GM_*/\vec{r}}$ is set by the protostar at $\vec{r} < \vec{r}_*$, and the “raw” mass accretion rate — without the f_{jet} correction — is the same in the cases with and without a jet.

3.3.3 A Fixed Point Attractor for $\rho(\vec{r}, t)$ Inside \vec{r}_*

One of the more striking findings in MC15 and confirmed in the simulations of Murray et al. (2017) was that the run of density is independent of time for $\vec{r} < \vec{r}_*$. Those simulations were hydrodynamic runs only, and thus the question addressed here is, do jets alter the density profile?

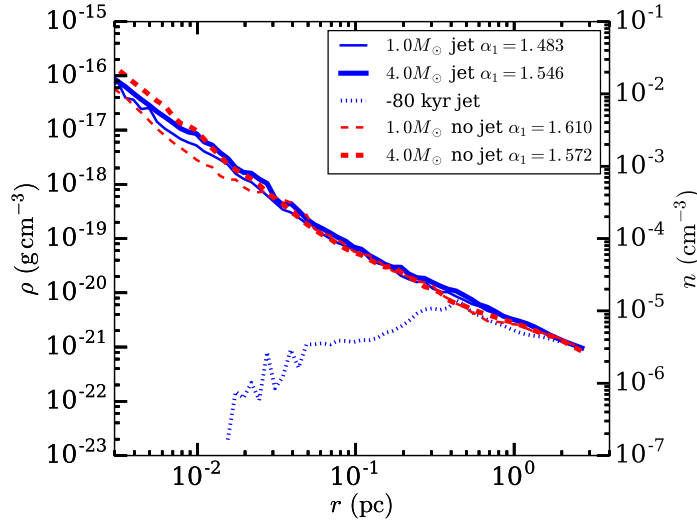


Figure 29 : Density ρ as a function of radius at 80,000 years prior to star formation (blue dotted line) and for 1 (thin lines) and $4M_{\odot}$ (thick lines) sink particles for both the jet (blue solid lines) and no jet (red dashed lines) simulations. In the jet case for the one solar mass stars we average over thirty six particles, and thirty particles for the four solar mass case. The corresponding no jet cases are averaged over nine and twenty three particles. Finally, the plot at 80,000 years prior to formation in the jet case is averaged over 16 particles.

In Figure 29 we plot the averaged number density n and mass density ρ as a function of \vec{r} for 1 and $4 M_{\odot}$ sink particles. The averages are over 36 and 30 particles respectively.

The plot confirms that $\rho(\vec{r}, t) \rightarrow \rho(\vec{r})$ for $\vec{r}_d < \vec{r} < \vec{r}_*$, i.e. the density is already on an attractor solution and that profile persists well after formation. We define the accretion disk radius \vec{r}_d as being the radius where the circular velocity (\vec{v}_ϕ) is larger than \vec{v}_T and $|\vec{u}_r|$. The mean power-law slope of the density after the star forms is $k_\rho \sim 1.5$. In addition the density profile is the same for the jet and no-jet case confirming a major ingredient of equation 3.3.3 showing that the results of MC15 continue to apply in the case of jet feedback.

It is important to note that the lack of change in the run of density is not due to the fact that we integrate for roughly a quarter of the global free-fall time. We emphasize that the density can change on the local free-fall time, which is much smaller than the global free-fall time. This can be seen from Figure 29, where $\rho(\vec{r})$ changes rapidly for $\vec{r} < 0.3\text{pc}$ before the star forms (see the dotted line).

3.3.4 The Infall ($|\vec{u}_r|$), Circular (\vec{v}_ϕ) and Random Motion (\vec{v}_T) Velocities with Protostellar Jets

Figure 30 shows the infall velocity $|\vec{u}_r|$ (blue triangles connected by a solid blue line), the random velocity \vec{v}_T (green dots connected by a green line), and the rotational velocity \vec{v}_ϕ (black plus signs) as a function of radius centered around a specific sink particle. The red dashed line depicts $\sqrt{GM(<\vec{r})/\vec{r}}$, while the black horizontal line shows the sound speed $c_s = 0.265 \text{ km s}^{-1}$. We calculate each of these velocities in the same manner as Chapter 2, with the following modification for the jet case: when calculating these otherwise spherical shell averaged quantities, we remove the cells that sit within the opening angle of the jet. See Appendix 3.6.1 to see how this subtraction affects the radial profiles of all the velocities.

The left panel in Figure 30 shows the velocities associated with a three solar mass sink particle in a simulation that included jet feedback. The right panel is of a sink particle in a simulation without jet feedback that formed within a hundredth of a parsec of the same location within a few thousand years of the same time as the particle in the jet case. That particle is roughly $3.8 M_\odot$. While we can not make a direct comparison of

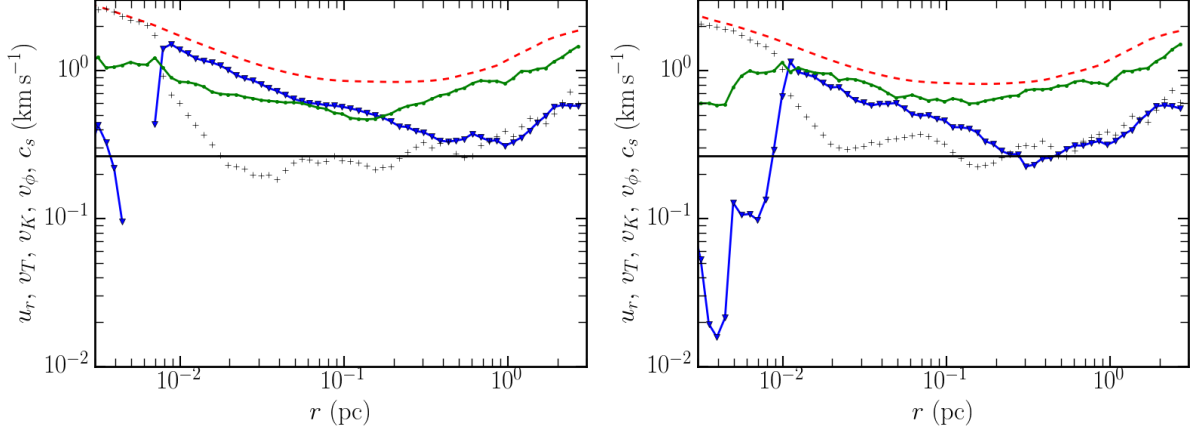


Figure 30 : The left panel is the run of velocity for a $\sim 3.0 M_{\odot}$ sink particle with jet feedback. The right panel is the particle in the same location in a simulation without jet feedback, with mass $3.8 M_{\odot}$. The sound speed is denoted by the black horizontal line while the infall velocity $|\vec{u}_r|$ is given by the blue triangles, connected by a solid blue line. The green circles connected by a solid green line show \vec{v}_T while the black crosses show the rotational velocity $\vec{v}_K \equiv \sqrt{GM(<\vec{r})/\vec{r}}$. Note that both $|\vec{u}_r|$ and \vec{v}_T increase with decreasing radius for $10^{-2} \text{ pc} < \vec{r} < 10^{-1} \text{ pc}$.

the magnitude of the velocities, due to the different masses, we can compare the trends in the velocities to the $\sqrt{GM(<\vec{r})/\vec{r}}$ velocity in each panel. We see similar behavior in both jet and no-jet simulations, with some expected differences.

First, what one immediately notices in each case (with and without jets), is that both $|\vec{u}_r|$ and \vec{v}_T decrease with decreasing radius down to $\vec{r} \approx 0.1 \text{ pc}$ then increase with decreasing radius, until running into the accretion disk around the sink particle, at $\vec{r}_d \approx 5 \times 10^{-3} \text{ pc}$. This indicates that jets by themselves do not change the general dynamics outside and inside the stellar sphere of influence. Both $|\vec{u}_r|$ and \vec{v}_T increase inward of \vec{r}_* . This was seen by Murray et al. (2017) for the no jet case. It is also consistent with the rapid increase in turbulent energy density with decreasing radius seen in Mocz et al. (2017), although their simulations halted when the first star particle formed (and hence did not include any protostellar jet feedback).

However, the inclusion of jets does affect the ratio of the random motion velocity to the fiducial velocity $\sqrt{GM(<\vec{r})/\vec{r}}$. In the case with jets, \vec{v}_T remains much closer to $\sqrt{GM(<\vec{r})/\vec{r}}$ for all radii larger than the disk radius as compared to that ratio for the no-jet simulation. This is not an unexpected result, given that jets are injecting momentum

back into the gas surrounding the collapse; this momentum deposition pumps up the random motions of the gas and thus slows down the in-falling gas. Even though the jets are boosting the random motion velocity, inside the stellar sphere of influence, $|\vec{u}_r|$ still increases with decreasing radius. That is, the gravity of the star dominates the dynamics.

Finally, we note that the infall velocity is $\sim 25 - 30\%$ of the free-fall velocity over all radii less than a parsec. This observation shows that this system is not in hydrostatic equilibrium. The run of density versus radius is similar to that in Figure 29.

3.3.5 Average Mass Accretion Rate $\langle \dot{M}(\vec{r}, t) \rangle_{\text{stars}}$ for Jet and No Jet Sink Particles

The final prediction that we can check is that $\dot{M}(\vec{r}, t)$ is independent of \vec{r} for $\vec{r} < \vec{r}_*$ and that the jet and no-jet cases have (roughly) the same \dot{M} . In Figure 31, we show the average mass accretion rate \dot{M} as a function of \vec{r} for 1 and 4 M_\odot sink particles comparing between the jet and no jet simulations.

We note that while the \dot{M} profile is flat at small radii it does increase over time: the profile at 4 M_\odot inside of \vec{r}_* is larger than that of the 1 M_\odot profile for both jet and no jet simulations. We contrast this with an inside-out collapse model, which we exemplify using a Shu (1977) solution, green dashed line obtained by directly integrating equations 11 and 12 of Shu (1977) at a fixed time.

We also note that both the jet and no-jet case settle onto an average \dot{M} that is roughly the same for the 1 and 4 M_\odot sink particle case. Hence the “raw” rate is the same in the jet and no-jet cases as implicitly required by equation (3.3.3).

3.3.6 Jet Momentum Deposition

In Figure 32 we plot the mass weighted average of the jet velocity for all sink particle jets over time. It has been calculated following the definition in Matzner & McKee (2000)

$$\langle \vec{v}_{\text{jet}} \rangle \equiv \vec{p}_{\text{jet}} / M_*, \quad (3.3.4)$$

where M_* is the total stellar mass and \vec{p}_{jet} is the total momentum ejected by all the jets up to the current time. Matzner & McKee (2000) estimate (observationally) that

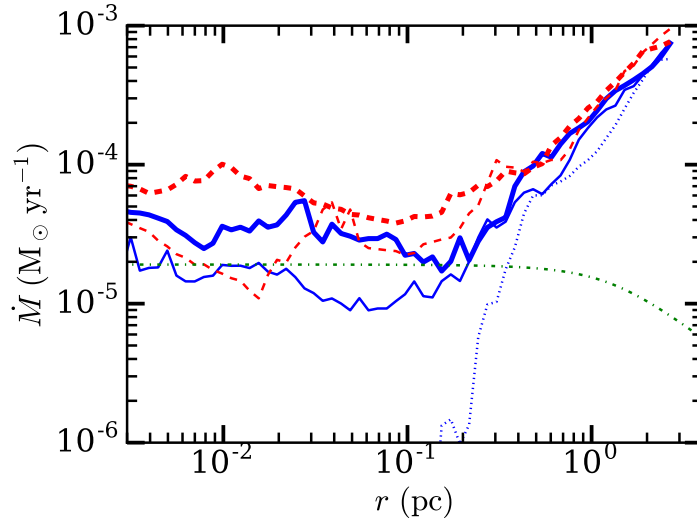


Figure 31 : The average run of \dot{M} for 1 and $4 M_\odot$ sink particles in simulations with and without jets. The blue solid lines are the jet simulations, while the red dashed lines are for the no jet case. The thin lines correspond to the $1 M_\odot$ averages, while the thick lines represent the $4 M_\odot$ averages. The thin blue dotted line is the average 80,000 years prior to formation in the jet case. The average, for the jet case, is over 16, 30 and 36 sink particles for the prior to formation, 1 and $4 M_\odot$ respectively. For the no jet case, the average is over 9 and 23 sink particles for the 1 and $4 M_\odot$ respectively. In all cases, the accretion rate is about an order of magnitude lower at small radii (say 10^{-2} pc) than at 1 pc. At both masses, and prior to formation, the accretion rate at 1 pc exceeds that at all smaller radii, showing that the collapse is outside-in, not inside-out. As an example of an inside-out collapse, we show the accretion rate for the Shu (1977) model (the green dot-dashed line) for a star of a solar mass with Shu's parameter $A = 3.501$.

$\langle \vec{v}_{\text{jet}} \rangle \approx 40 \text{ km s}^{-1}$. The figure shows that the average velocity is increasing with time because the stars are accreting more mass, and their radii are contracting. By the end of our run, the average velocity is in the range of that estimated by Matzner & McKee (2000).

We note that despite the relatively low value of the mass weighted average jet velocity over the entire box, the actual jet velocity is not necessarily slow. In Figure 33, we show the phase plot of density vs velocity for the no-jet case (left) and the jet case (right) at $t - t_* = 0.48 \text{ Myrs}$, which corresponds to the middle panels of Figure 25. The colourmap denotes the total mass of each point in density-velocity space. At the high density end, note that the velocities are substantially larger than the sound speed. This is due to infall stirring up v_T and $|u_r|$ as we saw in the velocity profiles above. A comparison between the no-jet and jet case on the high density end looks unsurprisingly similar. The jets are

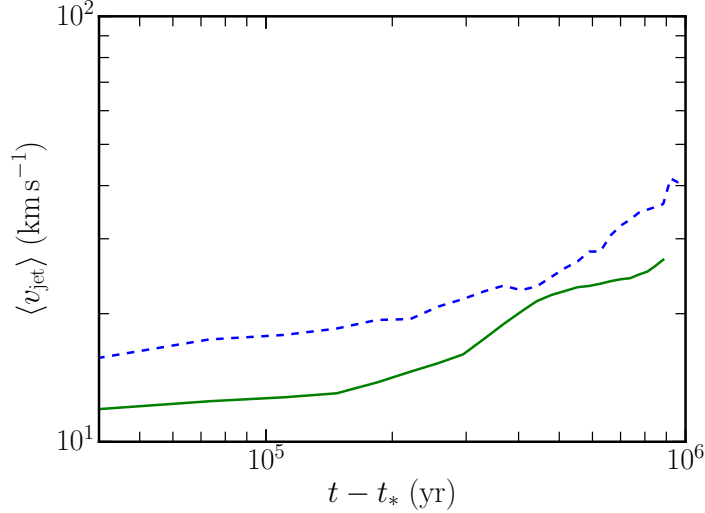


Figure 32 : The average jet momentum per stellar mass as defined in equation (3.3.4) as a function of time since the first sink particle forms ($t - t_*$). The solid green line depicts the $32k^3$ run while the dashed blue line depicts the $16k^3$ result. Both show an increase in $\langle \vec{v}_{\text{jet}} \rangle$ with increasing time. This occurs because as time increases, the star particles gain mass, and thus have higher escape velocities and launch faster jets. The $16k^3$ run produces higher jet momenta per stellar mass because it forms fewer stars that are more massive, due to its lower resolution. Note however that the total stellar mass in the two runs is converged (see Figure 27).

directed into lower density regions, not into the accretion disk and thus do not affect the high density regions.

However, we note that the major difference between the no-jet and jet cases is the substantial amount of gas above 10 km s^{-1} and that the density of this gas is around 10x the mean density $3 \times 10^{-22} \text{ g cm}^{-3}$. In fact, the jet case has material moving above 100 km s^{-1} .

3.3.7 Jets Mainly Drive Small Scale Turbulence

Figure 34 displays the mass averaged velocity dispersion in the simulation volume plotted as a function of time since gravity was turned on. The solid lines are the $32k^3$ simulation, while the dashed lines show the $16k^3$ simulation data. The thick and thin lines designate the jet vs no jet cases respectively. Looking at the no jet cases (at both resolutions), one sees an increase in the total velocity dispersion in the box from $3 \text{ km}^2 \text{ s}^{-2}$ to $4 \text{ km}^2 \text{ s}^{-2}$ by $t - t_* \approx 0.8 \text{ Myrs}$. This increase is being driven by the gravitational collapse as the first

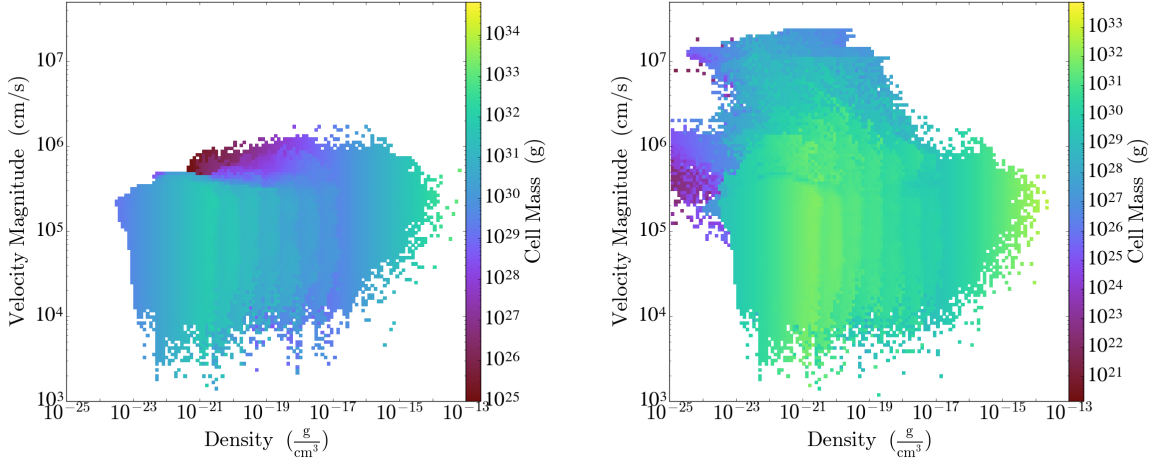


Figure 33 : Phase plot of density vs velocity for the no-jet case (left) and the jet case (right) at $t-t_* = 0.48$ Myrs. The colourmap denotes the total mass at each point in density-velocity space. The distribution at the high density end is set by gravity both accelerating the infall velocity and adiabatically heating the turbulent velocity, and is similar for both the no-jet and jet cases. There is, however, a clear difference between the no-jet and jet cases, namely, the substantial amount of gas above 10 km s^{-1} in the jet case. While there is a large distribution in velocity, this has only a 25% effect on the mass accretion rate (see Figure 27 and § 3.3.2).

stars begin to form. The jet cases' increase over this gravitational driving indicates that the jets do stir up the surrounding medium. It is important to note however, that this jet driving occurs on relatively small scales (of order $\sim 1 \text{ pc}$). This can be inferred by the rapid increase and decrease in the plotted velocity dispersions for the jet cases. In Figure 26 we presented a postage stamp shot of a star particle with $\approx 3 M_\odot$ that has cleared out a region on either side of the star particle nearly half a parsec in length.

The effect of jet driving in the velocity dispersion in the box can also be seen from looking at the power spectrum of the velocity. In Figure 35, we plot the velocity power spectrum for $t-t_* = -0.03$ (solid lines), 0.48 (dashed lines), and 1 Myrs (dotted lines) for the jet (thin black lines) and no-jet (thick blue lines) cases after mapping the simulation volumes to a 256^3 grid (to perform fast-Fourier transforms). These power spectrum correspond exactly to the top, middle, and bottom panels of Figure 25. As expected the $t-t_* = -0.03 \text{ Myrs}$ lines for the jet and no-jet case lines up exactly because they start from the same initial conditions. Moreover, the spectrum follows $P_k \propto k^{-2}$ as expected

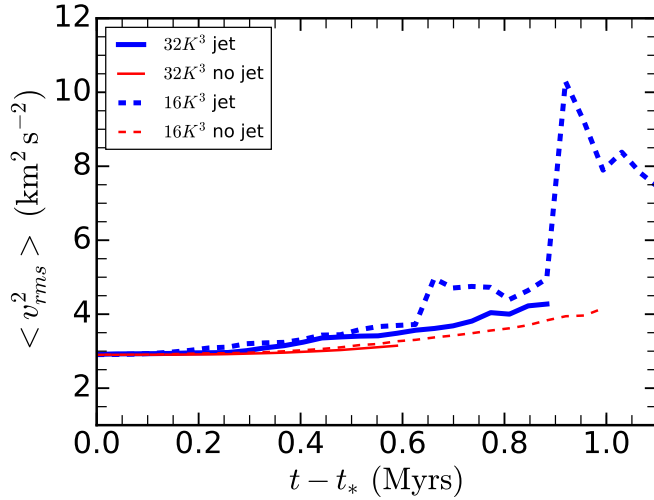


Figure 34 : The mass averaged velocity dispersion squared in the simulation volume plotted as a function of time since gravity was turned on. The thick and thin lines show the jet and no jet case respectively. The solid lines show the $32k^3$ result and the dashed lines the $16k^3$ result. The increase seen in the no jet case starting at $t \approx 1$ Myrs results from the gravitational collapse driving random motions. The excess seen over this background in the thick lines is the result of the jets driving random motions. Both the sharp increase and the sharp decrease in the latter case alert us to the fact that this driving occurs on relatively small scales (of order 1 pc): see Figure 26.

for Burgers turbulence up to where it begins to be cutoff around $k \approx 10L^{-1}$. For the no-jet case (thick blue lines), the power spectrum does not substantially differ in time as stars form. This is due to the fact that the timescale that we are looking at is smaller than the crossing time of the box. However, the jet case shows substantial deviation. At $t - t_* = 0.48$ Myrs for the jet case (thin black dashed line), we note that the power spectrum is remarkably similar to $P_k \propto k^{-2}$ even beyond the cutoff. In this case, this is not due to Burgers turbulence, but rather to the presence of delta-functions (at the resolution of 256^3) in velocity in the simulation volume. This is undoubtedly due to the narrow (on the scale of 256^3) protostellar jets. We caution the reader against the implication that this small scale velocity structure translates to turbulence in the star forming clumps. Figure 35 implies that the velocity structure is small scale, but does not imply that this structure is associated with the star forming regions. In particular, jets might induce turbulence at their working surfaces which would be at a significant distance from their launching sites.

At $t - t_* = 1$ Myrs, the jet case (thin black dotted line) show even greater deviation. Here the velocity power spectrum is larger than it was initially. On the larger scales, it has increase by a factor of approximately 3 and again remains remarkable flat for the same reasons discussed above. However, at $kL \sim 8$, we note a bump in the power spectrum, which contains the bulk of the energy. The scale of this bump is at $\sim L/8 = 2$ pc and so shows that the effect of jets is mainly on the few parsec scales in our simulation. Moreover, the decline toward larger scales from this scale may be an indication of an inverse cascade.

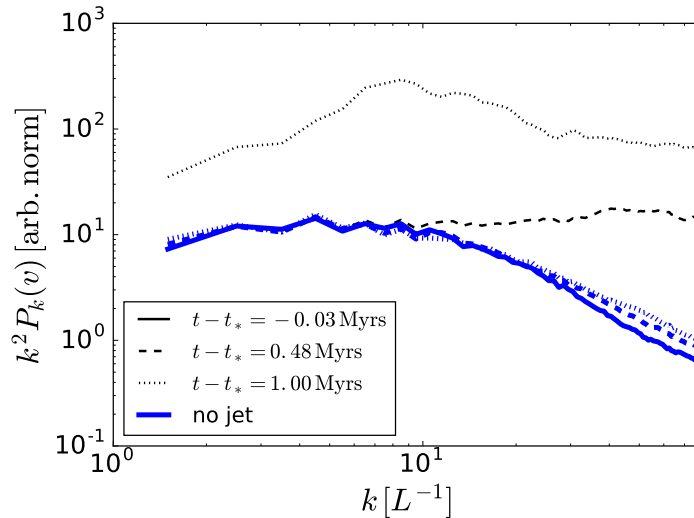


Figure 35 : Compensated velocity power spectrum, $k^2 P_k(v)$ as a function of wave vector, k at $t - t_* = -0.03$ (solid lines), 0.48 (dashed lines), and 1 Myrs (dotted lines) for the jet (thin lines) and no-jet (thick lines) cases. To perform the fast-Fourier transform, we map the simulation volume to a 256^3 grid. The $t - t_* = -0.03$ Myrs lines for the jet and no-jet case is the same as the spectrum is derived from stirred turbulence. The no-jet power spectrum does not substantially differ in time as stars form, but the jet case does. In particular the flatness of the power spectrum at large k at $t - t_* = 0.48$ and 1 Myr is due to the presence of velocity delta-functions (at the resolution of 256^3) in the simulation volume. Additionally, the jet drives an up-tick in power at $kL \sim 8$, a spatial scale of 2 pc, at $t - t_* = 1$ Myr.

3.4 Discussion

Given our initial set up of a box with sides 16 pc in length, with a Mach number of ≈ 9 and a virial parameter of order unity, we could expect to form moderate sized star clusters. However, this does not preclude isolated star formation. What we see is $\approx 180M_\odot$ in

stars, in a filament/clump ≈ 4 pc in length and a clump gas mass of $\approx 3500M_{\odot}$. The overdense regions that we see correspond to molecular clumps with a few thousand solar masses formed inside of our parent molecular cloud.

We have shown that protostellar jets do not strongly affect the dynamics of accreting gas. For example, the infall and rotational velocities both show similar behavior between the no jet and jet runs; the random velocity is also similar, once the region containing the jet cone has been excised (see Figure 37 and appendix 3.6.1). Similarly, the run of density approaches an attractor solution regardless of whether or not there are jets associated with the sink particle.

The fact that $|\vec{u}_r|$ increases inward for $\vec{r} < \vec{r}_*$, while increasing outward for $\vec{r} > \vec{r}_*$, combined with the time-independence of the density profile (once a density peak forms) implies that the mass accretion rate $\dot{M}(\vec{r}, t)$ for individual stars is flat for $\vec{r} < \vec{r}_*$ and increasing with radius for $\vec{r} > \vec{r}_*$. This is demonstrated in Figure 31, which also shows the contrasting behavior for an inside-out collapse model, that of Shu (1977). This is the signature of outside-in collapse, which occurs in runs both with and without jet feedback.

We have seen that jets do create cavities in the surrounding gas, changing the morphology of the gas on parsec scales. However, as we discussed in §3.3.7, while the jets and the expanding bubbles they inflate do drive turbulence, the outflows and bubbles do not have a large effect on the mass accretion rate. The jets do reduce the mass accretion rate, by a factor of about 2.5 in our simulations, but the bulk of this reduction is simply due to the jet ejecting mass from the star particle. In our simple jet model, this includes mass that in reality would be ejected from the associated protostellar disk.

We showed that the jet driven turbulence is on small scales (1 pc) compared to the scale of our simulation box (16 pc) or compared to GMC sizes (tens of parsecs). This ensures that the jet driven turbulence from an individual star decays more rapidly (see Figure 34 and 35) than the eddy turnover time of the simulation box, or of the host GMC in a real galaxy.

We have shown that $M_*(t) \propto (t - t_*)^2$ both with and without protostellar jet feedback, but that the stellar mass accreted after a given time is smaller by about a factor of 2.5

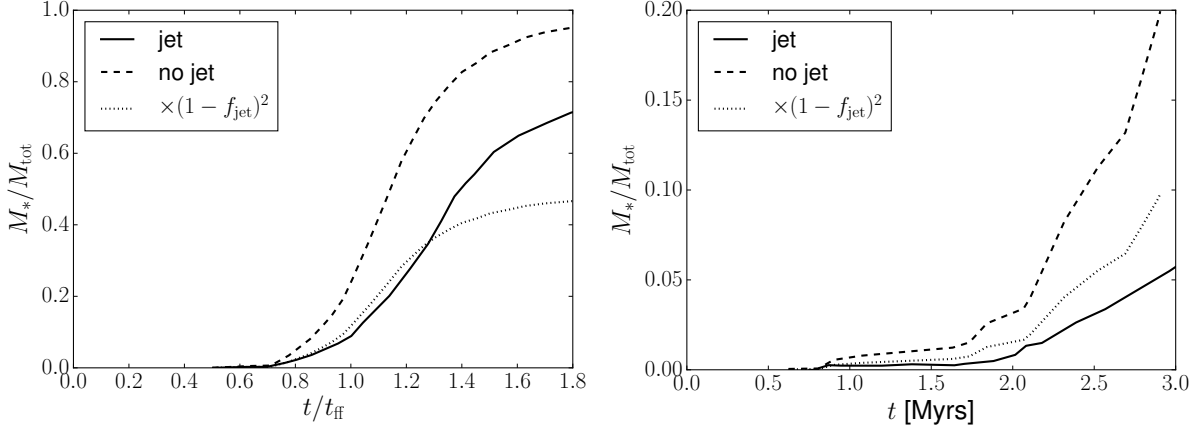


Figure 36 : Left plot: the SFE, M_*/M_{tot} , as a function of time (measure in free-fall times) for the jet (solid line) and no-jet (dashed line) cases from Federrath et al. (2014) Figure 9 (N.B. HD simulation). Right plot: the SFE as a function of time (measure in Myrs) for the jet (solid line) and no-jet (dashed line) cases from Federrath (2015) Figure 2 (N.B. MHD simulation). In both plots we have rescaled the no-jet case by $f = (1 - f_{\text{jet}})^2$, which is set to $f_{\text{jet}} = 0.3$. In the left plot the rescaled no-jet case follows the jet case fairly well up to about an SFE of about 0.4. The rescaled no-jet case at this point re-scales the no-jet case for $M_*/M_{\text{tot}} \approx 0.8$, where the accretion onto star particles is starved due to depletion of gas. In the right plot, the rescaled no-jet case does a rather poor job of following the jet case. This may be because Federrath (2015) does a MHD calculation rather than a HD calculation as in Federrath et al. (2014).

when jet feedback is included. This result is also seen in Wang et al. (2010); Federrath et al. (2014); Federrath (2015). While these authors did not note the power law dependence of mass upon time, it is clearly seen in their Figures 1, 9, and 2, respectively. From these figures we have calculated the ratio of stellar mass in the no jet to jet case, finding the ratios to be 2.3, 2.4, and 3, respectively, which is similar to our ratio of 2.5.

The scaling between the jets and no-jet case of $f^2 = (1 - f_{\text{jet}})^2$ that we have found above in equation (3.3.3) appears to hold for Federrath et al. (2014). This is shown in the left plot of Figure 36. Here we plot the SFE as a function of time from Figure 9 of Federrath et al. (2014) for the jet (solid line) and no-jet (dashed line) cases. We have also applied the simple rescaling $f^2 = (1 - f_{\text{jet}})^2$ following equation (3.3.3) where $f_{\text{jet}} = 0.3$ in Federrath et al. (2014), the result is shown as the dotted line in Figure 36. The rescaled no-jet case does a surprisingly good job of following the jet case up to about an SFE of 0.4, which corresponds to a no-jet SFE of 0.8, after which the SFE of the no-jet case

(unsurprisingly) turns over as there is little gas remaining to be accreted. In the right plot of Figure 36, we plot SFE as a function of time from Figure 2 of Federrath (2015) for the jet (solid line), no-jet (dashed line), and rescaled (dotted line) cases. Here the rescaled no-jet case does a rather poor job of following the jet case. This may be because Federrath et al. (2014) (right plot) does a MHD calculation rather than a HD calculation as in Federrath et al. (2014) (left plot). We do not believe that our analytic model can explain the evolution of \dot{M} beyond $t/t_{ff} > 1.3$, nor do we think it should. After a single free fall time $\approx 10\%$ of the entire gas mass in the simulation has been eaten by the created sink particles. By $t \approx 1.3t_{ff}$ that has expanded to nearly 40% of all the gas in the simulation. Once the mass of the stars becomes an appreciable fraction of the gas mass, accretion begins to be suppressed simply because there is insufficient gas. This should occur when the mass in stars is a few tens of percent of the gas mass.

The scaling of equation (3.3.3) may hold for other cases in the literature but we are unable to check them. For example, it is unclear in Wang et al. (2010) what f_{jet} is equal to. Myers et al. (2014) see the same curvature in $\dot{M}_*(t)$ that we do (their Figure 7), but they do not plot a no protostellar feedback simulation to compare against.

It appears that for hydrodynamic jet-feedback, the effect is to reduce the mass accretion rate by the rate at which the jet ejects material from the star (and disk). Beyond this, the effects of hydrodynamic jet feedback appear to be minor. This is clearly seen in the simulations of this paper and that of Federrath et al. (2014). It may also be the case for other simulations in the literature, but such comparisons were not possible in those cases.

It does appear that magnetic field may enhance the effects of jet feedback. The systematic evidence for this is sparse, but we can point to the comparison between the rescaled no-jet case and jet case of Federrath (2015) in the right plot of Figure 36, where the rescaled case does not capture the complete effect of the jet. Here the dynamics of the jet on the accreting gas appears to be more pronounced. We should note, however, that the curvature in the SFE remains and suggests that some of the analytic results of MC15 may continue to hold in the MHD case.

3.5 Conclusions

We performed simulations of turbulent, self-gravitating gas including star particle formation and protostellar jets. Starting with uniform density in a box with length 16 parsecs on a side, we drove turbulence until we reached a statistically steady state. At that point, the density was no longer uniform. We then turned on gravity and star formation. We used AMR to follow collapsing regions down to an effective resolution of $32k^3$ which gave us a Δx of $\sim 50\text{AU}$ at the finest level of refinement.

We observed that the inclusion of protostellar jets does not affect the general dynamics of accreting gas. In particular we saw $M_*(t) \propto f^2(t-t_*)^2$ where $f = 1 - f_{\text{jet}}$ is the fraction of mass accreted onto the protostar and f_{jet} is the fraction ejected by the jet. We find that this mass ejection accounts for 75% of the effect of jets on the star formation rate in our simulations. This appears to be the case in similar simulations performed by other groups (e.g. see Figure 36), but we find suggestions that this may be altered if MHD is included.

As we have found previously in the case without jets, Chapter 2 (Murray et al. 2017), the spherical average profile of gas around the protostar follows the analytic model of MC15 and does not seem to change in the case with jets. In particular, the run of density finds an attractor solution prior to star formation and remains on that solution even after jets begin to blow out cavities in the surrounding medium. The behavior of the infall and rotational velocities is similar regardless of whether jets are included or not. The profile of the random velocities are also similar once the jet bi-cone is removed. Finally, the mass accretion rates are similar in the jet and no-jet cases.

We also find that the collapse is outside-in (Murray et al. 2017), and holds for both the jet and no jet simulations. The average jet momentum per stellar mass does increase over time, though this is to be expected as the stars continue to accrete mass. We did not run long enough for the stars to completely consume the surrounding gas and thus for the jets to begin to be shut off. We find that jets do drive turbulence in the surrounding gas, but is confined to small scales of roughly a parsec.

3.6 Appendix

3.6.1 Effects of Excising Bi-cones Aligned with Protostellar Jets on the Infall, Random, and Rotational Velocity

In this appendix we illustrate the effect of excising bi-cones aligned with the jet emitted by a protostar when calculating $|\vec{u}_r|$, \vec{v}_T and \vec{v}_ϕ . The simulated jets are powerful enough that they enforce outflow over almost the entire bi-cone over which the star particle emits the jet. However, because our jets are emitted along the instantaneous spin axis of the star particle, which is usually roughly perpendicular to the accretion disk, the jet outflow tends to avoid high density and infalling gas, which is generally near the plane of the disk. An example can be seen in Figure 26.

While the jets do not strongly affect the infall and rotational velocity of the bulk of the gas near the star particle, they do have a fairly strong effect on the random velocity, when averaged over spherical shells. A glance at Figure 26 shows why: the jet velocities are very large in the evacuated region around the jet axis. Our calculation of \vec{v}_T involves subtracting the mass-weighted infall and rotational velocity in spherical shells from the velocity of each cell in the shell; since the jet expels low density gas, it does not affect the mass weighted infall or rotational velocity when performing the average, but it does boost the random velocity.

In Figure 37 we show three panels. All three panels follow the same convention: the infall velocity $|\vec{u}_r|$ is depicted by the blue triangles, connected by a solid blue line, the green circles connected by a solid green line show \vec{v}_T while the black crosses show the rotational velocity \vec{v}_ϕ . The dashed red line shows $\vec{v}_K \equiv \sqrt{GM(\vec{r})/r}$. Finally, the sound speed is denoted by the black horizontal line.

All three snapshots are of the same particle, of roughly $5.2 M_\odot$, at the same time, from the same simulation. In the top panel we calculate the various velocities averaged over spherical shells, i.e., we do not remove the jet bi-cone, in the center panel we remove the jet bi-cone, and in the bottom panel we remove a bi-cone with twice the jet opening angle.

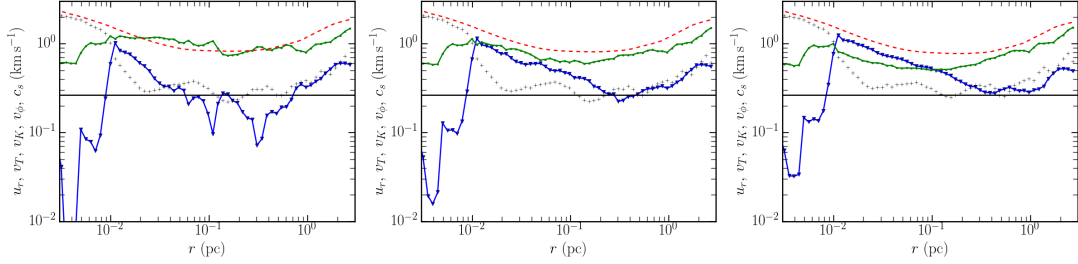


Figure 37 : The run of velocity for a $M_* \approx 5.2 M_\odot$ sink particle, averaged over spherical shells (left), averaged over the same shells but excising a bi-cone aligned with and having the same opening angle as the jet (middle) and excising a bi-cone with twice the jet opening angle (right). The sound speed is denoted by the black horizontal line while other lines denote the infall velocity $|\vec{u}_r|$ (blue triangles connected by a solid blue line), the random velocity \vec{v}_T (green circles connected by a solid green line) and the rotational velocity \vec{v}_ϕ (black crosses); the dashed red line shows $\vec{v}_K \equiv \sqrt{GM(\vec{r})/\vec{r}}$. Note that both $|\vec{u}_r|$ and \vec{v}_T increase with decreasing radius for $10^{-2} \text{ pc} < \vec{r} < 10^{-1} \text{ pc}$.

The most dramatic change is in the turbulent velocity. When we average over full spherical shells (top panel), the turbulent velocity remains roughly constant at all radii, with a slight increase at $\vec{r} > 1 \text{ pc}$. In the two plots where we excise the jet bi-cone (or a bi-cone with twice the jet opening angle), we see similar behavior to runs where no jets were included; at large radii the random velocity \vec{v}_T decreases (by a factor of two) with decreasing radius, while at small radii ($\vec{r} \lesssim 0.1 \text{ pc}$) \vec{v}_T increases with decreasing radius.

The effect of removing or not removing the jet bi-cone on $|\vec{u}_r|$ and \vec{v}_ϕ is much smaller. The infall velocity smooths out slightly when we excise the region around the jet, but the general dynamic of decreasing velocity with decreasing radius at large \vec{r} , and then inverting to increasing velocity with decreasing radius for $\vec{r} \lesssim 0.1 \text{ pc}$ is seen in all three panels.

3.6.2 Protostellar Model

There is one final thing to note about the protostellar model presented by O09, which is the transition from no burning to core burning at a fixed temperature of 1.5×10^6 Kelvin. When this transition is made, the polytropic index n is changed from whatever its' current value is to 1.5. However, in changing n we change the internal temperature of the protostar to a lower value than the required fixed temperature. This raises the

question of whether or not this has any effect on the radius of the star, the protostar's final mass, radius, and the length of time, for its evolution. We did run a quick experiment with looping n back and forth to achieve an actual burn temperature of 1.5×10^6 (rather than O09's dropping to a constant lower temperature). What we found was that the end result sees no appreciable difference: roughly the same mass, same radius, and in roughly the same amount of time. The only modification was a change of $\approx 1/16$ th the radius during the core burning phase of the evolution of the protostar.

Chapter 4

Conclusions

“There is no real ending. It’s just the place where you stop the story.”

— The King, *Dune* by Frank Herbert

I find that the star formation rate at small scales varies with time. This has several implications: It means observers can not judge the age of a system from its run of density, as the density has been shown reach an attractor solution. It indicates that there must exist a form of rapid feedback, in order to disrupt star formation, as the 4 million year wait for supernovae is too long. This requirement of rapid feedback is consistent with galaxy scale simulations, such as Hopkins et al. (2014). Their simulations include explicit treatment of the multiphase ISM and stellar feedback, and Hopkins et al. (2014) found that those sources of feedback reproduce the observed halo and stellar mass relationship. Agertz & Kravtsov (2015) find that radiation pressure and efficient supernovae feedback together, is crucial, as removing any of these feedback sources affects the star formation history.

The research which makes up the body of work in this dissertation was motivated, in large part, by the discrepancies between observations and the analytic models. Numerical simulations, as well, failed to account for the most recent insights into how stars form.

4.1 Isolating the Effect of Random Thermal Motions

My initial simulations did not include the additional physics of magnetic fields, winds, jets or supernovae. This was an effort to understand how the system behaves in its simplest form.

The significance of my results is twofold—turbulence is, in fact, a dynamic variable, driven by adiabatic compression (Robertson & Goldreich 2012), and the turbulence itself acts to slow the collapse. Furthermore, these outcomes are supported by observations made of massive star forming regions. As highlighted in this dissertation, $\vec{v}_T \propto r^p$ with $p \sim 0.2 - 0.3$, and that at small radii or high density, \vec{v}_T increases with increasing density, (Plume et al. 1997). We find these departures from Larson’s law only in collapsing regions in our simulations.

Two length scales emerge from the process of star formation, \vec{r}_* and \vec{r}_d . We demonstrate that these length scales are clearly associated with physical effects. As mentioned in section 1.6 analytic theories assumed that the solution shows a self-similarity, and thus would present a power law solution. In fact, there are two power laws, which change at $\vec{r}_*(t)$. One power law inside of \vec{r}_* (but outside \vec{r}_d) $|\vec{u}_T|$ and \vec{v}_T are both $\propto \mathbf{r}^{-1/2}$; and outside of \vec{r}_* , $\vec{v}_T \sim \mathbf{r}^p$ (with $p \approx 0.2$), while $|\vec{u}_T|$ is on average about constant. It is worth emphasizing, that $\vec{r}_*(t)$, the length scale at which the character of the solution changes, is time dependent. As the star grows in mass, the radius where the stars’ gravity exceeds the gravity of the surrounding gas increases outwards away from the star, $\vec{r}_*(t) \propto M_*^{2/3}(t)$. The disk radius, \vec{r}_d , also changes as a function of time as a result of the advection and transport of angular momentum from large scales to small scales (and vice versa).

I found that the density profile evolves to a time-independent attractor solution, $\rho(\vec{r}, t) \rightarrow \rho(\vec{r})$. The implication is that one cannot infer the age or lifetime of these structures via the free-fall or crossing time.

I also show that the acceleration due to the pressure gradient is comparable to that due to gravity at all $\vec{r} > \vec{r}_d$. As a result, the infall velocity is substantially smaller than

the free fall velocity even very close to the star or accretion disk. Inside \vec{r}_d , rotational support takes over and as a result $|\vec{u}_r|$ and \vec{v}_T both decrease.

I found the development of rotationally supported disks at $\vec{r}_d \sim 0.01$ pc. These disks have radii comparable to or slightly larger than disks seen around young stars in Taurus ($\sim 500 - 900$ AU) (Padgett et al. 1999) in which stellar feedback effects are minimal, and where the undisturbed disks are larger than in more active star forming regions such as Orion, where the disk radii are ~ 100 AU (Williams & Cieza 2011). As mentioned previously, large scale magnetic fields may transfer angular momentum away from these disks, shrinking them.

My simulated disks appear to be marginally gravitationally stable, similar to Kratter et al. (2010). If my disks are gravitationally unstable, at least part of the time, it would suggest that large scale gravitational torques could be responsible for transport of material and angular momentum in our simulations. However, while I resolve the radial component of the accretion disk, I do not resolve the scale height of my disks. This lack of resolution calls into question the ability of my simulations to properly describe the angular momentum transport of (potentially) self-gravitating disks. As mentioned previously, the simulation box length is 16 pc with an effective resolution of 32768^3 . That resolution and length scale correspond to a cell length of $\sim 5 \times 10^{-4}$ pc = 50 AU. Radially the simulated disks extend up to 0.01 pc, allowing roughly twenty cells to resolve the radial portion of the disk. However, this does not indicate sufficient resolution of the scale height of the disk; which have been seen to have thicknesses of ~ 50 to 350 AU in Taurus (Padgett et al. 1999), corresponding to 1 \sim few cells. This is not enough to consider the scale height of the disk resolved.

I have shown that the assumptions made by previous analytic collapse models (Shu 1977; Myers & Fuller 1992; McLaughlin & Pudritz 1997; McKee & Tan 2003), are not fulfilled in my simulations. In my simulations, the collapsing regions do not start from a hydrostatic equilibrium, nor do they show any evidence of inside-out collapse. The gathering of material before collapse, i.e., before the central cusp in the density power law is formed, involves transonic bulk motions and supersonic random motions (see Figure

11). The accretion of mass starts at large scales ($\vec{r} \sim 1 \text{ pc}$) with large initial infall velocities. In addition, we find that \vec{v}_T scales differently in collapsing regions as opposed to the rest of the simulation box, whereas the turbulent collapse models (McLaughlin & Pudritz 1997; McKee & Tan 2003) assume that the scaling of \vec{v}_T with \vec{r} remains fixed.

4.2 The Effect of Protostellar Jets

We observed that protostellar jets do not affect the general dynamics of accreting gas. In particular, $M_*(t) \propto f^2(t - t_*)^2$ where $f = 1 - f_{\text{jet}}$ is the fraction of mass accreted onto the protostar and f_{jet} is the fraction ejected by the jet. We find that this mass ejection accounts for 75% of the effect of jets on the star formation rate in our simulations.

The spherical average profile of gas around the protostar follows the analytic model of MC15 and does not appear to change in the case with jets. The run of density finds an attractor solution prior to star formation and remains on that solution even after jets begin to blow out cavities in the surrounding medium. The behavior of the infall and rotational velocities is similar regardless of whether jets are included or not. The profile of the random velocities is also similar, once the jet bi-cone is removed. Finally, the mass accretion rates are similar in the jet and no-jet cases.

It is worth noting again that the collapse is *outside-in*. This result holds for simulations that both include and ignore protostellar jet feedback. The average jet momentum per stellar mass does increase over time, though this is to be expected as the stars continue to accrete mass. Our runs were not long enough for the stars to completely consume the surrounding gas and thus, for the jets to begin to be shut off. We find that jets do drive turbulence in the surrounding gas, but is confined to small scales of roughly a parsec.

4.3 Future Work

As the King in Dune rather eloquently stated, our story doesn't truly end here. The results presented in this dissertation advance the story of star formation, but there is still much we do not understand and further work is required.

For instance, this theory and the results of this dissertation, has not yet looked at the effects of magnetic fields. There are several papers (Li et al. 2009; Burkhardt et al. 2015; Mocz et al. 2017) , which suggest that magnetic fields have an effect on the rate of star formation. Whether that contribution modifies the $M_*(t) \propto t^2$ profile we've seen or the normalization, like protostellar jets, has yet to be determined.

As mentioned above, my simulations also neglect strong physical effects at late times. For example, the absence of radiation is not physically accurate for sink particles that grow beyond $\sim 4 M_\odot$. We direct the reader to section 1.8.1 for our argument about $M < 4 M_\odot$. The upshot was that we expect that the effects of radiation pressure are not particularly significant in the situations we report; the run of density and infall velocity, and hence the $M_*(t) \sim t^2$ scaling should not be affected, at least up to the times we are reporting on. This estimate neglects the effect of radiative or ionization heating which is an important feedback mechanism. In addition, our argument in 1.8.1 indicates that radiation dynamics must have a significant effect when $M_* \geq 4 M_\odot$.

Radiative feedback will also affect both the IMF and, for massive enough stars, the dynamics of the collapse at late times (after massive stars have formed).

Simulations including radiative feedback support this simple analysis. Figure 15 of Myers et al. (2014) shows that in their simulations, which include feedback from both protostellar outflows and radiation (as well as magnetic fields), the stellar mass increases as the square of the time, up to masses of $\sim 4.5 M_\odot$. Earlier work by the Berkeley group found similar results, forming stars with 10 solar masses, with $M_*(t) \sim t^2$ even for such massive stars, see Figure 13 of Krumholz et al. (2012b). Their simulations included radiative effects, but no protostellar winds.

Among the myriad of contributions that can be made, in particular, looking at the chemistry of these regions, holds many avenues of intrigue. Creating predictions about the species, the type and amount of emission and absorption of radiation that may be seen would provide specific tracers/profiles that may be observed. This knowledge, and the generation of synthetic observations from these simulations would allow more accurate searches and testing by the latest generation of telescopes.

The knowledge and wisdom of those who came before has allowed us to partially unravel the mysterious tapestry that is our Universe. Our inquisitiveness and thirst for truth will drive us to question and pull harder on that thread. To answer the question of what halts star formation, a saying I learned as a child comes to mind: “The motto of all the mongoose family is, ‘Run and find out,’ and Rikki-tikki was a true mongoose.” (Pinkney & Kipling 1997).

Bibliography

- Agertz, O., & Kravtsov, A. V. 2015, *ApJ*, 804, 18
- Agertz, O., Kravtsov, A. V., Leitner, S. N., & Gnedin, N. Y. 2013, *ApJ*, 770, 25
- Andersen, M., Gennaro, M., Brandner, W., et al. 2017, *A&A*, 602, A22
- Aumer, M., White, S. D. M., Naab, T., & Scannapieco, C. 2013, *MNRAS*, 434, 3142
- Balbus, S. A., & Hawley, J. F. 1991, *ApJ*, 376, 214
- . 1998, *Reviews of Modern Physics*, 70, 1
- Bate, M. R. 2012, *MNRAS*, 419, 3115
- Bethe, H. A. 1939, *Physical Review*, 55, 434
- Bigiel, F., Leroy, A., Walter, F., et al. 2008, *AJ*, 136, 2846
- Bleuler, A., & Teyssier, R. 2014, *MNRAS*, 445, 4015
- Blitz, L., Fukui, Y., Kawamura, A., et al. 2007, *Protostars and Planets V*, 81
- Burkhart, B., Collins, D. C., & Lazarian, A. 2015, *ApJ*, 808, 48
- Caselli, P., & Myers, P. C. 1995, *ApJ*, 446, 665
- Cho, W., & Kim, J. 2011, *MNRAS*, 410, L8
- Chomiuk, L., & Povich, M. S. 2011, *AJ*, 142, 197
- Collins, D. C., Padoan, P., Norman, M. L., & Xu, H. 2011, *ApJ*, 731, 59

- Csengeri, T., Bontemps, S., Schneider, N., Motte, F., & Dib, S. 2011, *A&A*, 527, A135
- Cunningham, A. J., Klein, R. I., Krumholz, M. R., & McKee, C. F. 2011, *ApJ*, 740, 107
- Dame, T. M. 1993, in *American Institute of Physics Conference Series*, Vol. 278, *Back to the Galaxy*, ed. S. S. Holt & F. Verter, 267–278
- Dekel, A., & Silk, J. 1986, *ApJ*, 303, 39
- Dubey, A., Fisher, R., Graziani, C., et al. 2008, in *Astronomical Society of the Pacific Conference Series*, Vol. 385, *Numerical Modeling of Space Plasma Flows*, ed. N. V. Pogorelov, E. Audit, & G. P. Zank, 145
- Dubois, Y., Devriendt, J., Slyz, A., & Teyssier, R. 2010, *MNRAS*, 409, 985
- Ewen, H. I., & Purcell, E. M. 1951, *Nature*, 168, 356
- Ezer, D., & Cameron, A. G. W. 1967, *Canadian Journal of Physics*, 45, 3429
- Federrath, C. 2015, *MNRAS*, 450, 4035
- Federrath, C., Banerjee, R., Clark, P. C., & Klessen, R. S. 2010a, *ApJ*, 713, 269
- Federrath, C., & Klessen, R. S. 2012, *ApJ*, 761, 156
- Federrath, C., Klessen, R. S., & Schmidt, W. 2008, *ApJ*, 688, L79
- Federrath, C., Roman-Duval, J., Klessen, R. S., Schmidt, W., & Mac Low, M.-M. 2010b, *A&A*, 512, A81
- Federrath, C., Schrön, M., Banerjee, R., & Klessen, R. S. 2014, *ApJ*, 790, 128
- Federrath, C., Sur, S., Schleicher, D. R. G., Banerjee, R., & Klessen, R. S. 2011, *ApJ*, 731, 62
- Fryxell, B., Olson, K., Ricker, P., et al. 2000, *ApJS*, 131, 273
- Gavagnin, E., Bleuler, A., Rosdahl, J., & Teyssier, R. 2017, *MNRAS*, 472, 4155

Gong, M., & Ostriker, E. C. 2015, *ApJ*, 806, 31

Governato, F., Brook, C., Mayer, L., et al. 2010, *Nature*, 463, 203

Guo, Q., White, S., Li, C., & Boylan-Kolchin, M. 2010, *MNRAS*, 404, 1111

Hansen, C. E., Klein, R. I., McKee, C. F., & Fisher, R. T. 2012, *ApJ*, 747, 22

Heiderman, A., Evans, II, N. J., Allen, L. E., Huard, T., & Heyer, M. 2010, *ApJ*, 723, 1019

Heiles, C., & Troland, T. H. 2003, *ApJ*, 586, 1067

Ho, P. T. P., & Haschick, A. D. 1986, *ApJ*, 304, 501

Hopkins, P. F., Kereš, D., Oñorbe, J., et al. 2014, *MNRAS*, 445, 581

Hopkins, P. F., Quataert, E., & Murray, N. 2011, *MNRAS*, 417, 950

—. 2012, *MNRAS*, 421, 3522

Kalberla, P. M. W., & Kerp, J. 2009, *ARA&A*, 47, 27

Kennicutt, Jr., R. C. 1998, *ApJ*, 498, 541

Klaassen, P. D., & Wilson, C. D. 2008, *ApJ*, 684, 1273

Klaassen, P. D., Wilson, C. D., Keto, E. R., et al. 2011, *A&A*, 530, A53

Klessen, R. S. 2000, *ApJ*, 535, 869

Klessen, R. S., Heitsch, F., & Mac Low, M.-M. 2000, *ApJ*, 535, 887

Kratter, K. M., Matzner, C. D., Krumholz, M. R., & Klein, R. I. 2010, *ApJ*, 708, 1585

Kritsuk, A. G., Norman, M. L., & Wagner, R. 2011, *ApJ*, 727, L20

Krumholz, M. R., Dekel, A., & McKee, C. F. 2012a, *ApJ*, 745, 69

Krumholz, M. R., Klein, R. I., & McKee, C. F. 2012b, *ApJ*, 754, 71

- Krumholz, M. R., Klein, R. I., McKee, C. F., Offner, S. S. R., & Cunningham, A. J. 2009, *Science*, 323, 754
- Krumholz, M. R., Myers, A. T., Klein, R. I., & McKee, C. F. 2016, *MNRAS*, 460, 3272
- Krumholz, M. R., & Tan, J. C. 2007, *ApJ*, 654, 304
- Lada, C. J., & Lada, E. A. 2003, *ARA&A*, 41, 57
- Lada, C. J., Lombardi, M., & Alves, J. F. 2010, *ApJ*, 724, 687
- Lamberts, A., & Daigne, F. 2018, *MNRAS*, 474, 2813
- Lamberts, A., Fromang, S., & Dubus, G. 2011, *MNRAS*, 418, 2618
- Lamberts, A., Fromang, S., Dubus, G., & Teyssier, R. 2013, *A&A*, 560, A79
- Lamberts, A., Millour, F., Liermann, A., et al. 2017, *MNRAS*, 468, 2655
- Larson, R. B. 1969, *MNRAS*, 145, 271
- . 1981, *MNRAS*, 194, 809
- . 2005, *MNRAS*, 359, 211
- Lee, D., Deane, A. E., & Federrath, C. 2009, in *Astronomical Society of the Pacific Conference Series*, Vol. 406, *Numerical Modeling of Space Plasma Flows: ASTRONUM-2008*, ed. N. V. Pogorelov, E. Audit, P. Colella, & G. P. Zank, 243
- Lee, E. J., Chang, P., & Murray, N. 2015, *ApJ*, 800, 49
- Lee, E. J., Miville-Deschênes, M.-A., & Murray, N. W. 2016, *ApJ*, 833, 229
- Li, H.-b., Dowell, C. D., Goodman, A., Hildebrand, R., & Novak, G. 2009, *ApJ*, 704, 891
- Li, P. S., Klein, R. I., & McKee, C. F. 2018, *MNRAS*, 473, 4220
- Matzner, C. D. 2007, *ApJ*, 659, 1394
- Matzner, C. D., & McKee, C. F. 2000, *ApJ*, 545, 364

- McGaugh, S. S., Schombert, J. M., de Blok, W. J. G., & Zagursky, M. J. 2010, *ApJ*, 708, L14
- McKee, C. F., & Tan, J. C. 2002, *Nature*, 416, 59
- . 2003, *ApJ*, 585, 850
- McKee, C. F., & Zweibel, E. G. 1992, *ApJ*, 399, 551
- McLaughlin, D. E., & Pudritz, R. E. 1997, *ApJ*, 476, 750
- Mihalas, D., & Mihalas, B. W. 1984, *Foundations of radiation hydrodynamics*
- Miville-Deschênes, M.-A., Murray, N., & Lee, E. J. 2017, *ApJ*, 834, 57
- Mocz, P., Burkhart, B., Hernquist, L., McKee, C. F., & Springel, V. 2017, *ApJ*, 838, 40
- Mooney, T. J., & Solomon, P. M. 1988, *ApJ*, 334, L51
- Mouschovias, T. C. 1976, *ApJ*, 207, 141
- Muller, C. A., & Oort, J. H. 1951, *Nature*, 168, 357
- Murray, D. W., Chang, P., Murray, N. W., & Pittman, J. 2017, *MNRAS*, 465, 1316
- Murray, N. 2011, *ApJ*, 729, 133
- Murray, N., & Chang, P. 2015, *ApJ*, 804, 44
- Myers, A. T., Klein, R. I., Krumholz, M. R., & McKee, C. F. 2014, *MNRAS*, 439, 3420
- Myers, P. C., & Fuller, G. A. 1992, *ApJ*, 396, 631
- Nakamura, F., & Li, Z.-Y. 2007, *ApJ*, 662, 395
- . 2011, *ApJ*, 740, 36
- Nakano, T., Hasegawa, T., Morino, J.-I., & Yamashita, T. 2000, *ApJ*, 534, 976
- Ocvirk, P., Gillet, N., Shapiro, P. R., et al. 2016, *MNRAS*, 463, 1462

- Offner, S. S. R., Klein, R. I., McKee, C. F., & Krumholz, M. R. 2009, *ApJ*, 703, 131
- Padgett, D. L., Brandner, W., Stapelfeldt, K. R., et al. 1999, *AJ*, 117, 1490
- Padoan, P., Haugbølle, T., & Nordlund, Å. 2014, *ApJ*, 797, 32
- Padoan, P., Juvela, M., Bally, J., & Nordlund, Å. 1998, *ApJ*, 504, 300
- Padoan, P., & Nordlund, Å. 2002, *ApJ*, 576, 870
- . 2011, *ApJ*, 730, 40
- Pawsey, J. L. 1951, *Nature*, 168, 358
- Penston, M. V. 1969, *MNRAS*, 144, 425
- Peretto, N., Fuller, G. A., Duarte-Cabral, A., et al. 2013, *A&A*, 555, A112
- Pinkney, J., & Kipling, R. 1997, *Rikki-tikki-tavi* (Morrow Junior Books)
- Piontek, F., & Steinmetz, M. 2011, *MNRAS*, 410, 2625
- Plume, R., Jaffe, D. T., Evans, II, N. J., Martín-Pintado, J., & Gómez-González, J. 1997, *ApJ*, 476, 730
- Ragan, S. E., Heitsch, F., Bergin, E. A., & Wilner, D. 2012, *ApJ*, 746, 174
- Ragan, S. E., Henning, T., Beuther, H., Linz, H., & Zahorecz, S. 2015, *A&A*, 573, A119
- Ricker, P. M. 2008, *ApJS*, 176, 293
- Robertson, B., & Goldreich, P. 2012, *ApJ*, 750, L31
- . 2018, *ApJ*, 854, 88
- Rosdahl, J., Blaizot, J., Aubert, D., Stranex, T., & Teyssier, R. 2013, *MNRAS*, 436, 2188
- Rosdahl, J., & Teyssier, R. 2015, *MNRAS*, 449, 4380
- Rosolowsky, E. W., Pineda, J. E., Kauffmann, J., & Goodman, A. A. 2008, *ApJ*, 679, 1338

- Schaller, G., Schaerer, D., Meynet, G., & Maeder, A. 1992, *A&AS*, 96, 269
- Scoville, N. Z., & Good, J. C. 1989, *ApJ*, 339, 149
- Shetty, R., Kelly, B. C., & Bigiel, F. 2013, *MNRAS*, 430, 288
- Shu, F. H. 1977, *ApJ*, 214, 488
- Skinner, M. A., & Ostriker, E. C. 2015, *ApJ*, 809, 187
- Solomon, P. M., Rivolo, A. R., Barrett, J., & Yahil, A. 1987, *ApJ*, 319, 730
- Strittmatter, P. A. 1966, *MNRAS*, 132, 359
- Sur, S., Schleicher, D. R. G., Banerjee, R., Federrath, C., & Klessen, R. S. 2010, *ApJ*, 721, L134
- Tackenberg, J., Beuther, H., Henning, T., et al. 2012, *A&A*, 540, A113
- Teyssier, R. 2002, *A&A*, 385, 337
- Traficante, A., Fuller, G. A., Peretto, N., Pineda, J. E., & Molinari, S. 2015, *MNRAS*, 451, 3089
- Trimble, V. 1997, in *American Institute of Physics Conference Series*, Vol. 393, American Institute of Physics Conference Series, ed. S. S. Holt & L. G. Mundy, 15–37
- Truelove, J. K., Klein, R. I., McKee, C. F., et al. 1997, *ApJ*, 489, L179
- Trumpler, R. J. 1930, *Lick Observatory Bulletin*, 14, 154
- Wang, P., Li, Z.-Y., Abel, T., & Nakamura, F. 2010, *ApJ*, 709, 27
- Williams, J. P., Blitz, L., & McKee, C. F. 2000, *Protostars and Planets IV*, 97
- Williams, J. P., & Cieza, L. A. 2011, *ARA&A*, 49, 67
- Wilson, R. W., Jefferts, K. B., & Penzias, A. A. 1970, *ApJ*, 161, L43
- Wu, J., Evans, II, N. J., Shirley, Y. L., & Knez, C. 2010, *ApJS*, 188, 313

Wyrowski, F., Güsten, R., Menten, K. M., et al. 2016, *A&A*, 585, A149

Zhu, W., Petrovich, C., Wu, Y., Dong, S., & Xie, J. 2018, ArXiv e-prints,
arXiv:1802.09526

4.4 Curriculum Vitae

CURRICULUM VITAE

Daniel Murray

Place of birth: Santa Monica, CA

EDUCATION

- 8/2012–5/2018* **Doctor of Philosophy in Physics**
University of Wisconsin – Milwaukee, Milwaukee WI
Advisor: Dr. Philip Chang
GPA: 3.07/4.00
- 9/2008–6/2012* **Bachelor of Science in Physics**
University of California Santa Barbara, Santa Barbara, CA
GPA: 3.00/4.00

RESEARCH EXPERIENCE

- 8/2012–present* **Graduate Research Assistant**
University of Wisconsin - Milwaukee, Milwaukee WI
Advisor: Dr. Philip Chang
- 6/2011 – 8/2011* **Summer Undergraduate Research Assistant**
Smithsonian Astrophysical Observatory, Cambridge MA
Advisor: Dr. Matthew Holman
- 6/2010 – 1/2011* **Undergraduate Research Assistant**
Las Cumbres Observatory, Santa Barbara CA
Advisor: Dr. Andy Howell
- 12/2009 – 3/2010* **Undergraduate Research Assistant**
University of California, Santa Barbara, Santa Barbara CA
Advisor: Dr. Phil Lubin

TEACHING EXPERIENCE

8/2012–5/2018 **Teaching Assistant and Lecturer**
University of Wisconsin – Milwaukee, Milwaukee, WI
Discussion section leader for introductory and advanced physics courses
Led discussion sections for both introductory and
advanced undergraduate courses

FELLOWSHIPS & AWARDS

2018 Department of Physics Papastamatiou Scholarship (UWM)

CONFERENCES AND PRESENTATIONS

Iowa High Performance Computing Summer School Iowa City, IA July 2013.
Fundamentals of HPC, including OpenMPI and CUDA.

Princetons Institute for Advanced Study Prospects in Theoretical Physics 2016, Princeton, NJ July 2016. Oral presentation on the effects of turbulence on gravitational collapse.

Graduate Student Research Symposium for Math, Engineering, and the Natural Sciences, Milwaukee, WI, October. 2016. Poster presentation on the effects of turbulence on gravitational collapse.

Midwest Magnetic Fields 2017 Workshop, Madison, WI, May. 2017. Oral presentation on the effects of magnetic fields on the star formation rate for massive star forming regions.

PUBLICATIONS

Primary Publications

D. Murray, and P. Chang. “The Effects of Magnetic Fields on Turbulent Collapse”. (in prep.)

D. Murray, S. Goyal, and P. Chang. “The Effects of Protostellar Jet Feedback on Turbulent Collapse.” MNRAS 2018 arXiv: 1710.09415

M. Holman, M. Payne, W. Fraser, P. Lacerda, M. Bannister, M. Lackner, Y. Chen, H. Lin, K. Smith, R. Kokotanekova, K. Chambers, S. Chastel, L. Denneau, A. Fitzsimmons, H. Flewelling, T. Grav, M. Huber, N. Induni, A. Krolewski, R. Jedicke, E. Lilly, E. Magnier, Z. Mark, M. Micheli, **D. Murray**, et al. “A Dwarf Planet Class Object in the 21:5 Resonance with Neptune.” ApJ Letters 2017

D. Murray, P. Chang, N. Murray, and J. Pittman. “Collapse in Self-gravitating Turbulent Fluids.” MNRAS 2017; 465:1316

E. O. Ofek, M. Sullivan, S. B. Cenko, M. M. Kasliwal, A. Gal-Yam, S. R. Kulkarni, I. Arcavi, L. Bildsten, J. S. Bloom, A. Horesh, D. A. Howell, A. V. Filippenko, R. Laher, **D. Murray**, et al. “An outburst from a massive star 40 days before a supernova explosion.” Nature 2013; 494:65

A. Corsi, E. O. Ofek, D. A. Frail, D. Poznanski, I. Arcavi, A. Gal-Yam, S. R. Kulkarni, K. Hurley, P. A. Mazzali, D. A. Howell, M. M. Kasliwal, Y. Green, **D. Murray**, D. Xu, S. Ben-ami, J. S. Bloom, B. Cenko, N. M. Law, P. Nugent, R. M. Quimby, V. Pal'shin, J. Cummings, V. Connaughton, K. Yamaoka, A. Rau, W. Boynton, I. Mitrofanov, J. Goldsten "PTF 10bzf (SN 2010ah): a broad-line Ic supernova discovered by the Palomar Transient Factory." ApJ 2011; 741:76

Telegrams

Supernova 2010mc 2012CBET.3313....2H

Supernova 2010ko in NGC 1954. 2010CBET.2575....2P